



UNIVERSITÀ
DI PISA

Dipartimento di Ingegneria
Corso di Laurea Magistrale in Ingegneria Biomedica

TESI DI LAUREA:

**Development of non-invasive methods for
quantification of peripheral sympathetic nerve
activity**

Relatore:

Prof.ssa Arti Devi Ahluwalia

Tutor:

Prof. Emiliano Ricciardi

Controrelatore:

Prof. Nicola Vanello

Tutor:

Ing. Monica Betta

Laureando:

Valerio Fantozzi

Abstract

The autonomic nervous system, often known as the peripheral nervous system (PNS), is in charge of controlling the body's unconscious functions, through the complementary action of its main subdivisions, namely the sympathetic and the parasympathetic nervous systems.

During these years, clinical research has suggested that the breakdown of this subtle balance, arising as a sustained increase in the sympathetic tone could be implicated in the pathogenesis and/or in the progression of different cardio-vascular and metabolic diseases, including various forms of hypertension, myocardial infarction, cardiac arrhythmias, congestive heart failure and diabetes.

Moreover, frequent peripheral sympathetic activations during sleep have been associated with various sleep disorders, like obstructive sleep apnea, periodic leg movement syndrome and could serve a crucial role in sleep fragmentation and sleep disruption. Further investigation on these pathophysiological mechanisms, as well as the definition of reliable strategies for diagnosing should start from a wide-range assessment of the level of sympathetic activity across different conditions, including also sleep.

Unfortunately, standard techniques directly assessing sympathetic nerve activity are generally invasive for the patient, time-consuming and very difficult to record, and certainly detrimental to sleep quality. Microneurography in particular, is the gold standard technique for quantifying the muscle nerve sympathetic activity (MSNA), it involves implanted electrodes in the nerves to record the action potential generated by the axons, and, as a result, it's not a suitable procedure for large-scale monitoring.

In light of these premises, this work of thesis was concentrated in the analysis of a dataset in which the MSNA signal of 9 healthy volunteers was recorded simultaneously with different peripheral non-invasive bio-signals, including blood pressure, electrocardiographic (ECG) signal, photoplethysmographic (PPG) signal and air flow. After a baseline assessment, each subject performed different guided voluntary breathing maneuvers, in order to observe also non-steady-state relations. The final goal of the project was the development of tools able to systematically characterize potential relations between MSNA and peripheral non-invasive signals

and eventually identify surrogate non-invasive features that correlate with MSNA derived features and that could represent potential predictors of the level of sympathetic activity.

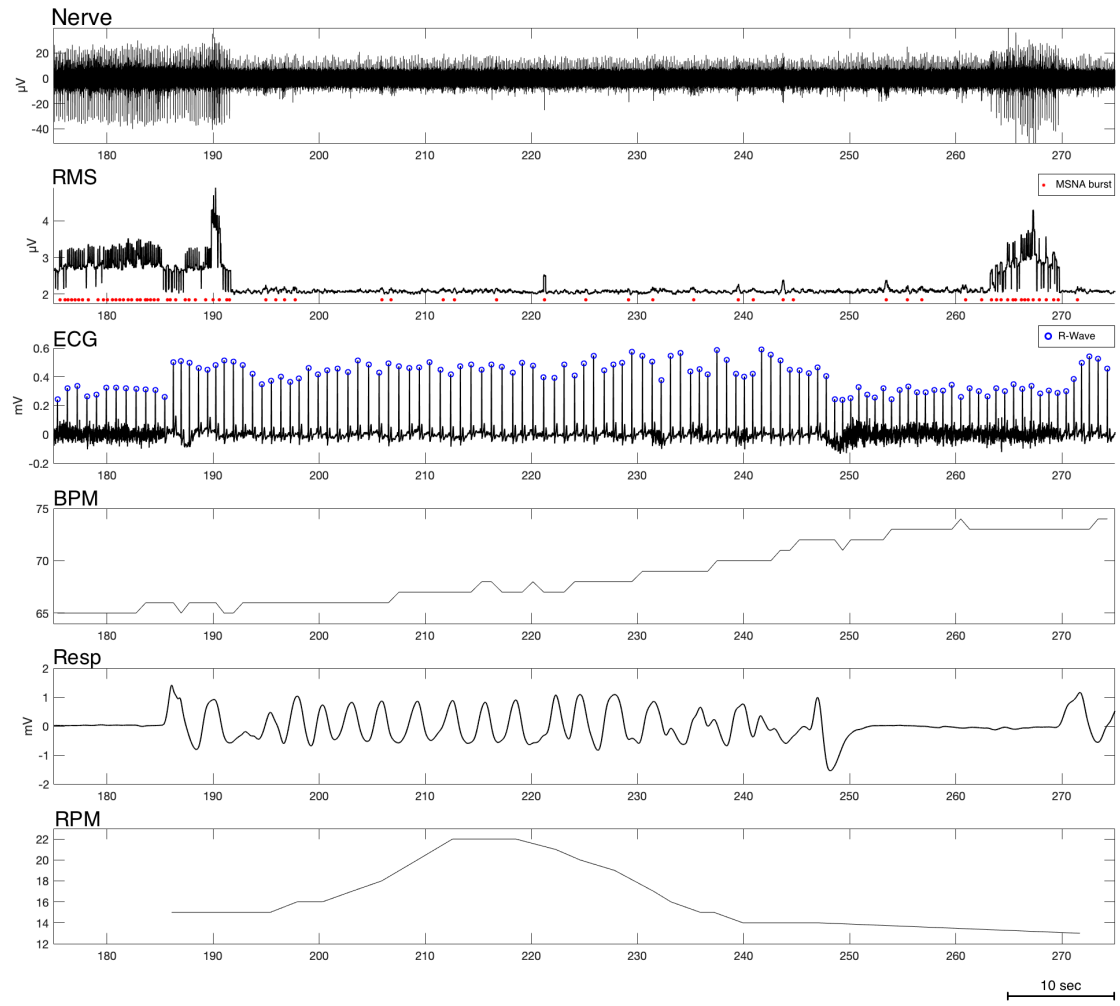


Figure: Multi-unit recording of muscle sympathetic nerve activity (MSNA) during an apnea-hypoventilation maneuver.

Therefore, a toolbox has been developed in the Matlab environment capable of carrying out an automatic analysis of all the signals before mentioned. Each signal was initially cleaned of artifacts, and then processed to extrapolate a wide range of features, that have been defined after an accurate revision of the corresponding literature. All data and features were optimally organized within the database in

order to allow easy accessibility for further analysis. Most attention was given to the raw MSNA signal, for which an automated procedure was defined that first attempts to reduce noise and then estimates the Mean Neurogram for each cardiac cycle, as well as detects and characterizes bursts of impulses in the MSNA. The goodness of extracted MSNA-based features was then assessed comparing their values and numerosity with those reported in previous studies, in which single MSNA bursts were visually scored by clinicians. Finally, a further module was implemented within the toolbox that estimates temporal relations between MSNA events and cardiac and respiratory events and inspects for consistent variations in the characteristics of MSNA features time-locked to peripheral events. In particular, were investigated variations potentially triggered by sudden drops in the pulse wave amplitude (PWA) signal, measured by finger photoplethysmography (PPG), that are known to reflect peripheral vasoconstriction.

— *Keywords* —

*Peripheral Nervous System - Muscle Nervous System (MSNA) - Microneurography -
Burst detection - Baroreflex delay - PWA drop*

Contents

1	Introduction	1
1.1	The nervous system	1
1.1.1	General anatomy	1
1.1.2	Information reception and interpretation	3
1.1.3	Central nervous system (<i>CNS</i>)	4
1.1.4	Peripheral nervous system (<i>PNS</i>)	4
1.1.5	Autonomic nervous system (<i>ANS</i>)	6
1.2	Microneurography	12
1.2.1	Action potentials and synapses	12
1.2.2	History	13
1.2.3	Recording technique	13
1.2.4	Sympathetic Nerve Activity (<i>SNA</i>)	18
1.2.5	MSNA Noise and analysis	20
1.2.6	MSNA quantification	21
1.3	Peripheral Bio-Segnals	22
1.3.1	Electrocardiogram (ECG)	22
1.3.2	Respiration	28
1.3.3	Photoplethysmogram (PPG)	31
1.4	Purpose of the study	32
2	Materials and methods	35
2.1	Data acquisition	35
2.1.1	Participants	35
2.1.2	Data Acquisition	35
2.1.3	Experimental Procedures	36
2.2	Processing pipeline	37
2.3	Pre-processing	37
2.3.1	Nerve Signal	38
2.3.2	ECG Signal	46
2.3.3	Respiration Signal	48
2.3.4	Cross-correlation between MSNA and ECG	57

2.3.5	PPG Signal	59
2.3.6	Data Structure	62
2.3.7	Graphical User Interface (GUI)	64
3	Results	66
3.1	Algorithm validation	66
3.1.1	R-peak Detection	66
3.1.2	Inspiration Peak Detection	70
3.2	MSNA burst analysis	71
3.2.1	Burst incidence in cardiac interval	71
3.2.2	Features analysis	74
3.2.3	Baroreflex delay	75
3.2.4	Baroreflex delay distribution	76
3.2.5	Respiration delay	79
3.2.6	MSNA-PWA relationship	80
4	Discussion	82

Chapter 1

Introduction

1.1 The nervous system

1.1.1 General anatomy

It is a common feature of all living organisms, the ability to interact with the surrounding environment from which they receive information of various kinds. Thus, the organism creates suitable reactions to restore the basic organism-environment balance (homeostasis) altered by the incoming information.

As the complexity of an organization grows, highly specialized cellular elements, neurons, take over these functions. They can both receive (afferent or sensory activity) and elaborate (efferent or motor activity) appropriate responses to incoming stimuli.

Both of these activities can be used to enable interaction with the external world (somatic activity, inherent in the life of relationship) or to the functioning of internal organs (visceral activity, inherent in vegetative life).

The nervous system is made up of all neurons of the organism, as well as their supporting cells, in which neurons aggregate in increasingly complex formations and tend to occupy a more central or axial location in the organism ([1] chapter 14.1)

Vertebrates are characterized by a *central nervous system (CNS)*, enclosed inside bone envelopes, and a *peripheral nervous system (PNS)*, comprised of all neural components that assure the link (afferent and efferent) with the rest of the body.

The *CNS* and the *PNS* interact to transmit and analyze the stimuli coming from the external environment and internal organs, resulting in a voluntary or involuntary reaction. These functions are linked to psychic activities, which include

emotional and cognitive processes, as well as behavior in general.

The *CNS* is responsible for processing afferent sensitive information, integrating it with previously acquired information, and generating efferent reactions.

The *PNS* is made up of structures (spinal nerves and encephalic nerves with their associated ganglia) that transfer impulses to and from extra-nervous organs and is located outside the bone envelopes (respectively afferent and efferent information). ([1] chapter 14.2).

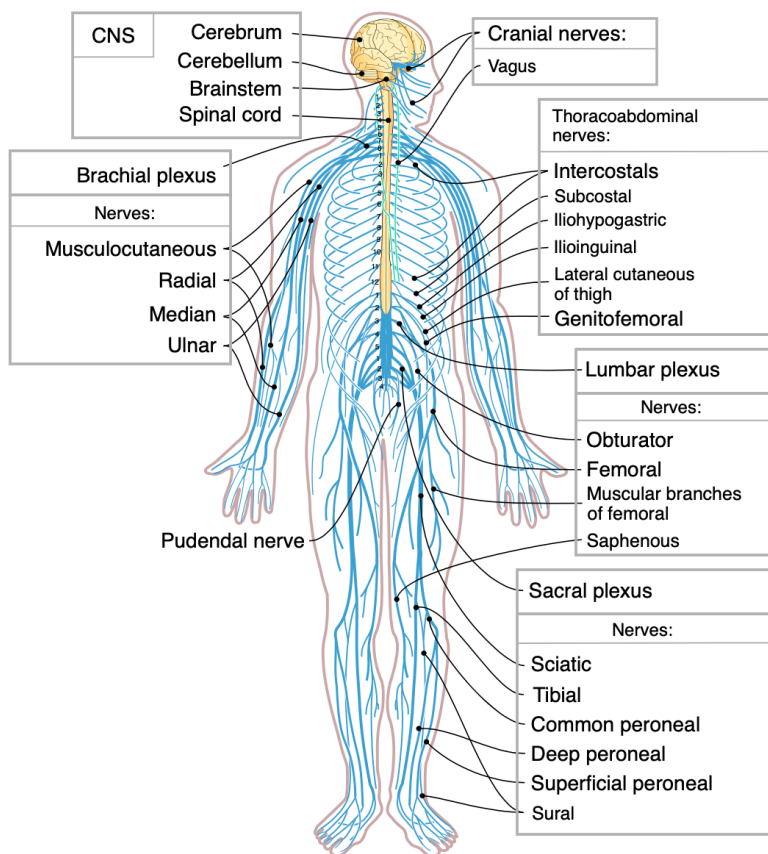


Figure 1.1: Model of human nervous system showing in yellow the Central Nervous System and in blue the Peripheral Nervous System (Image by:[1])

Sensory fibers (afferent fibers) carrying information from the periphery to the center and effector fibers (efferent fibers) directed to skeletal muscles, heart, smooth muscles, and exocrine and endocrine glands, make up the spinal and encephalic nerves, which connect the center with the periphery.

Both types of fibers can relate to both somatic (sensory and motor fibers) and vegetative (sensory fibers and effector fibers) activities ([1] chapter 14.1).

1.1.2 Information reception and interpretation

The presence of specific peripheral receptors capable of transmitting the message to the CNS via afferent nerve fibers enables the CNS to receive information.

Appropriate responses involving various levels of complexity can be obtained throughout this approach.

The most basic reaction is performed through reflex arcs, in which an afferent nerve fiber directly stimulates an efferent neuron (placed in the CNS) and so determines the motor response almost immediately after a sensory event.

The more sophisticated reactions need the activation of higher brain centers, to which the nerve message is delivered through ascending fiber bundles. As a result of the fine integration of the stimuli, the sensations originating in the periphery become perceptions (conscious sensations).

The type of receptors that have collected the peripheral stimuli are used to interpret the nerve message by the higher centers. These different types of sensitivity are carried to the higher centers by ascending pathways, anatomically distinct, which allow the detection of the type of stimulus and the location from which it originated.

Descending neural pathways drive the contraction of skeletal muscles as well as the behaviors of smooth muscles and glands in response to stimuli.

Smooth muscles and glands, particularly, respond to a subsection of the vegetative nervous system that is divided into sympathetic and parasympathetic systems.

Although the various subsections of the CNS are organized similarly, from the spinal cord to the most rostral parts of the brain, the increase in structural complexity is achieved by quantitative repetition of the same simple nervous circuits that form the structural pattern of all nevrasses ([1] chapter 14.1).

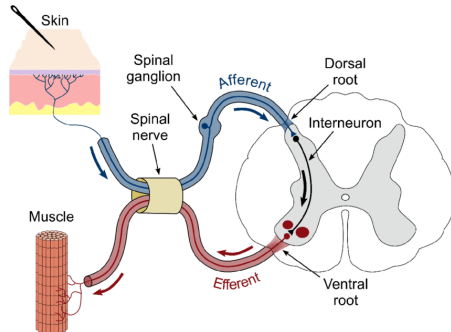


Figure 1.2: A diagram of a spinal reflex arc. A pin in the skin sends an input signal to the dorsal root of the spinal cord through the afferent route in the spinal nerve. The appropriate motor output leaves the ventral root and eventually reaches the muscle. The connection between the afferent (input) and efferent (output) pathways is mediated by the interneuron. (Image by [2])

1.1.3 Central nervous system (*CNS*)

Based on their anatomical locations, the CNS is divided into two groups:

- i) brain*, which is located inside the skull and
- ii) neuraxial system*, which is located inside the spinal column.

These two portions, which are anatomically connected at the level of the foramen magnum, exhibit differing external and internal conformation features.

The CNS is coated in three fibrovasacular layers, known as meninges, and has a series of interconnected cavities in its core, which are made by the central canal in the spinal cord and numerous ventricles in the brain.

The cerebrospinal fluid fills the central canal, the brain ventricles, and the subarachnoid space.

At the roof of the fourth ventricle, the exterior and internal compartments of the neuraxis are connected, resulting in the same pressure of cerebrospinal fluid in both compartments.

The blood-brain barrier, which sits between the blood compartment and the neural tissue, actively and selectively regulates the exchange of chemicals and cells. The CSF blood barrier, on the other hand, refers to the interface between the blood compartment and the cerebrospinal fluid ([1] chapter 14.2).

1.1.4 Peripheral nervous system (*PNS*)

The CNS is connected to the periphery, or to all of the body's non-nervous organs, via the PNS, which is divided into two parts:

- i) the peripheral somatic or voluntary nervous system*, that controls body movements through voluntary control of skeletal muscles,
- ii) and the autonomic or visceral nervous system*, that serves to innervate the viscera, vessels, and glands.

Furthermore, the peripheral system can be categorized into:

- i) an afferent (sensory) division that sends impulses to the CNS and*
- ii) an efferent (motor) division that sends impulses from the CNS to the peripheral organs to generate an effect or action.*

The *somatic nervous system*'s nerves originate directly from the inferior surface of the brain (cranial nerves) and laterally from the spinal cord (spinal nerves) and are distributed throughout the body's superficial and skeletal areas (skin, some mucous membranes, bones, muscles, joints and sense organs).

The somatic nervous system are under voluntary control, and transmits signals from the brain to end organs such as muscles.

The sensory nervous system is part of the somatic nervous system and transmits signals from senses such as taste and touch (including fine touch and gross touch) to the spinal cord and brain.

The *autonomic nervous system*'s nerves are responsible for transmitting to internal organs. They function automatically and continuously, without conscious effort to coordinate visceral activities that work together to maintain homeostasis.

The somatic and autonomic PNSs transmit effector impulses to peripheral organs in different ways.

In the first case, the effector impulse is delivered to the periphery by a single neuron (somatic motor neuron) that travels uninterrupted from the CNS that projects directly from the spinal cord or brain to the innervated organ.

In the second case, the stimulus is delivered to the effector organ by a pair of neurons: a preganglionic neuron whose soma is usually in the brainstem or spinal cord, in the CNS that is headed by a ganglion, and a postganglionic neuron that travels from the ganglion to the innervated organ ([1] chapter 15).

Structure

The PNS consists of *nerves* and *ganglia*, located outside the brain and spinal cord.

The basic unit of the PNS is the *nerve*, an enclosed, cable-like bundle of nerve fibers (called axons) that carries electrical impulses.

The electrochemical nerve impulses known as action potentials are transmitted, via a nerve, down each of the axons to peripheral organs or, in the case of sensory nerves, from the periphery back to the CNS.

Within the nerve, each axon is an extension of a single neuron, along with other supporting cells like Schwann cells, which coat the axons with myelin.

Each axon in a neuron is wrapped by an endoneurium, a layer of connective tissue. Each fascicle is covered in a layer of connective tissue called the perineurium, which bundles the axons into groups called fascicles. Lastly, the epineurium is a layer of connective tissue that wraps around the entire nerve.

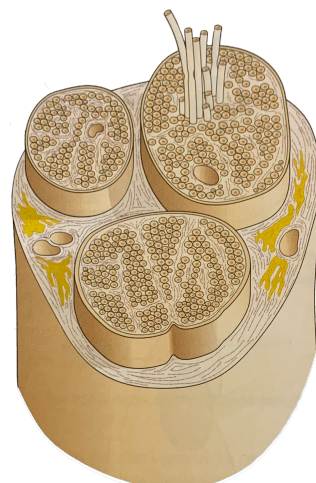


Figure 1.3: Structure of a nerve in cross section (Image by: [1])

Nerve cells (also known as neurons) are divided into sensory, motor, and mixed nerves .

The individual neurons that make up a nerve carry information in the form of electrochemical impulses (known as action potentials).

The impulses travel at rates of up to 120 m/s from one neuron to another by crossing a synapse, where the message is converted from electrical to chemical and then back to electrical.

Nerves are divided into two classes based on their function:

- i) An afferent nerve fiber carries sensory information from a sensory neuron to the CNS, which processes it. Nerves are bundles of fibres or axons in the PNS, while sensory nerves are bundles of afferent fibers.
- ii) Signals from a motor neuron in the CNS are sent to muscles through an efferent nerve fiber. Efferent nerves are collections of these fibers.

1.1.5 Autonomic nervous system (*ANS*)

The *ANS*, also known as the vegetative nervous system, is the unit of the nervous system (*NS*) that controls the organism's visceral processes, as already mentioned previously. It's essentially an effector system in charge of smooth muscle, cardiac muscle, and glandular function control.

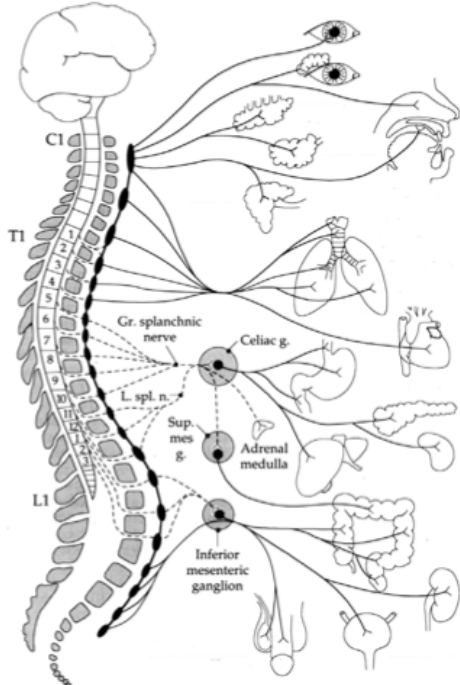
It modulates cardiac output and arterial pressure, gastric and intestinal activities, glandular secretions, and many other visceral functions, with the help of the endocrine system in many circumstances.

It has a faster reaction rate than the endocrine system, being able to respond to changes in the internal environment very quickly, even within a few seconds, ensuring quick recovery of stable conditions.

The *ANS* is named after the fact that regulatory functions are not directly controlled by the will. Higher centers in the CNS can, however, influence its actions in a more or less direct way.

On the basis of morphological, neurochemical and functional differences, it is possible to distinguish two main subsections in the *ANS*: the *sympathetic* system and the *parasympathetic* system. There is also a third subsection, the *enteric* system, that regulates the gastrointestinal system [3].

Sympathetic



Parasympathetic

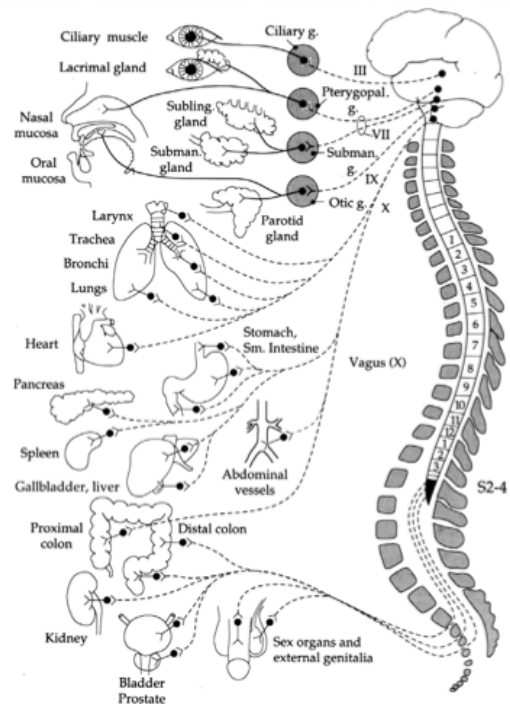


Figure 1.4: Schematic overview of sympathetic and parasympathetic innervation. The organs have been labeled on the right, on the left only those parts that are particular to the sympathetics. Dotted lines: preganglionic, solid: postganglionic fibers (Image by:[4])

The sympathetic division consists of cells with soma in the lateral grey column. It originates in the thoracic and lumbar areas of the spinal cord and ends around L2-L3.

The parasympathetic division has craniosacral outflow, meaning that the neurons begin at the cranial nerves (specifically the oculomotor nerve, facial nerve, glossopharyngeal nerve and vagus nerve) and sacral (S2-S4) spinal cord [5].

Autonomic nerves travel to organs throughout the body. Most organs receive parasympathetic supply by the vagus nerve and sympathetic supply by splanchnic nerves. At certain spinal segments, the sensory portion of the latter reaches the spinal column. Pain in any internal organ is perceived as referred pain, more specifically as pain from the dermatome corresponding to the spinal segment.

The ANS's distinctive functions are aimed at maintaining the internal medium's homeostasis.

This result is largely guaranteed by the mostly antagonistic influences that the two systems (*sympathetic* and *parasympathetic*) exert on the functions of the different organs and systems.

In fact, almost all organs are innervated by both, with the exception of sweat glands, piloerector muscles, and the majority of blood vessels, which are only innervated by sympathetic stimuli.

Organ	Sympathetic activation	Parasympathetic activation
Eye		
Pupil	Dilation (dilator muscle)	Constriction (sphincter muscle)
Ciliary muscle	Relax (far vision)	Constrict (near vision)
Lacrimal gland	Slight secretion	Secretion
Salivary glands	Slight secretion	Secretion
Heart		
Rate (sinus node)	Increase	Decrease
Contractility (muscle)	Increase	Decreased or none
Lungs	Bronchodilation	Bronchoconstriction
Gastrointestinal tract	Decreased motility	Increased motility
Kidney	Antidiuresis (decreased output)	None
Bladder		
Detrusor muscle	Relaxation	Contraction
Sphincter	Contraction	Relaxation
Penis	Ejaculation	Erection
Clitoris, labia minora	None	Swelling/erection
Nipples	None	Erection
Sweat glands	Secretion	Palmar sweating
Piloerector muscles	Contraction	None
Blood vessels		
Large arteries	Constriction	None
Arterioles	Constriction	None
Precapillary sphincters	Constriction	None
Venules	Constriction	None
Large veins	Constriction, volume mobilization	None
Coronary arteries	Dilatation	None
Muscle		
Arterioles	Dilatation	None
Metabolism	Increased	None
Muscle spindles	Decreased sensitivity	None
Liver	Glycolysis, glucose mobilization	Glycogen synthesis
Fat tissue	Lipolysis	None
Immune system	Suppressed	Activated

Figure 1.5: Main Autonomic Nervous System Sympathetic and Parasympathetic Stimulation (Table by: [3])

The activity of the sympathetic system manifests itself particularly in conditions in which the organism faces with emergency situations or stress. It has been associated with *fight or flight* reactions. In fact, sympathetic system activation causes a rise in heart rate, arterial pressure, and blood supply to the care and nerve centers, as well as suppression of gastrointestinal functions, hyperglycemia, and catabolic processes. Burning energy resources enriches the blood with all metabolic substrates that the body can use to maintain a constant defensive or offensive response.

Activation of the parasympathetic system, on the other hand, predominates in conditions of stability (rest and digest). It promotes digestive functions, reduces heart rate and blood pressure, and has a pronounced anabolic activity in terms of renewing energy reserves.

The ANS operates mainly through visceral reflex arches that have similarities, at least in their general organization, with the somatic reflex arches that control skeletal muscles.

From the receptors, the afferent information (visceral) reaches the centers of the CNS (spinal cord, brain stem) from which efferent commands occur after appropriate integration processes, and they reach the effector organs via the ANS fibers.

The mechanisms in which the ANS innervates the target organs differ from the somatic motor system in several ways.

The somatic motor pathway is typically monosynaptic, consisting of a single efferent neuron located inside the CNS in the anterior horns of the spinal cord or motor nuclei of the cranial nerves. It connects directly to the skeletal muscles it innervates, with no intermediary steps. The soma is located within the CNS and the axons directly innervate the skeletal muscle.

The vegetative efferent pathways, on the other hand, are typically disinaptic. The efferent neuron does not directly affect the target organs; instead, its fiber generally terminates in a ganglion, where it forms synapses with a second neuron.

The ganglion is generally next to the innervated organ, and the postsynaptic neuron's axon is not myelinated. The innervated organs will be influenced by the fiber of the ganglionic neuron, also known as the visceral motor neuron.

As a result, in the ANS, we distinguish between a preganglionic fiber (neuron) with a cell body in the CNS and a postganglionic fiber (neuron) with a cell body in the ganglion and innervates the viscera.

Another distinction between the somatic nervous system and the ANS is the mechanism behind inhibitory events. Because somatic motor neurons are exclusively excitatory, skeletal muscle relaxation cannot be achieved through direct inhibitory actions on the muscle fiber, but rather as a disfacilitating phenomenon, i.e. as a result of the motor neuron that controls it being inhibited.

In the ANS, the inhibitory effect can be direct, meaning that the released neurotransmitter and its interaction with its own receptor can cause the visceral fibers to exert excitatory or inhibitory effects directly on the target organ [3, 5].

Sympathetic nervous system (*SNS*)

Many homeostatic functions in living organisms are regulated by the SNS.

SNS fibers innervate tissues in almost every organ system, allowing them to regulate processes as diverse as pupil diameter, gut motility, and urine system.

It's best recognized for regulating the fight-or-flight response, which is a neuronal and hormonal stress response.

This response is also known as sympatho-adrenal response of the body, as the preganglionic sympathetic fibers that end in the adrenal medulla (but also all other sympathetic fibers) secrete acetylcholine, which activates the great secretion of adrenaline (epinephrine) and to a lesser extent noradrenaline (norepinephrine) from it. As a result, this response, which predominantly affects the cardiovascular system, is mediated both directly and indirectly through SNS impulses and catecholamines released by the adrenal medulla.

The SNS is in charge of stimulating the body for action, especially in situations where survival is at risk. For example, in the moments before waking, sympathetic outflow rises spontaneously in preparation for action.

SNS stimulation causes vasoconstriction of most blood vessels, including many of those in the skin, the digestive tract, and the kidneys. This occurs as a result of activation of alpha-1 adrenergic receptors by norepinephrine released by post-ganglionic sympathetic neurons. These receptors exist throughout the vasculature of the body but are inhibited and counter balanced by beta-2 adrenergic receptors (stimulated by epinephrine release from the adrenal glands) in the skeletal muscles, the heart, the lungs, and the brain during a sympathoadrenal response.

The net effect is a shunting of blood away from organs that aren't critical to the organism's immediate survival and an increase in blood flow to tissues that are involved in severe physical activity.

The ANS's afferent fibers, which convey sensory information from the body's internal organs to the CNS, are not differentiated into parasympathetic and sympathetic fibers like the efferent fibers are. Autonomic sensory information is instead transmitted by nonspecific visceral afferent fibers.

General visceral afferent sensations are mainly unconscious visceral motor reflex sensations supplied to the CNS through hollow organs and glands. While the unconscious reflex arcs are typically undetectable, they can occasionally send pain sensations to the CNS, masked as referred pain. This pain is typically non-localized and referred to dermatomes on the same spinal nerve level as the visceral afferent synapse [6, 1].

Parasympathetic system (*PSNS*)

The PSNS is in charge of stimulating 'rest-and-digest' or 'feed-and-breed' functions, such as sexual arousal, salivation, lacrimation, urination, digestion, and defecation, that occur when the body is at rest, especially after feeding. Its effect can be described as complimentary to that of the SNS, which is in charge of activating fight-or-flight behaviors.

The PSNS derives its nerve fibers from the CNS.

Owing to its location, the PSNS is often referred to as having 'craniosacral outflow', in contrast to the SNS, which is referred to as having 'thoracolumbar outflow' [6, 1].

1.2 Microneurography

1.2.1 Action potentials and synapses

Neurons are essentially electrical devices and talk to each other across synapses.

Action potentials are the fundamental units of communication between neurons and occur when the sum total of all of the excitatory and inhibitory inputs makes the neuron's membrane potential reach around -50 mV, a value called the action potential threshold (See Fig.1.6).

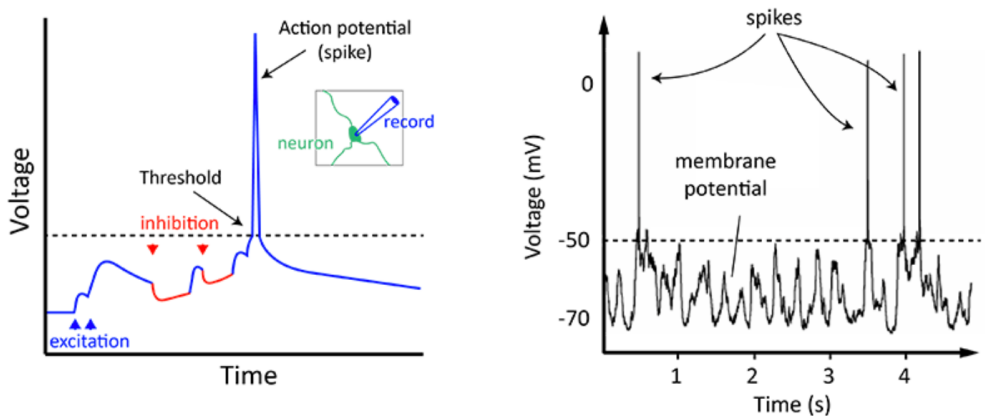


Figure 1.6: A neuron spikes when a combination of all the excitation and inhibition it receives makes it reach threshold. On the right is an example from an actual neuron in the mouse's cortex. (Image by: [7])

When an action potential reaches the presynaptic terminal, it causes neurotransmitter to be released from the neuron into the synaptic cleft. After travelling across the synaptic cleft, the transmitter will attach to neurotransmitter receptors on the postsynaptic side, and depending on the neurotransmitter released, particular positive (e.g. Na^+ , K^+ , Ca^+) or negative ions (e.g. Cl^-) will travel through channels that span the membrane.

Synapses can be thought of as converting an electrical signal (the action potential) into a chemical signal in the form of neurotransmitter release, and then, upon binding of the transmitter to the postsynaptic receptor, switching the signal back again into an electrical form, as charged ions flow into or out of the postsynaptic neuron.

Neuroscientists often refer to action potentials as *spikes*, or say a neuron has *fired a spike*. The term is a reference to the shape of an action potential as recorded using sensitive electrical equipment (See Fig.1.6).

1.2.2 History

Autonomic activity in humans was previously estimated by measuring effector responses (e.g., heart rate, blood pressure, muscle/skin conductance, sweating) or neurotransmitter concentrations in the blood.

In the department of clinical neurophysiology at the Academic Hospital in Uppsala, Sweden, Hagbarth and Vallbo developed the technique of microneurography in the mid-1960s [8, 9].

The original purpose of human microneurographic recording was to investigate the muscle spindle and its role in motor control. The technique also proved capable of recording afferent multiunit nerve activity from skin and muscle in response to mechanical skin stimuli and voluntary movements.

In one of the first published microneurographic recordings [8], the microelectrode was inserted into a cutaneous nerve bundle in the popliteal fossa. Multiunit cutaneous impulses were recorded in response to tapping and more prolonged pressure in the area of innervation.

As a result of these early experimental breakthroughs and successes, it quickly became apparent that microneurography could be used as a tool to directly measure neural activity generated by individual axons, including efferent sympathetic axons, i.e, the unmyelinated postganglionic sympathetic fibers.

Hundreds of later studies, utilizing the technique of microneurography, were driven by the discovery that bursts of efferent postganglionic SNS activity could be directly recorded from awake humans.

Microneurography is currently the only electrophysiological recording technology capable of measuring either multi-unit and single-unit activity in peripheral nerves.

1.2.3 Recording technique

Sympathetic microneurography requires tungsten needle electrodes that are inserted through the skin without anesthesia and directed into a peripheral nerve.

The recordings are possible due to three anatomical characteristics:

- i)* The perineurium, a high impedance fibrous barrier that inhibits crosstalk between nearby fascicles, surrounds each fascicle in peripheral nerves.
- ii)* All nerve fibers in a fascicle are destined for the same tissue near the target of innervation. As a result, when an electrode is put into the distal part of a fascicle, all action potentials will come from fibers that are going to or coming from that type of tissue.

iii) Individual sympathetic neurons can sometimes be found dispersed within a fascicle, although most sympathetic fibers are found in bundles. Because the unmyelinated fibers are surrounded by myelinated fibers, current distribution is limited, allowing the electrode tip to record from one sympathetic fiber (single unit recording) or many sympathetic fibers simultaneously (multiunit recording).

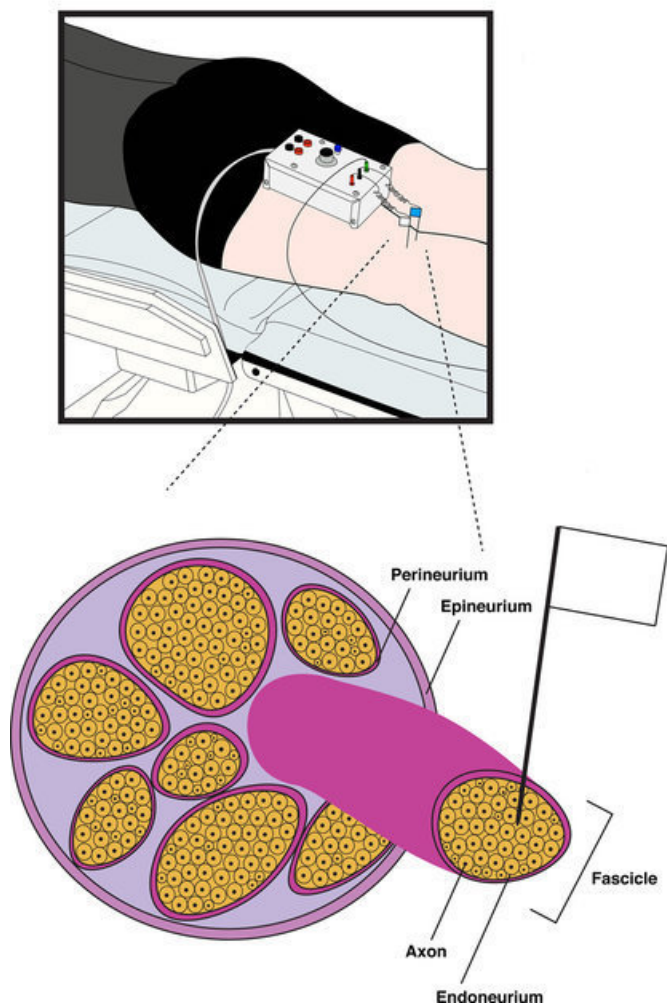


Figure 1.7: Human microneurography technique. Top: Experimental arrangement for recording from the tibial nerve at the knee level (popliteal fossa). The active electrode is placed into the nerve, while the reference electrode is implanted beneath the skin near the nerve. Bottom: A schematic of a peripheral nerve is shown, with the active electrode inserted into a single nerve fascicle, directly adjacent to a single axon (i.e., intrafascicular extracellular recording) (Image by: [10])

Because of its electrical (conduction) and mechanical (thin, rigid, and nonbrittle) qualities, tungsten is the metal of choice for percutaneous nerve implantation.

The microelectrode, typically with a shaft diameter of $200\text{ }\mu\text{m}$ and a rounded tip of $5\text{ }\mu\text{m}$ in diameter, is placed percutaneously through unanesthetized skin and carefully positioned into an underlying peripheral nerve in awake humans during microneurography. As a reference electrode, a second subdermal microelectrode is implanted 1 cm apart from the active recording electrode[11].

The peroneal, popliteal, radial, median, and ulnar nerves are the most widely used peripheral nerves, primarily for practical reasons.

The electrodes are connected to a grounding unit and a preamplifier, with further amplification and filtering occurring in the main amplifier.

Because unmyelinated (C-fibre) sympathetic axon action potentials are so weak, they must be amplified 20,000 times via an electrically separated headstage near the recording site. The mean power in the baseline between bursts is approximately $1.8\text{ }\mu\text{V}$, and the peak-to-peak background noise is approximately $10\text{ }\mu\text{V}$. Such low noise levels and high signal to noise ratio indicate a high-quality recording [12].

Most commercially available headstages pre-amplify the signal 10–100 times before sending it to the main amplifier for further amplification and filtering.

To reduce electrical interference, the cables connecting the headstage to the microelectrodes must be maintained short (no more than 10 cm). In fact, long leads attached to a high-impedance micro-electrode behave as antennae, picking up electrical noise.

Each tungsten electrode used to record SNA is epoxy insulated except for the electrode tip, which remains uninsulated. The epoxy insulation can vary in thickness, allowing for a wide variety of electrode impedances that affect the recording area ($50\text{ k}\Omega$ to $10\text{ M}\Omega$; generally $1\text{-}2\text{ M}\Omega$ at 1 kHz) [13].

Low-impedance microelectrodes (less than $50\text{ k}\Omega$) often record low-amplitude multi-unit activity made up of tiny spikes generated at a distance from the micro-electrode tip, referred to as far-field activity [12]. Conversely, for oligounitary and especially unitary recordings, a high-impedance microelectrode is necessary .

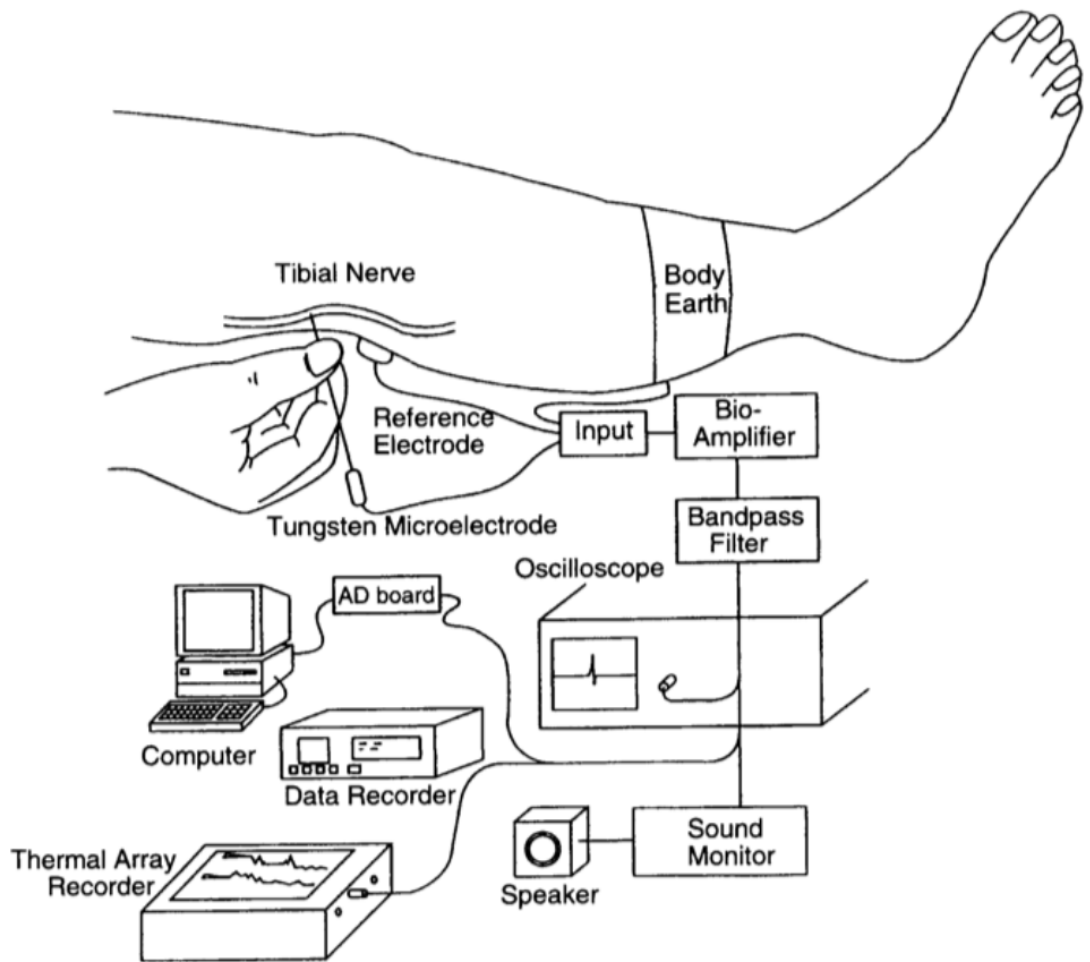


Figure 1.8: An illustration of the human microneurography recording setup. The signal from the tungsten electrode placed in the tibial nerve is filtered in a bandpass filter before being amplified and collected. (image by: [14])

Sympathetic nerve activity is usually recorded from the common peroneal nerve (also known as the fibular nerve) as it courses behind the fibular head, though the Japanese favour the tibial nerve, which they enter through the popliteal fossa. They employ forceps to introduce the microelectrode through the skin and use a considerably longer and more flexible tungsten microelectrode than the typical microneurography needle, which has a shaft diameter of 0.2 mm.

The triceps surae muscles and the intrinsic muscles of the foot are supplied by fascicles, whereas the plantar and lateral parts of the foot are supplied by cutaneous fascicles.

The common peroneal nerve is used in most other laboratories because, with one exception, it is composed of distinct fascicles that supply either the pretibial flexors (tibialis anterior, toe extensor muscles, or peronei muscles) or skin on the dorsum of the foot or anterolateral aspects of the leg at the level of the fibular head (and an occasional fascicle on the medial aspect of the foot).

Other nerves, such as the median and ulnar nerves in the upper arm, are even more mixed, with less fascicular architecture in proximal subsections of limb nerves and mixing within the nerve in the cutaneous and muscle areas [12].

1.2.4 Sympathetic Nerve Activity (SNA)

Multiunit sympathetic activity occurs of 'bursts' of impulses separated by quiet intervals of varied length and can be categorised in Muscle (*MSNA*) (see Fig.1.9.A) and Skin (*SSNA*) (see Fig.1.9.B) Sympathetic Nerve Activity.

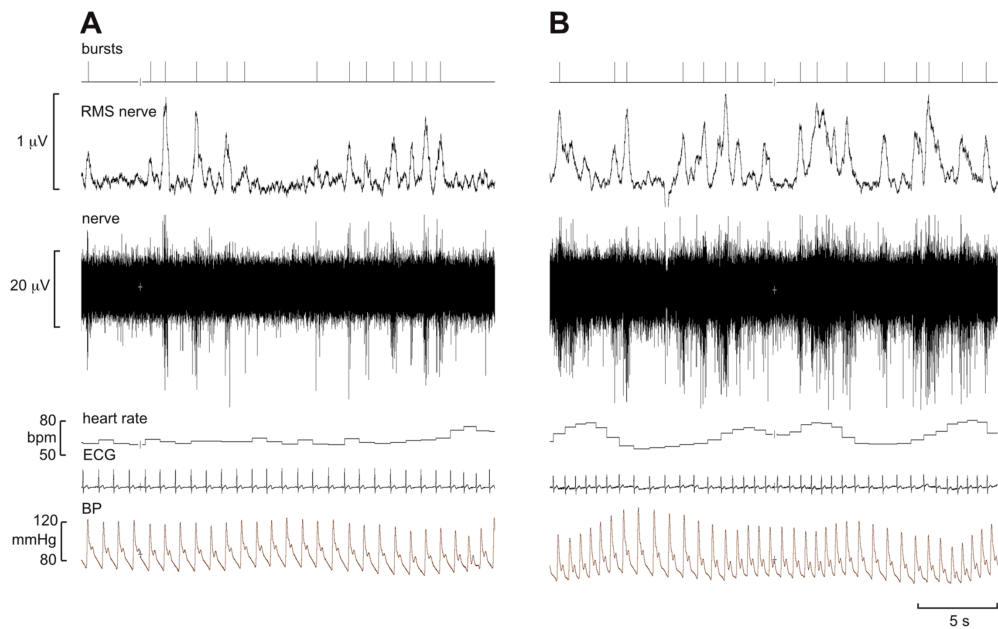


Figure 1.9: Multi-unit recordings of spontaneous bursts of MSNA (a) and SSNA (b) in two participants. (Image by: [15])

The bursts exhibit different morphologies and temporal patterns depending on whether the active recording microelectrode is inserted into a muscle or a skin nerve fascicle, and they can be induced by different stimuli. The microneurographer can correctly identify recordings as either efferent MSNA or SSNA based on these differences.

MSNA core objective is vasoconstrictor, and its major purpose is to buffer sudden drops in blood pressure via the baroreflex, allowing for a constant perfusion pressure. MSNA is also affected by respiration, with levels dropping during inspiration and rising during expiration [16, 17]. MSNA remains constant in a given individual, day to day, year to year [18].

At rest, some subjects have high MSNA levels, while others have low levels.

Searching for MSNA is facilitated by asking the participant to perform an inspiratory-capacity apnea (maximal inspiratory breath-hold) or an end-expiratory apnea or a Valsalva manoeuvre, each of which increases MSNA.

The primary role of sympathetic outflow to the skin (SSNA) is to control heat loss from the body, through its actions on sweat glands, cutaneous blood vessels, and, phylogenetically, the hairs. In addition to its role in thermoregulation, it has been associated with emotional expressiveness, showing activity rising in response to short arousing stimuli [19] or moments of increased emotional involvement [15]. The major elements of skin sympathetic nerve activity supplying hairy skin are cutaneous vasoconstrictor and sudomotor activity. Most diseases that affect MSNA have little effect on skin sympathetic nerve activity. The majority of the conditions that affect SSNA are found to be correlated with thermoregulation.

The efferent SNA to muscle (MSNA) and skin (SSNA) have various distinguishing characteristics that allow the two signals to be distinguished on a real-time mean voltage neurogram [20].

The more typically recorded MSNA has a pulse-synchronized burst pattern, with a burst occurring ~ 1.3 seconds following the R wave on an ECG. Importantly, MSNA burst confirmation can be enhanced by having the participant conduct a voluntary end-expiratory apnea, which triggers MSNA increases.

Instead, a sudden startle stimulus, such as a yell or a loud clap, has no effect on MSNA.

SSNA, on the other hand, is not pulse synced, and the shape of the burst is much more unpredictable. When compared to the acute, distinct MSNA shape, SSNA bursts are commonly longer, broader, and shallower. Furthermore, a startle stimulus (e.g., a yell or clap) as well as mild skin stroking cause significant increases in SSNA.

Before starting with an MSNA or SSNA experiment, it is critical to undertake these auditory and physical confirmation tests to guarantee that only one signal (MSNA or SSNA) is being recorded.

SSNA is only weakly influenced by the baroreflex and plays a minor role in blood pressure (BP) regulation [19]. Thus, MSNA should be recorded when a research issue is largely focused on sympathetic regulation of blood pressure, while SSNA should be recorded when measuring thermoregulatory control of cutaneous blood flow [21].

The skin and muscular nerve fascicles are anatomically proximal to one another, and fibers from one type of fascicle may cross over to the other. Because of these anatomic features, it is possible to have both MSNA and SSNA signals mixed within the same neurogram. Because both signals interfere with burst detection, quantification, and mechanistic interpretation, this may and should be avoided.

1.2.5 MSNA Noise and analysis

Electrical noise is a neurophysiologist's greatest enemy, and it's worth thinking about ways to reduce it.

Amplifiers for microneurography are, like those for other neurophysiological applications, differential amplifiers. Modern amplifiers feature a high input impedance, which ensures that the voltage taken up by the recording (active) microelectrode is kept as high as possible without current leakage into the amplifier.

Because the input impedance and electrode impedance are both high, anything between the tip of the microelectrode (the recording surface devoid of insulation) and the input terminals of the headstage, the connecting wires, will act as electrical noise antennae. However, the most significant sources of noise (the line frequency of the power supply, 50 or 60 Hz), as well as sources of higher frequency components, such as computer monitors and fluorescent lights, are found within the laboratory (i.e. data acquisition and monitoring equipment).

There's a limit to how much noise we can eliminate, but having a high pass filter of 100 Hz or more, as well as a headstage that preamplifies the signal by at least 10 times, helps.

The background noise for a typical high-impedance (approximately $15\text{ M}\Omega$) microelectrode will be approximately $20\text{ }\mu\text{V}$ peak-to-peak [12].

When the microelectrode tip loses some of its insulation, through repeated passage through fascicles or the nerve sheath or skin (one should avoid removing the microelectrode completely and reinserting through the skin), the background noise becomes appreciably smaller and the recording capacity of the microelectrode will be compromised: at impedances typically less than 100 k, the microelectrode will only pick up far-field nerve activity.

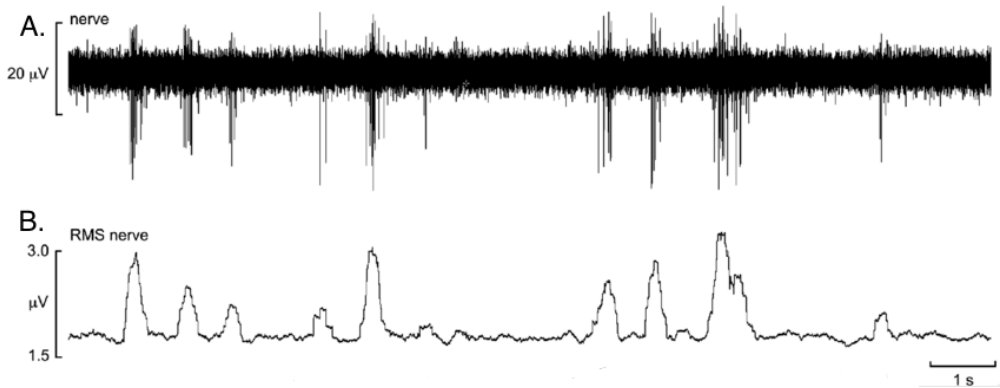


Figure 1.10: Multi-unit recordings of spontaneous bursts of MSNA a) raw signal and b) filtered signal (Image by: [12])

While consistent recordings of sympathetic nerve activity can be produced for much over an hour, potential changes in the recording site over time must be considered. The microelectrode should remain at a stable intrafascicular site for a long period if the nerve is quite deep and the microelectrode is properly supported by the tissues overlaying the nerve.

When the nerve is superficial, unfortunately, the microelectrode may tend to slip out due to gravity's effects, especially if oriented upwards towards the nerve. This will be observed as a downward shift in the mean-voltage neurogram's baseline, which may be gradual or abrupt.

1.2.6 MSNA quantification

The most commonly accepted approach for quantifying MSNA is to evaluate [22, 23, 24, 25, 12]:

- i) the burst rate over the recorded time period, which is given in bursts per minute

$$\text{burstFrequency} = \text{bursts}/\text{min}$$

- ii) number of bursts per 100 heart beats

$$\text{burstIncidence} = \text{burst}/100\text{HeartBeats}$$

- iii) area underneath the burst

$$\text{burstArea} = \int_{\text{burst}} \text{nerveSignal} * dt$$

Burst frequency characterise the average SNA that the vascular smooth muscle is exposed to over a given time period.

Burst incidence, on the other hand, measures how frequently bursts occur in relation to the total number of heartbeats available.

Both ways of quantifying burst rate/occurrence should be reported. An increase in burst frequency could be caused by an increase in burst incidence, an increase in heart rate, or a combination of the two.

1.3 Peripheral Bio-Segnals

1.3.1 Electrocardiogram (ECG)

The electrocardiogram is a visual representation of the heart's electrical activity.

Low-intensity electric fields can be detected on the surface of the human body, particularly at the level of the trunk, mostly caused by the heart's periodic depolarizations and repolarizations.

A device called electrocardiograph is used to record these small voltages.

The acquired signal is converted into an electrocardiographic trace, which is the simplest way to examine heart's electrical activity.

The normal ECG trace has a distinct appearance: it consists of a series of positive (*P*, *R*, *T*) and negative (*Q*, *S*) deflections, referred to as *waves*, separated by some straight lines, referred to as *segments*. Positivity or negativity refers to the *isoelectric line*.

The QRS complex is made up of three waves that repeat itself. The *Q wave* is a negative, small wave that corresponds to the interventricular septum depolarization. The *R wave* is a very high positive peak that corresponds to the depolarization of the apical part of the ventricles; it is so noticeable because it is linked to the most relevant muscle mass, particularly that of the left ventricle. The *S wave* is a negative wave that, like the *Q*, is small in size and represents depolarization of the left ventricle's basal and posterior regions.

The interval between two QRS complexes can be used to estimate a regular heart rate.

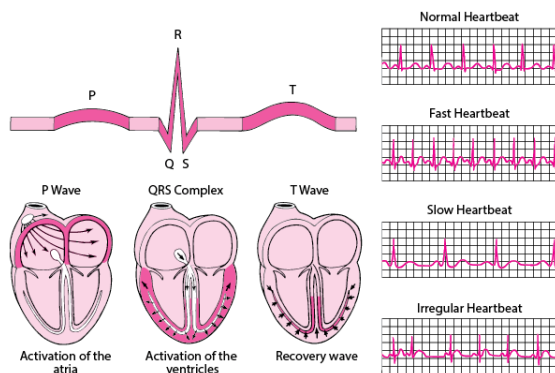


Figure 1.11: Elements of the ECG-complex. On the left is shown the PQRS wave where the P-wave appears due to the atrial activation, an R-peak does due to the ventricular activation and a T-wave does due to the ventricular relaxation. On the right is shown the electrocardiogram (graphic recording of the electrical activity of the Heart) (Image by: [26])

Baroreflex System

Heart rate is largely controlled by the heart's *internal pacemaker activity*.

The main pacemaker in a healthy heart is a group of cells called the sinoatrial node, which is located on the border of the atria and vena cava. As a result, the node's cells create electrical activity on their own, which is then carried throughout the heart, resulting in a regular heart beat.

In absence of any external stimuli, sinoatrial pacing helps to keep the heart rate between 60 and 100 beats per minute.

At the same time, the two branches of the ANS increase or slow the heart rate in a complementary manner.

Heart is under the influence of both the sympathetic and parasympathetic nerve system, being served from the cardiac plexuses, mainly located around the atria.

The fundamental relationships among main arterial pressure (MAP), cardiac output (CO) and total peripheral vascular resistance (TPR) are based on the hydraulic equivalent of Ohms Law [6, 27]:

$$MAP = CO * TPR$$

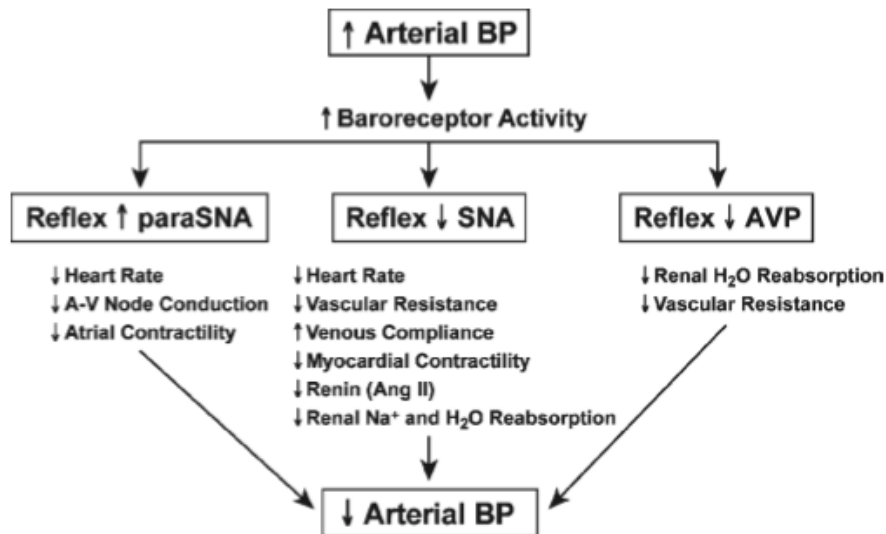


Figure 1.12: Baroreceptor reflex control of arterial blood pressure (BP). Increases in baroreceptor activity during a rise in BP evokes reflex activation of para-SNA, inhibition of SNA, and inhibition of arginine vasopressin (AVP) release. The resulting cardiovascular, hormonal, and renal adjustments reduce BP in a negative feedback manner. Opposite reflex responses are evoked during decreases in arterial BP. (image by: [28])

Changes in blood pressure are sensed by mechanosensitive afferent nerve endings called baroreceptors, located primarily in the carotid sinus and aortic arch, as well as in the pulmonary great vessels, atria and ventricles.

The arterial baroreflex is responsible for the dynamic inverse relationship between sympathetic nerve activity and arterial blood pressure[29].

Arterial baroreceptor afferents project via the glossopharyngeal and vagus nerves to the nucleus tractus solitarii (NTS), in the dorsal medulla. The NTS is the primary site of cardiorespiratory reflex integration, and recruits specific neural pathways to generate appropriate autonomic adjustment in order to maintain arterial blood pressure within a narrow range of variation.

The activation of the baroreceptor afferents cause the walls of blood vessels to stretch more and consequently an increase in blood pressure [30].

The reflex inhibition of efferent sympathetic pre- and postganglionic activity occurs when afferent firing increases (due to increased blood pressure).

The arterial baroreceptor reflex, in its most basic form, functions as a classic negative feedback system that senses, controls, and resenses blood pressure in a rapid and dynamic way.

This indicates that the sympathetic system is in charge of regulating pressure and distributing flow on a global scale, acting in concert with local mechanisms to fine-tune supply and demand. The vascular smooth muscle cell (VMC) is the active component of blood vessels that controls their diameter[31, 6].

Baroreflex delay

This dynamic negative feedback relationship with blood pressure is also the source of sympathetic nerve activity's cardiac rhythmicity: the baroreceptors detect each systolic pressure wave and elicit reflex inhibition[19].

The baroreceptors trace each systolic pressure wave and cause reflex inhibition, or a pause in the neurogram. During diastole, on the other hand, blood pressure falls, the inhibition wears off, and a burst may occur. Each cardiac cycle is, in this way, a small baroreflex cycle of inhibition and disinhibition.

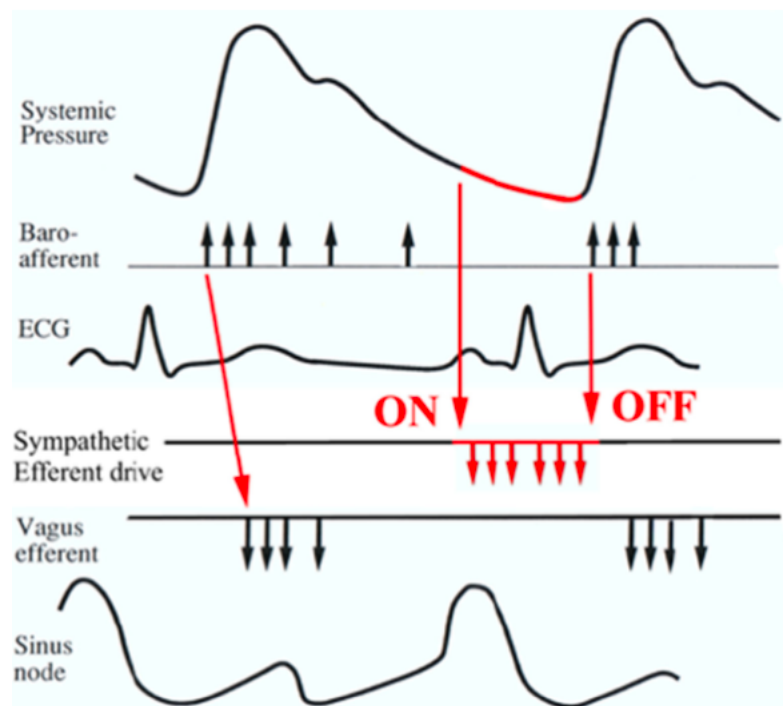


Figure 1.13: Schematic time relations of baroreceptor afferent activity and feedback via sympathetic and vagus nerve efferents to the sinus node (Image by: [6])

In agreement with this there is a relatively reproducible mean baroreflex latency from the start of the systolic pressure wave (or the R wave in the ECG) to the peak of corresponding burst in the mean voltage neurogram.

To quantifying MSNA relative to cardiovascular control, it is necessary to compensate for the delay in the baroreflex arc. The average delay time is greater in tall individuals than in the short ones, however the average delay time is usually about 1.2 to 1.3 seconds [12, 13, 20, 27, 30, 32].

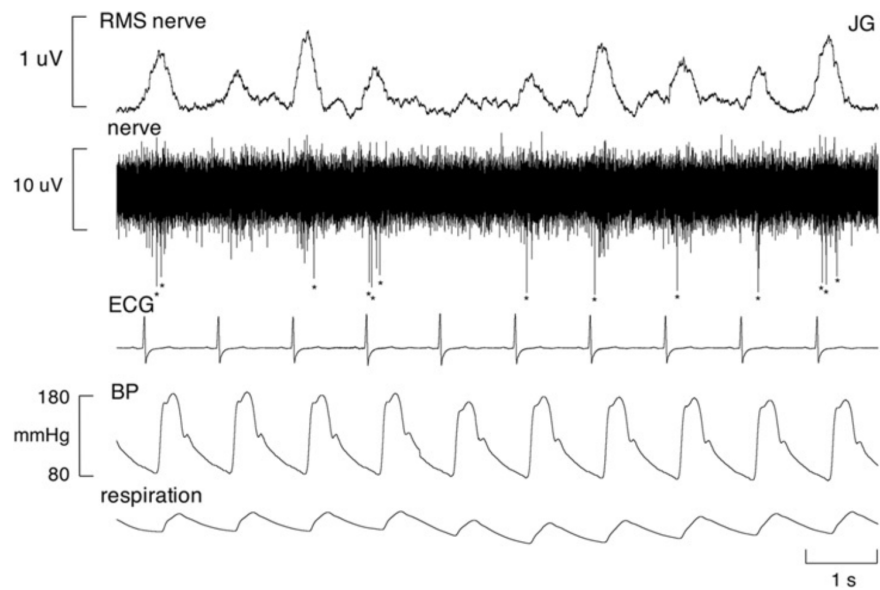


Figure 1.14: Recording from a muscle vasoconstrictor neuron in an awake patient. Typical of muscle vasoconstrictor neurons, this unit generally fired only one spike (indicated by asterisks) per cardiac interval, but occasionally fired multiple spikes within a burst of MSNA (Image by:[25])

The majority of the delay is due to slow conduction in the peripheral sympathetic fiber, while at least 0.25 s is related to central conduction and processing time in the brainstem and spinal cord [33].

Spikes per cardiac interval

Because each type of neuron has a degree of cardiac rhythmicity, the cardiac interval (the duration between two consecutive R-waves) may be used to divide a recording into epochs and determine whether the nervous system fires or remains dormant.

The proportion of cardiac intervals in which a neuron fires one or more spikes is referred to as the *firing probability* (presented as a percentage), and is the unitary equivalent of burst incidence (burst probability), namely the percentage of cardiac intervals in which multi-unit sympathetic bursts occur.

The amount of spikes produced by vasoconstrictor motoneurones differed between units and bursts.

The occurrence of spikes was not high. Many previous researches indicate that an average of 75% of all heart beats lacked spikes altogether.

- An average of
- 20% of cardiac intervals show 1 spike,
 - 5 % of cardiac intervals show 2 spike,
 - 1 % of cardiac intervals show 3 spike,
 - 0.5% of cardiac intervals show 4 spike [35, 34, 36, 37, 38, 39].

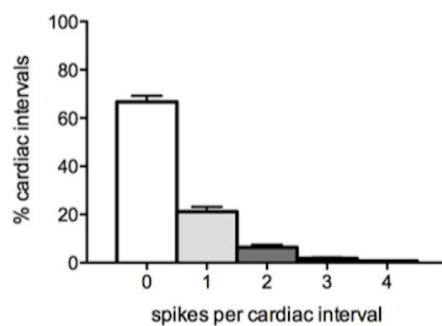


Figure 1.15: Spike distribution of muscle vasoconstrictor neurons
(Image by:[34])

1.3.2 Respiration

The breathing act takes part in the function of controlling blood flow.

During the normal respiratory cycle the sympathetic and parasympathetic efferents are active in counter-phase [40]:

- During inspiration, the alveoli expand, the left atrial pressure drops, and the pulmonary microcirculation becomes more compliant. Consequently, left ventricular output and blood pressure fall, resulting in a baroreflex-mediated increase in HR.

- During expiration, the opposite happens: left ventricular output rises, blood pressure rises, and HR falls due to the baroreflex and the influence of respiratory centers.

Breath modulation of sympathetic nerve activity

Microneurographic recordings of MSNA and non-invasive, beat-by-beat assessments of regional blood flow have revealed evidence for a major respiratory system influence on sympathetic vasoconstrictor outflow in healthy humans.

In healthy humans, multiple types of respiratory influences on MSNA have been reported, including within-breath modulatory effects, lung inflation inhibitory effects, muscle metaboreceptor influences [41].

Respiratory modulation of MSNA is quite evident [42, 43, 17, 44, 45], at least across the usual range of resting breathing frequencies.

The respiratory rhythm consists of 3 distinct phases, inspiration, postinspiration, i.e. stage I expiration, and stage II expiration.

The sympathetic nerve activity usually displayed a ramp-like increase during inspiration, followed by a decrescendo of activity during postinspiration (stage I expiration), and finally a period of silence during stage II expiration [46, 47].

Small variations in systemic blood pressure and changes in lung capacity might be potential mediators of MSNA alterations during breathing, with no apparent influence from central respiratory motor output.

Human experiments reveal that the SNS's sensitivity to baroreceptor stimuli varies during breathing, with the greatest reactivity occurring at low lung volumes, when spontaneous MSNA is highest [48, 42].

This experimental evidence is in line with evidence of strong associations between within-breath modulation of MSNA and changes in diastolic blood pressure at any given lung volume or changes in lung volume at any given diastolic blood pressure[45].

Cardio-Sympatho-Respiratory Coupling

Cardiac, sympathetic and respiratory activities are coordinated for effective and efficient gas exchange[49]. It is possible to observe that heartbeat, blood pressure, and ventilation share common frequencies[50] .

The cardiovascular and respiratory systems can be considered as just a single physiological system that delivers oxygen to the tissues while also eliminating carbon dioxide from the body.

The neural control of this system is located within the brainstem, which is also where respiratory rhythm and sympathetic premotor activity are generated.

Furthermore, within the brainstem, the respiratory and sympathetic control circuits interact, and various sensory afferents, such as baroreceptor inputs, influence the neurons that generate and modulate both respiratory and sympathetic activities [51].

Even after vagotomy and decerebration, sympathetic nerve activity reflects respiratory modulation, supporting the hypothesis of central connection between respiratory and sympathetic networks [52, 53] .

This coupling appears to be the main mechanism for optimizing minute ventilation and cardiac output to improve oxygen uptake/perfusion efficiency at rest, as well as allowing appropriate dynamic integrative cardiovascular and respiratory reflex responses, which are necessary for maintaining homeostasis[49, 54].

Therefore, respiratory modulation may contribute to the dynamic control of SNA.

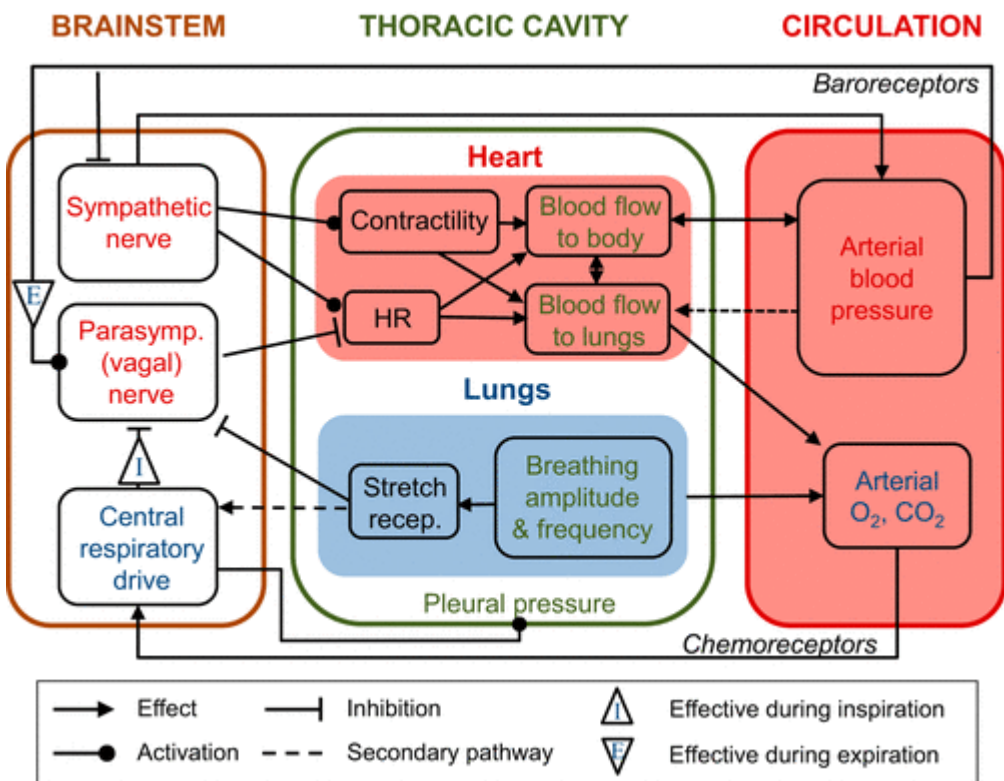


Figure 1.16: Cardiorespiratory interactions main mechanisms. The brain stem is responsible for central respiratory drive, as well as sympathetic and parasympathetic nerve activity. The heart rate is mostly controlled by the parasympathetic nerves (HR). HR, contractility, and blood pressure are all regulated by sympathetic nerves (via the peripheral resistance, not shown in the diagram). Stroke volume and thus blood flow to the body and lungs are directly influenced by the product of HR and contractility (these are also affected by pleural pressure). The partial pressures of O₂ and CO₂ are determined by pulmonary blood flow and breathing, whereas arterial blood pressure is determined by systemic blood flow (together with peripheral resistance). Parasympathetic nerves are activated and sympathetic nerves are inhibited when arterial blood pressure rises. The central respiratory drive regulates parasympathetic nerve activity. Changes in pleural pressure affect the central respiratory network, which regulates inspiration and influences breathing amplitude and frequency. Breathing affects the activity of pulmonary stretch receptors, which feeds back to the parasympathetic nerve. The central respiratory drive is influenced by arterial CO₂ and O₂ via peripheral and central chemoreceptors. (Image by:[51])

1.3.3 Photoplethysmogram (PPG)

Photoplethysmography is a non-invasive technique used to determine relative blood volume changes in blood vessels close the skin's surface.

It has grown in popularity as a non-invasive approach for measuring mean arterial blood pressure and oxygen saturation in recent years (Pulse Oximeter).

The fact that blood absorbs infrared light several times more strongly than the other skin tissues allows PPG to assess blood volumetric changes in skin perfusion.

PPG offers a number of benefits. It makes use of basic, low-cost optical sensors that require minimum maintenance.

The simplest PPG sensor consists of an infrared LED and a photo detector placed in a small plastic housing.

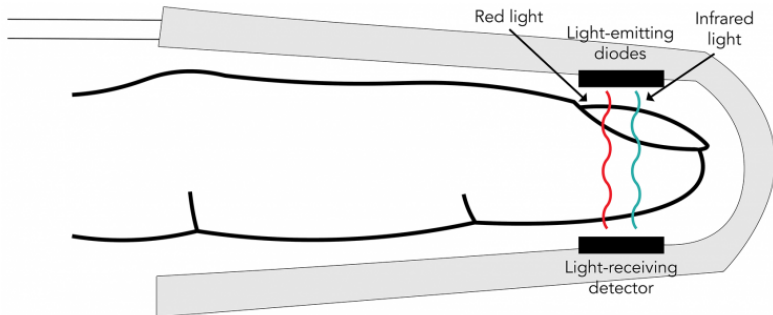


Figure 1.17: A standard pulse oximeter operating model that uses an electronic processor and a pair of small light-emitting diodes (LEDs) facing a photodiode through a translucent part of the patient's body, usually a fingertip or an earlobe. One LED is red, with wavelength of 660 nm, and the other is infrared with a wavelength of 940 nm. Light absorption at these wavelengths vary dramatically between blood that is oxygenated and blood that is not. (Adapted from: [55])

The PPG-signal obtained from conventional pulse-oximeters identifies changes in blood volume in the microvascular bed of tissue.

A pulsatile physiological waveform (*pulse wave*) related to heart synchronous changes is overlaid on a more slowly fluctuating baseline with numerous lower frequency components related to breathing, SNS activity, and thermoregulation in the PPG-signal.

Drops in pulse wave amplitude (PWA), as measured by PPG at each cardiac cycle, are known to directly reflect changes in peripheral blood flow caused by vasoconstriction, and hence may provide a very simple indication of autonomic activity. Heart rate and BP are modulated neurally, and both parasympathetic and sympathetic nerves have respiratory-modulated activity patterns [6].

1.4 Purpose of the study

Numerous research have been conducted on the state of activation of the CNS in the last 50 years, aided by the discovery of microneurography. Because it entails the use of tungsten needles placed in the nerve, as previously explained, this approach proves to be intrusive and time-consuming, so cannot be applied routinely for clinical diagnostic purpose.

Clinical research has showed the multiple degrees of interaction of the autonomic system, and has underlined the relevance of assessing the sympathetic activity of the muscular nerve (MSNA), despite its difficulty.

The ANS is the part of the nervous system that regulates the body's visceral functions. It's a kind of effector system that control smooth muscle, cardiac muscle, and glandular activity. In various situations, it uses the endocrine system to tune cardiac output and arterial pressure, stomach and intestinal activities, glandular secretions, and a variety of other visceral processes. The SNS manage several homeostatic activities in living beings. SNS fibers innervate practically every organ system, allowing them to control activities as diverse as pupil diameter, gut motility, and urine system.

Using standard multiunit recordings, elevated levels of muscular sympathetic nerve activity have been discovered in a variety of disorders. MSNA is increased in many different forms of hypertension, along with congestive heart failure [56, 57], obstructive sleep apnea[58, 59, 60], chronic obstructive pulmonary disease [61, 44], and bronchiectasis [44].

Heart failure, for example, is associated with increased sympathetic nerve activity (HF). Most blood vessels, including those in the skin, the digestive tract, and the kidneys, constrict when the SNS is stimulated. Baroreceptors are mechanosen-sitive afferent nerve endings found largely in the carotid sinus and aortic arch, as well as in the pulmonary great arteries, atria, and ventricles, that detect changes in blood pressure. The dynamic inverse link between sympathetic nerve activity and arterial blood pressure is due to the arterial baroreflex [29].

A substantial sympathoexcitation is seen in the neurohumoral activity associated with congestive heart failure (CHF), which is thought to be an essential pathophysiology and prognostic component.

Excessive sympathetic nerve activity has been linked to a bad prognosis since the early stages of the disease. Excessive sympathetic activity in chronic HF has detrimental consequences on the heart, including beta receptor downregulation [62], cardiac myocyte apoptosis [63], and calcium overload [63, 64].

It is crucial to emphasize, however, that a high level of MSNA does not always reflect the presence of underlying disease.

Individual muscle vasoconstrictor neurons in healthy adults with increased resting levels of MSNA exhibit low firing probabilities, low firing rates, and a low incidence of multiple firing [65]. Pathological increases in MSNA are linked to high firing probabilities, high firing rates, and a high incidence of multiple firing of individual neurons. In addition, the patterns of growth vary depending on the kind of disease.

In light of these considerations, this thesis study examined a dataset in which the MSNA signal of 9 healthy individuals was collected alongside other non-invasive peripheral biosignals such as blood pressure, electrocardiographic signal (ECG), photoplethysmographic signal (PPG), and respiration rate. Guided voluntary breathing movements, which are known to promote MSNA activity, were used to induce both the stationary (baseline) and non-stationary (maneuvers) conditions.

The project's ultimate purpose is to create techniques that can characterize possible links between MSNA and non-invasive peripheral signals in a systematic way. An algorithm is required that allows for the measurement or prediction of MSNA activity without the need of invasive methods such as microneurography. These tools could in fact be useful in diagnostics if they are quick and easy to use.

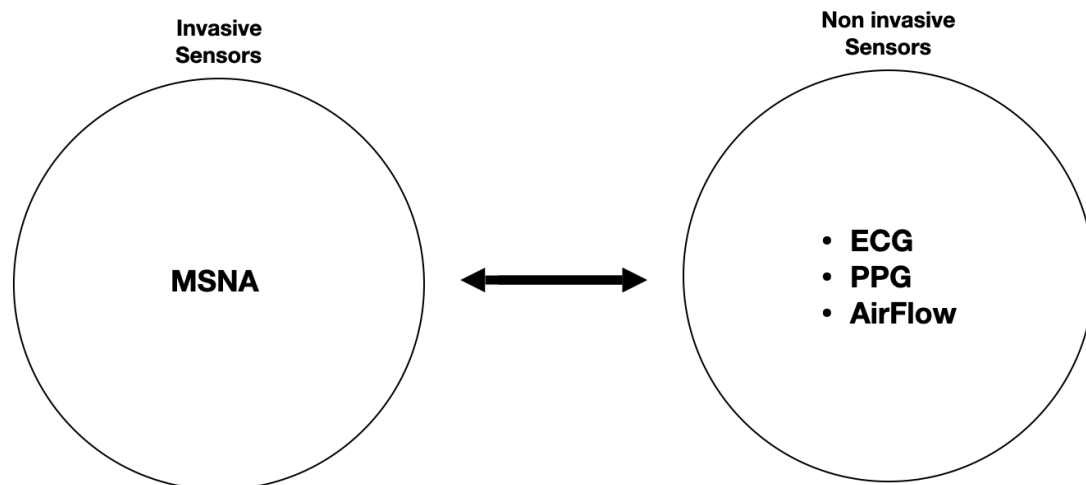


Figure 1.18: Concept schematic of the interaction model through invasive and non-invasive sensors

Currently, collecting MSNA data on a broad scale is very challenging, and even more difficult during sleep, posing a significant barrier to study in the field.

Therefore, throughout the process of this research, a toolbox was created in the Matlab environment that can do an automatic analysis of all of the above-mentioned signals.

The signals were cleaned from noise and recording artifacts before being processed with the aim of extrapolating a wide set of parameters that were selected after a comprehensive analysis of the literature.

All data and functionalities inside the database have been appropriately structured to enable for quick access for further analyses.

The raw MSNA signal received the most attention, and an automated approach was developed to minimize noise before estimating the mean neurogram for each cardiac cycle, as well as identifying and categorizing bursts of pulses in the MSNA.

The validity of the MSNA-based features was then examined by comparing the values to those reported in prior research in which specialists visually analyzed individual bursts of MSNA.

Finally, within the toolbox, a module has been included that evaluates the temporal relationships between MSNA events and cardiac and respiratory events, as well as inspects consistent variations in the characteristics of MSNA features that are time-bound to peripheral events.

Variations in the pulse wave amplitude (PWA) signal, as assessed by finger photoplethysmography (PPG), which are reported to indicate peripheral vasoconstriction, were examined in particular.

Chapter 2

Materials and methods

2.1 Data acquisition

2.1.1 Participants

Nine healthy participants (36 ± 9 years, 5 male, 5 female, BMI 25 ± 2 kg/m 2) were selected from January 1st to July 1st, 2020. All participants provided written informed consent to participate in the study and were subjected to a full physical examination as well as an examination of anamnestic data to guarantee the absence of any past disorders that might alter MSNA.

2.1.2 Data Acquisition

Recording of Sympathetic activity

The participant was positioned in a semi-recumbent position on a chair reclined at 45 degrees, with the legs resting on a horizontal plane. In order to determine the course of the right common peroneal nerve at the level of the fibular head, electrical pulses (2-10 mA; Stimulus Isolator, ADInstruments) were administered via a 2 mm surface probe. Weak electrical stimulation was utilized to guide manipulation of the active sterile insulated tungsten microelectrode's tip into the nerve (0.2 ms, 1 Hz, 0.01-1.0 mA). Induced muscle twitches at 0.01-0.02 mA, without radiating paraesthesia, confirmed that the tip had penetrated a muscular fascicle of the nerve. A reference electrode with a bigger uninsulated tip was implanted 1 cm away. The activity of neurons is detected using a headstage (NeuroAmpEX, ADInstruments). The signal is then amplified through an isolated amplifier (gain 2x104, bandpass 0.3-5.0 kHz) and recorded on hard drive at a sampling frequency of 10kHz. The identification of the muscle fascicle of the nerve was established by spontaneous or stretch-evoked activity of muscle spindle afferents in the absence

of afferent activity caused by light stroking of the leg or foot. Electrode location was improved by observing the mean voltage neurogram of the filtered nerve signal until spontaneous bursts of muscular sympathetic nerve activity (MSNA) with evident cardiac rhythmicity were noticed, particularly during a maximal inspiratory apnoea.

Recording of non-invasive physiological signals

Electrocardiographic activity (ECG) was recorded with Ag-AgCl surface electrodes (BioAmp, PowerLab, ADInstruments, Sydney, Australia) on the chest and sampled at 2 kHz (bandpass 0.3 Hz1 kHz).

Finger pulse plethysmography (PPG) was used to record continuous blood pressure, which was sampled at 400 Hz (DC-200 Hz) and calibrated with an integrated sphygmomanometer cuff on the opposite upper arm (NOVA; Finapres Medical System BV, Amsterdam, Netherlands).

A respiratory belt transducer was used to capture respiration at 100 Hz (DC-100 Hz) (ADInstruments).

All signals has been simultaneously acquired and displayed in real time via Lab Chart Software. A data acquisition and analysis system was used to store all physiological signals on a computer (PowerLab 16SPTM hardware device and LabChartTM, ADInstruments).

2.1.3 Experimental Procedures

Simultaneous recording of MSNA and non-invasive peripheral bio-signals was performed during periods of normal breathing as well as during specific voluntary breathing maneuvers, which have been shown to affect sympathetic nerve activity in prior research [41, 61, 66, 67, 68]. Both conditions were separately investigated during the study, in order to assess and compare potential relationship between MSNA and physiological signals separately also during non-steady-state. In particular, subjects were asked to simulate two different patterns of Periodic Breathing (PB), namely a cyclical breathing pattern composed of alternating periods of hyperventilation (hyperpnea) and temporary cessation of respiratory effort (central apnea). Periodic Breathing is a breathing pattern of clinical relevance since it is frequently experienced by patients affected by heart failure (HF), in which central apneas alternate with hyperpneas with a typical crescendo-decrescendo pattern known as Cheyne-Stokes Respiration (CSR). CSR is caused by respiratory control system instability characterized by a tendency to hyperventilate [67].

Each experimental session started once the microelectrode was correctly positioned and MSNA signal was stable. After a baseline session, lasting from 5 to 10

minutes, in which participants were free to breath naturally, each participant was then given explicit instructions on how to perform different breathing manoeuvres. Specifically, a computer monitor was used in order to display specific ventilatory patterns that subjects were asked to follow in real time. Before the recording, participants had the possibility to practice with the visual feedback and simulate several breathing patterns. Each subject performed three different breathing manoeuvres in a randomized order, lasting 3 minutes each. Different manoeuvres were separated by periods of spontaneous breathing until heart rate and blood pressure had returned to baseline. Such manoeuvres included a prolonged hyperventilation period, in which subjects were advised to hyperventilate (i.e. breath as fast and as deep as possible) and two different patterns of Periodic Breathing, defined as follow in order to standardize the CSR cycle among subject:

- i) Periodic Breathing with short cycle length (40 sec), namely the alternation between a 20 seconds long hyperventilation phase and 20 sec apnea phase;
- ii) Periodic Breathing with long cycle length (60 sec), namely the alternation between a 40 seconds long hyperventilation phase and 20 sec apnea phase;

2.2 Processing pipeline

The processing pipeline is made up of two main phases:

- a pre-processing phase in which each sensor's raw signal is analyzed apart. The noise is reduced and distinctive features of the signal are estimated.
- an analysis phase in which the aim was to create a series of algorithms that could systematically characterize potential relationships between MSNA and peripheral non-invasive signals.

The working environment adopted for the entire project is MATLAB by MathWorks which constitutes a numerical calculation and statistical analysis software.

2.3 Pre-processing

With the implementation of a python script reparable at https://github.com/JimHokanson/adinstruments_sdk_matlab, each original file with the extension *.adicht*, property of AD Instruments SDK, has been converted in *.mat* file to be available in the Matlab environment.

After the acquisition and conversion to *.mat* format the recordings were pre-processed and analysed in the software Matlab (The MathWorks, Inc.).

First of all, the recordings imported were re-organized. The data logging software, Labchart, exports the data by splitting each patient acquisition into partial log clusters containing all sensors data.

We chose to arrange the dataset into struct-type containers for each patient, which contained the entire interpolated acquisition for each sensor as well as related meta data like comments, sampling frequency, unit of measure, time of acquisition.

2.3.1 Nerve Signal

Noise

The signal derived from the acquisition of microneurography of the peroneal nerve is characterized by the presence of various types of noise.

The following sources must be considered to extract and reduce the noisy component from the signal:

a) AC power-line:

Due to the high impedance electrodes the input terminals of the headstage will act as antennae that pick up electrical noise.

The greatest sources of noise, the line frequency of the power supply, 50 or 60 Hz, sit within the laboratory (i.e. the data acquisition and monitoring equipment), as do the sources of higher frequency components, such as computer monitors and fluorescent lights.

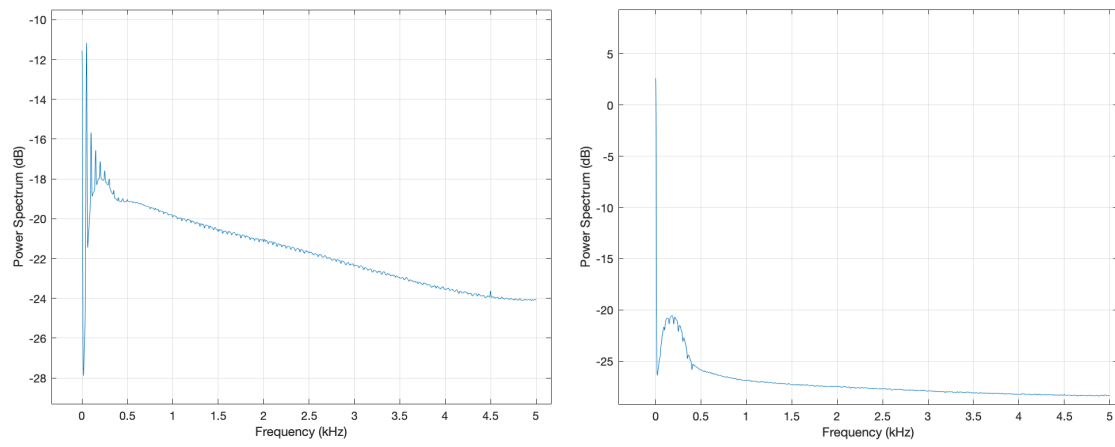
A notch type filter has been implemented to reduce power supply noise, with cut-off frequencies set around 50Hz and the following 8 harmonics.

The filter was created using the 'designfilt' function in Matlab. It consists of a second-order ('FilterOrder',2) Butterworth ('DesignMethod','butter') infinite impulse response (IIR) bandstop filter (*bandstopiir*).

```

1 linenoise_f = [ 50 100 150 200 250 300 350 400 ]
2 designfilt(      'bandstopiir',
3                 'FilterOrder', 2,
4                 'HalfPowerFrequency1', linenoise_f(k-1),
5                 'HalfPowerFrequency2', linenoise_f(k+1),
6                 'DesignMethod', 'butter',
7                 'SampleRate', fs );

```



(a) Power spectrum of the raw signal (b) Power spectrum of the filtered signal

Figure 2.1: Power spectrum of nerve signal

b) Needle Drift:

As long as the nerve is quite deep the microelectrode is well supported by the tissue overlying and remain stable.

However, when the nerve is superficial, the microelectrode may likely to slip out due to gravity, particularly if oriented upwards towards the nerve. Doing so the mean-voltage neurogram will show a downward shift in the baseline, which may be gradual or abrupt.

To compensate this attenuation a '*detrend*' algorithm has been applied to the previously filtered signal to remove the polynomial trend. The filter acts removing from the data the best straight-fit line comparable with the constant drift of the electrode.

c) Electrode noise:

Modern amplifiers feature a high input impedance, which ensures that the voltage taken up by the recording (active) microelectrode is kept as high as possible without current leakage into the amplifier.

Because the input and electrode impedances are both high, everything between the tip of the micro-electrode (the recording surface devoid of insulation) and the input terminals of the headstage, the connecting wires, will behave as antennae, picking up electrical noise.

An attempt was then made to estimate the level of this noise that was here defined as the variance of MSNA peaks with amplitude closer to the MSNA median value than three scaled median absolute deviations (MAD). Both MSNA median and MAD were evaluated for each data point on a 10 second long sliding window. This is achieved applying a Hampel filter to the local maxima points calculated on the signal and finally calculate its variance.

In fact, the presence of spontaneous burst activity of spikes (action potentials) separated by silent priods against a background of considerable gaussian noise is a general characteristic of the MSNA signal.

```

1 [y_pk~,~,~,p_pk~] = findpeaks( filteredSignal );
2 [~,ind_out] = rmoutliers(p_pk~, 'movmedian', 10*fs);

```

The resulted noise is then subtracted from the previously filtered signal.

```

1 noise = var(p_pk~(ind_out));
2 filteredSignal(filteredSignal >0) =
3     filteredSignal(filteredSignal >0) - noise/2;
4 filteredSignal(filteredSignal <0) =
5     filteredSignal(filteredSignal <0) + noise/2;

```

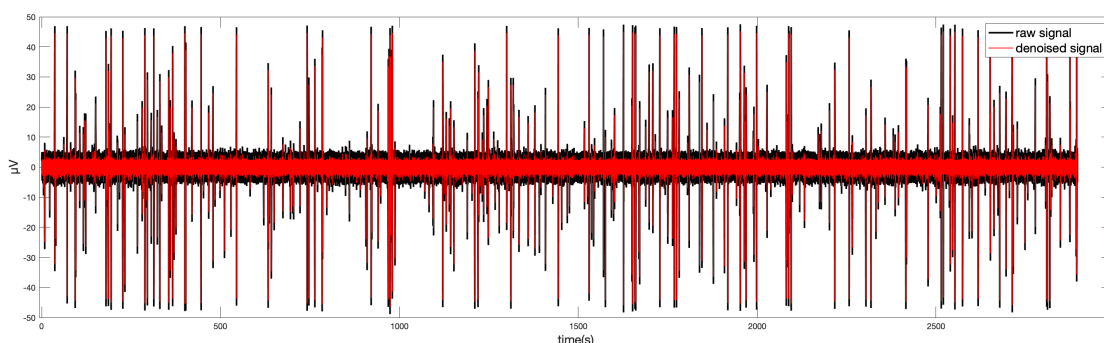


Figure 2.2: Electrode signal detection

d) RMS:

To facilitate the identification of the bursts, the filtered neural signal is also full-wave rectified, produced as an RMS-processed (root mean square) moving average with a time constant 200 ms. This procedure is currently the most widely accepted by the scientific community [25, 12] and shows the advantage of avoiding the integration time lag.

$$RMS(t) = \sum_{j=t}^{t+200ms} \sqrt{filteredSignal(t+j)^2} \quad (2.1)$$

```
1 RMS      = sqrt( movmean( filteredSignal.^2, 0.2*fs ) );
```

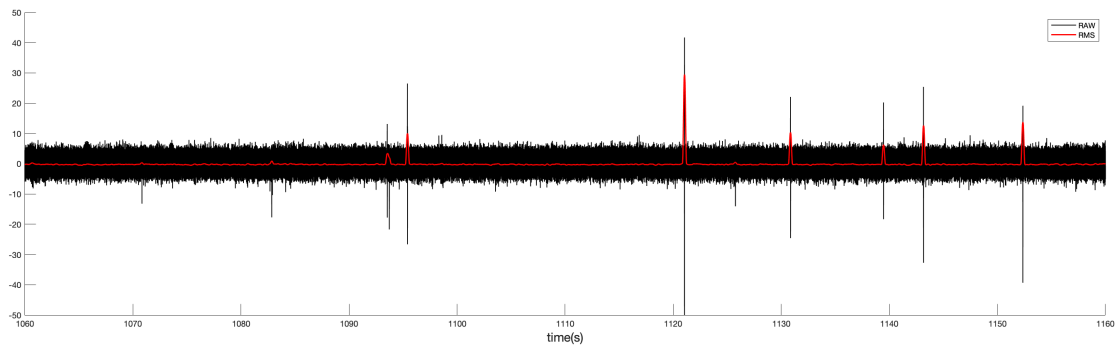


Figure 2.3: RMS signal

e) Subject movements:

Lastly, the unintentional movement of the patient during the recording is taken into account.

To minimize their impact a detrend filter and then a linear regression ('*lowess*') smoothing algorithm (*smoothdata*) with windows of 200 ms ($0.20*fs$), have been applied to the RMS signal.

```
1 RMS_filtered = detrend( RMS );
2 RMS_filtered = smoothdata( RMS_filtered, 'lowess', 0.20*fs );
```

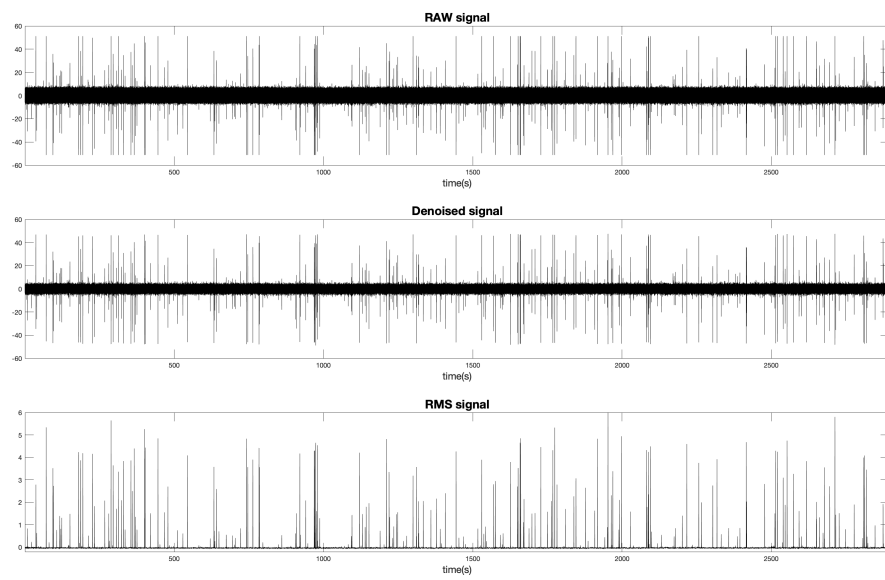


Figure 2.4: De-Noising Process

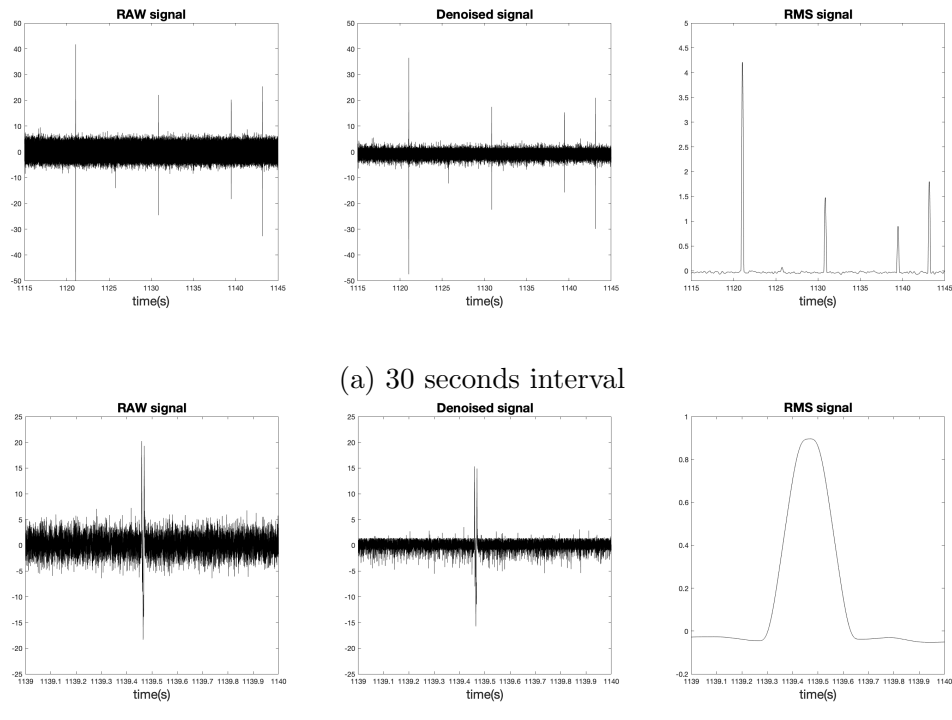


Figure 2.5: Zoomed De-Noising Process

Burst detection

As previously discussed in *Chapter 3*, sympathetic outflow occurs not as a continuous (tonic) discharge but as bursts of impulses.

Because unmyelinated postganglionic axons prefer to cluster inside a fascicle [69], a typical recording is made up of action potentials produced by a large number of axons.

Parallel to most burst detection software, a peak finding technique was adopted to identify the presence of bursts in the RMS nerve trace. Instead of apply threshold parameters to the peak finding algorithm, we implemented an algorithm for the detection of the outliers based on a moving median calculation method over a time window of 10 seconds.

Outlier bursts are therefore the only ones to be maintained, as opposed to background noise, which produces smaller and high frequency peaks.

```
1 [ y_pk , x_pk , w_pk , p_pk ] = findpeaks( RMS_filtered ) ;
2
3 [ ~ , ind_out ] = rmoutliers( p_pk , 'movmedian' , 10* fs ) ;
4 x_pk = x_pk(ind_out) ;
5 y_pk = y_pk(ind_out) ;
6 w_pk = w_pk(ind_out) ;
7 p_pk = p_pk(ind_out) ;
```

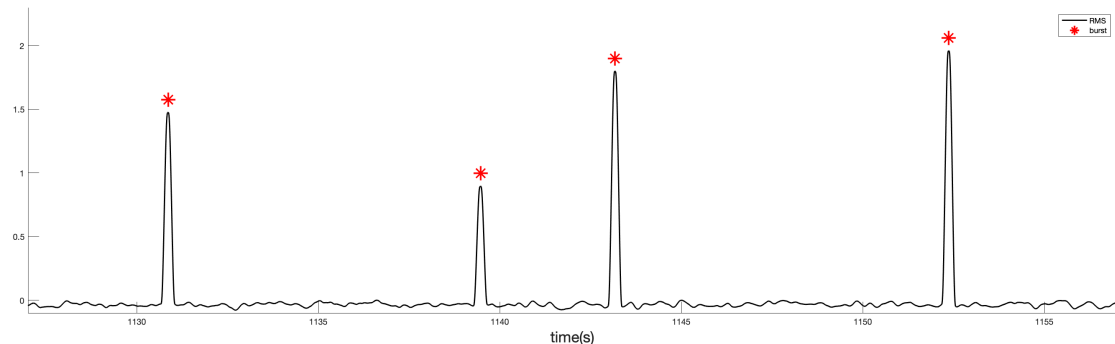


Figure 2.6: MSNA Burst

Burst feature evaluation

The standard approach to recording MSNA bursts has been and continues to be very useful, but there is a lot of information in sympathetic burst patterning that hasn't been extracted from multiunit recordings.

Because of the pulse synchronicity of MSNA, the most accepted method to quantify MSNA is calculation of burst rate over the recorded time period, which is expressed as bursts per minute (burst frequency) and bursts per 100 heart beats (burst incidence) [22, 23, 24, 70, 12, 25, 27, 11, 13].

$$\text{burstFrequency} = \frac{\text{number of burst}}{60 \text{ sec}}$$

$$\text{burstIncidence} = \frac{\text{number of burst}}{100 \text{ HeartBeats}}$$

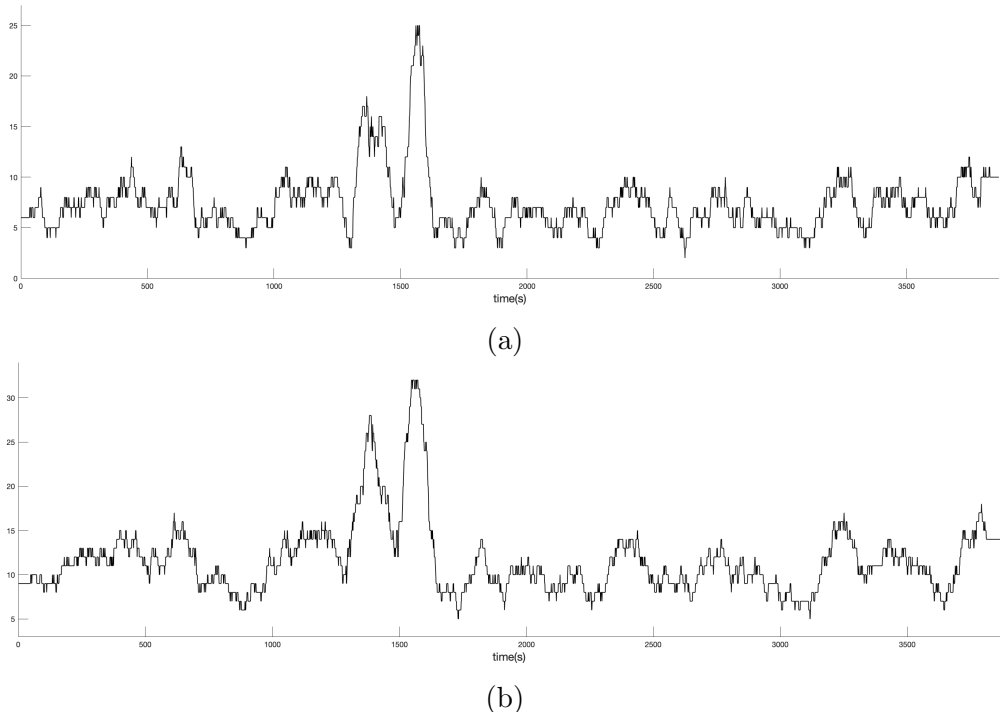


Figure 2.7: Burst (a) frequency and (b) incidence

Further information that can be extracted from the neurogram that can help quantify sympathetic activity is the quantification of area and amplitude of the burst.

However, burst area and amplitude are determined not just by the intensity of a sympathetic burst, but are also dependent on the proximity of the electrode tip to the group of active axons from which the recording is made. For this reason, one cannot compare burst amplitudes across subjects, unless they are first normalized.

[44, 71, 72, 73].

The area has been determined calculating the approximate integral of the nerve signal during the burst via the trapezoidal method. To make sure the burst area is standardized feature across all subjects, it was chosen to normalize all burst area in each subject recording with the highest burst observed the same recording.

$$burstArea \approx \frac{\int_{burst} RMS(t) * dt}{max(RMS(burst))}$$

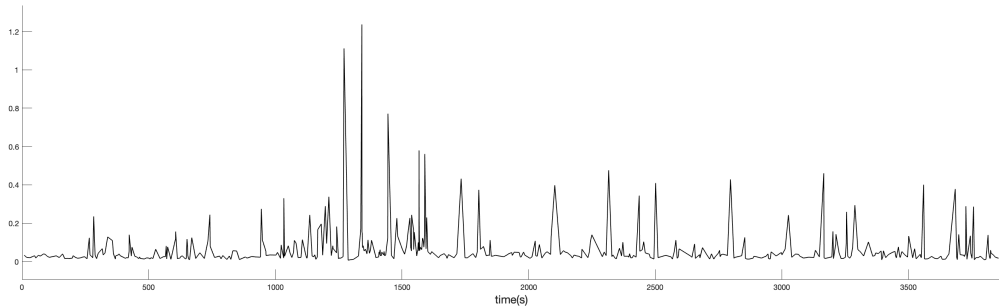


Figure 2.8: Burst area

2.3.2 ECG Signal

The main source of noise in the ECG signal is the line frequency of the power supply. To remove the 50Hz frequency typical of the mains frequency utilized in the sampling laboratory, a low pass filter was applied.

The filtering has been realized performing a zero-phase lowpass ('low') Butterworth(*butter*) digital filter (*filtfilt*) with a cut-off frequency $fc=50Hz$:

```
1 [A,B] = butter(5, fc/(fs/2), 'low');
2 ecgff = filtfilt(A,B, ecg);
```

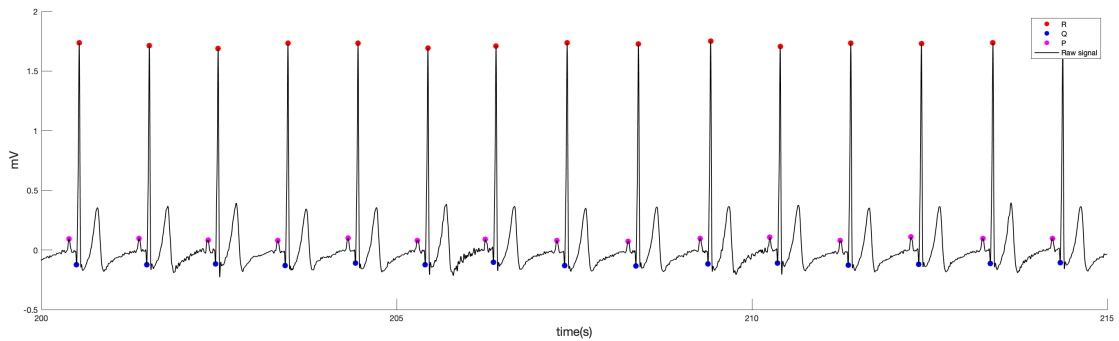
The electrocardiogram's distinctive features (PQR wave) were then extracted using a peak finding algorithm for each point with different threshold values applied.

The following script detects R points :

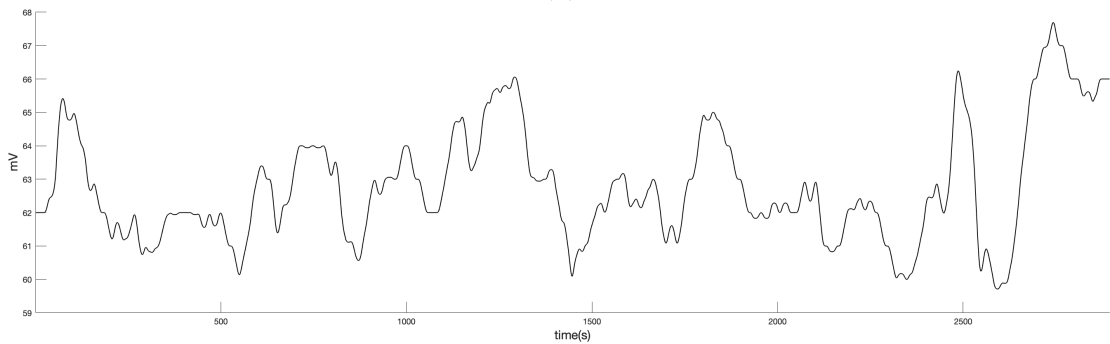
```
1 [y_R, x_R, w_R, p_R] = findpeaks(ecgSignal);
2
3 minDist =
4 [ mean(x_R(2:end)-x_R(1:end-1)) - mean(x_R(2:end)-x_R(1:end-1)) ]/3;
5
6 minHeight = max(y_R) - (max(y_R)/1.5);
7
8 [y_R, x_R, w_R, p_R] = findpeaks(
9     ecgSignal,
10     'MinPeakDistance', minDist,
11     'MinPeakHeight', minHeight,
12     'MinPeakProminence', 0.01
13 );
```

The Beats Per Minute are then calculated counting the number of R peaks in a moving window of 60 seconds. The variable BPM is a two row matrix: the first row is

```
1 start = find(x_R > (31*fs), 1);
2 stop = find(x_R <= (x_R(end) - 30*fs), 1, 'last');
3 for k = start:stop
4     tmpStart = find(x_R >= (x_R(k) - 30*fs));
5     tmpStop = find(x_R >= (x_R(k) + 30*fs));
6     BPM(2,k) = length(x_R(tmpStart:tmpStop));
7     BPM(1,k) = x_R(k);
8 end
9 for k=1:start
10     BPM(1,k) = x_R(k);           BPM(2,k) = BPM(2, start);
11 end
12 for k=stop:length(x_R)
13     BPM(1,k) = x_R(k);           BPM(2,k) = BPM(2, stop);
14 end
15 BPM(1,:) = BPM(1,:)./ fs;
```



(a)



(b)

Figure 2.9: The figure shows in (a) a 15 seconds of ECG trace marked with the PQR wave and in (b) the BeatsPerMinute signal calculated on the entire recording

This procedure for the detection of R peaks has been validated both towards a visual scoring and with respect to other algorithms already commonly used. The results are provided numerically in the *Results* chapter that follows.

2.3.3 Respiration Signal

The noise in the signal under consideration is attributed to the subject's movements, which appear as artifacts in the form of spikes with amplitude much higher than the average. To minimize the noise we searched for outlier spikes with amplitude five times greater than the mean of the signal.

Inspiration / Espiration phase detection

The signal filtered from artifacts is then smoothed and detrended in preision to be fed to a peak finding algorithm.

```
1 %filter artifacts
2 resp( find( abs(resp)>mean(abs(resp)) *5 ) ) = mean(resp);
3
4 %filter subject movements and sensor drifting
5 resp_filt = smoothdata(resp, 'lowess', 1, 'SamplePoints', time);
6 resp_filt = detrend(resp_filt);

1 [y_pk, x_pk, w_pk, p_pk] = findpeaks( abs(resp_filt), fs );
2 minPeakProminence = mean(p_pk) /2 ;
3 minPeakHeight = mean(y_pk) /2 ;
4 % search for Pos and Neg Peaks
5 [y_pk, x_pk, w_pk, p_pk] = findpeaks(
6     abs(resp_filt), fs,
7     'MinPeakProminence', minPeakProminence,
8     'MinPeakHeight', minPeakHeight );
9 % search only Pos Peaks
10 [y_pkPos, x_pkPos, w_pkPos, p_pkPos] = findpeaks(
11     resp_filt, fs,
12     'MinPeakProminence', minPeakProminence );
13 % search only Neg Peaks
14 tmp = resp_filt;
15 tmp( find( resp_filt >= 0 ) ) = 0;
16 tmp = abs(tmp);
17 [y_pkNeg, x_pkNeg] = findpeaks(
18     tmp,
19     fs,
20     'MinPeakProminence', minPeakProminence,
21     'MinPeakHeight', minPeakHeight );
22
23
24 y_pkNeg = -y_pkNeg;
25 for k=1:length(x_pkNeg)
26     y_pk( find( x_pkNeg(k) == x_pk ) ) = -y_pk( find( x_pkNeg(k) == x_pk ) );
27 end
```

The peaks derived describe the limits of the inspiration and expiration phases.

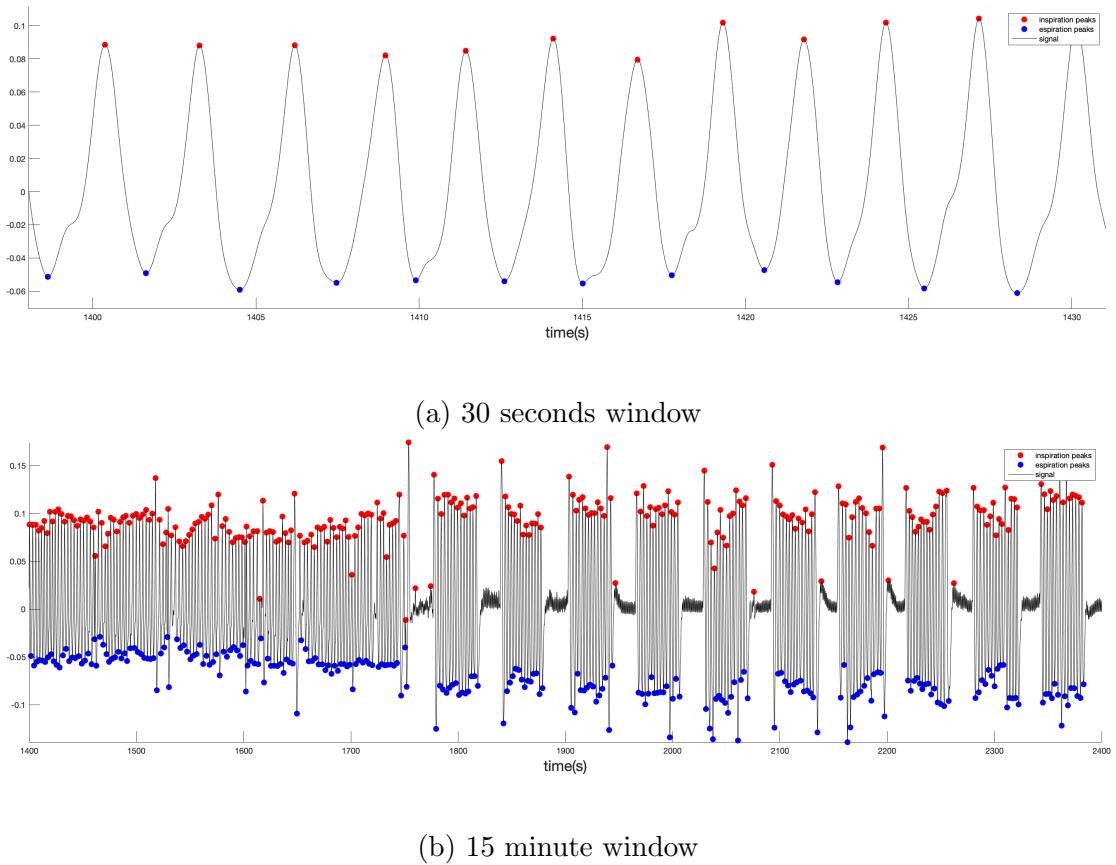


Figure 2.10: Inspiration and expiration phases detection

The RPM (Respiration Per Minute) value was calculated for each subject's recording by quantifying the inspiratory or expiratory peaks on 60 second intervals.

```

1 RPM = [];
2 start = find(x_pkPos > 31, 1);
3 stop = find(x_pkPos <= (x_pkPos(end)) - 30), 1, 'last');
4
5 for k=start:stop
6     tmpStart = find( x_pkPos >= x_pkPos(k) - 30 );
7     tmpStop = find( x_pkPos >= x_pkPos(k) + 30 );
8     RPM(2,k) = length( x_pkPos(tmpStart:tmpStop) );
9     RPM(1,k) = x_pkPos(k);
10 end
11
12 for k=1:start % correct first 30 sec
13     RPM(1,k) = x_pkPos(k);
14     RPM(2,k) = RPM(2, start);
15 end
16
17 for k=stop:length(x_pkPos) % correct last 30 sec
18     RPM(1,k) = x_pkPos(k);
19     RPM(2,k) = RPM(2, stop);
20 end

```

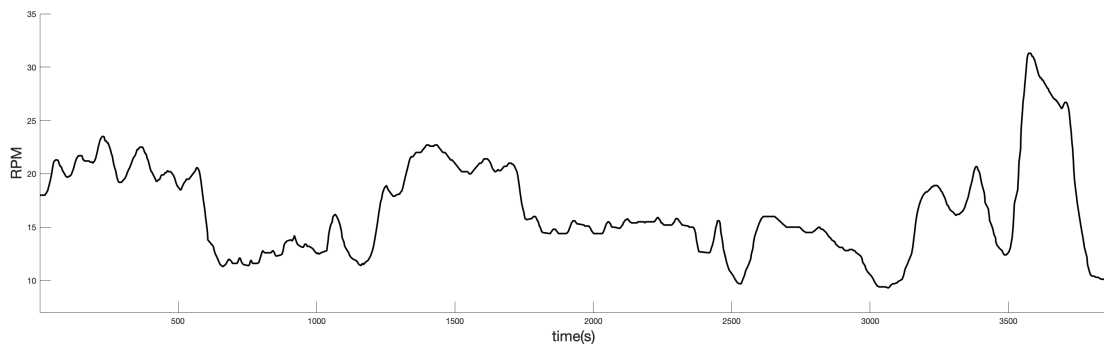


Figure 2.11: Respiration Per Minute (RPM)

Apnea / Hyperventilation phases detection

During data collection, respiratory techniques that have been proven to impact the MSNA in past studies were used to better understand sympathetic activity [40, 41, 42, 43, 17, 44, 45, 51].

As a result, an algorithm for the automatic detection of these respiratory maneuvers was necessary, as well as a time delimiter, so it could be used later in the analysis phase. The first step of the procedure is devoted to the identification of apneas phases throughout the entire data track

It's worth noting that abrupt changes in breathing patterns result in points with zero second derivative in the respiratory signal's time domain.

```

1 apneaFunc = diff( movsum( diff(x_pk), 5) );
2
3 [ apneaPk(2,:) , apneaPk(1,:)] =
4     findpeaks( abs(apneaFunc) , 'MinPeakHeight' ,10);
5
6 [ PosApnea(2,:) , PosApnea(1,:)] =
7     findpeaks( apneaFunc , 'MinPeakHeight' ,10);
8
9
10 for k=1:length(apneaPk(2,:))
11     if isempty( find( apneaPk(2,k) == PosApnea(2,:) ) )
12         apneaPk(2,k) = - apneaPk(2,k);
13     end
14 end

```

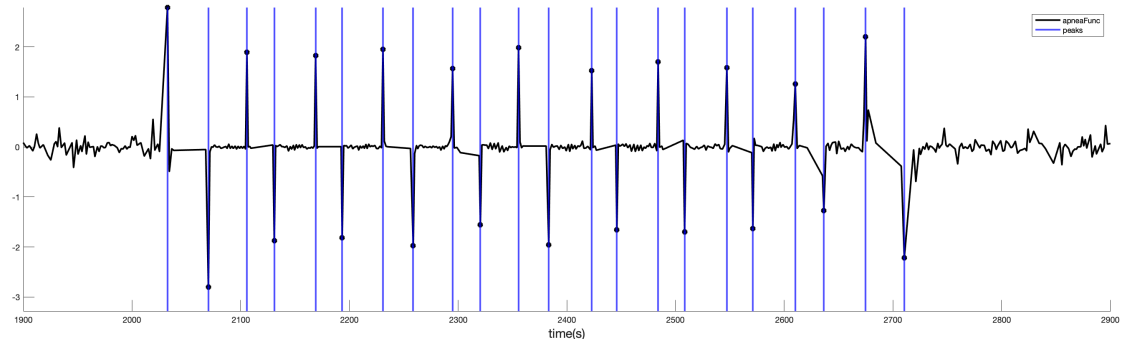


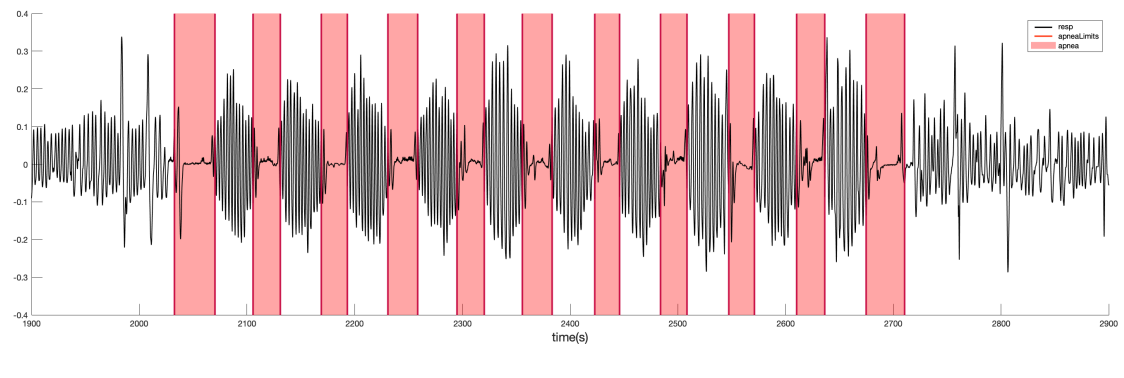
Figure 2.12: Inspiration and expiration automatic peaks detection

As a conclusion, the starting and ending points for each apnea phase are represented by these points.

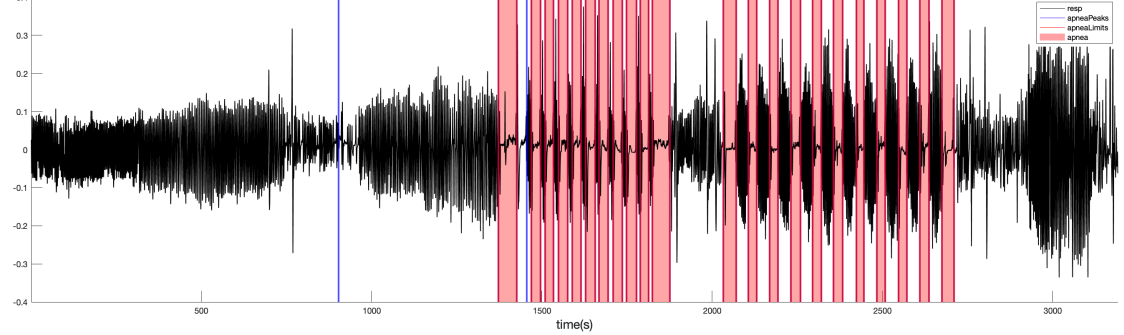
```

1 %apneaLim(1,:) : start time (POS pks)
2 %apneaLim(2,:) : stop time (NEG pks)
3 apneaLim = [];
4
5 apneaPksDiff = diff( apneaPks(1,:) );
6 for k=1:length(apneaPksDiff)
7 if apneaPksDiff(k)<60 && apneaPks(2, k+1 )<0 && apneaPks(2, k )>0
8 apneaLim=[apneaLim , [ apneaPks(1,k) ; apneaPks(1,k+1)] ];
9 end
end

```



(a)



(b)

Figure 2.13: Apnea automatic detection (a) in a maneuver and (b) in a recording

As in the laboratory protocols described above, it is noted that:

1. each maneuver is characterized by at least 7 periods of apnea;
2. each maneuver is always both preceded and followed by baseline periods.

Beginning with the first hypothesis, the entire maneuvering phase was defined as a time interval between two baselines. This gave us the indication to look for apneas that were further, spaced by baseline periods, allowing us to define the start and end of each maneuver. A period of 2.5 minutes was therefore chosen as the minimum delay between maneuvers, which corresponds to half of the average interval needed to return to baseline values of heart rate and pressure.

```

1 maneuvers = [];
2 threesholdApnea = 150; % 150 sec = 2.5 min
3
4 m=0;
5
6 for k=1:length(apneaLim)-1
7     if (apneaLim(1,k+1)-apneaLim(1,k)) < threesholdApnea
8         m=m+1; % num apneas in maneuvers
9     elseif m>3
10        maneuvers(1,n+1) = apneaLim(1, k-m);
11        maneuvers(2,n+1) = apneaLim(2, k);
12        m = 0;
13    end
14
15    if k==length(apneaLim)-1 && m>3
16        maneuvers(1,n+1) = apneaLim(1, k-m+1);
17        maneuvers(2,n+1) = apneaLim(2, k+1);
18    end
19 end

```

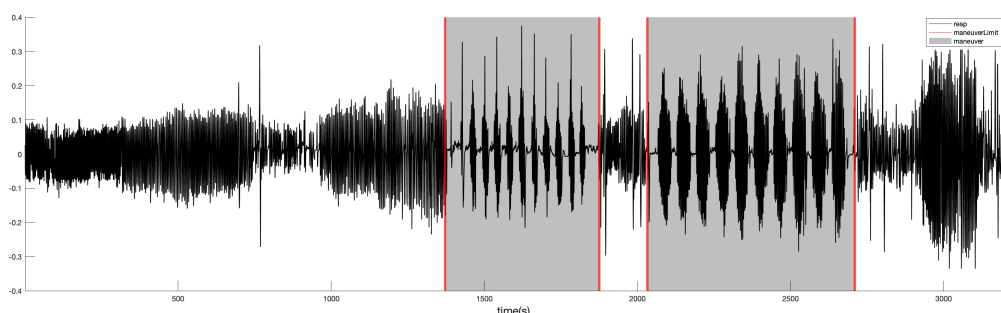


Figure 2.14: Maneuver automatic detection

The maneuvers just detected were validated by the second hypothesis reported. So the maneuvers with fewer than 7 apnea phases were discarded. By defining the maneuvers as a sequence of apnea/hyperventilation alternations, it follows that there are hyperventilation phases in the inter-apnea periods. The hyperventilation phase is consequently defined as the time between the end of the previous apnea period and the start of the next one.

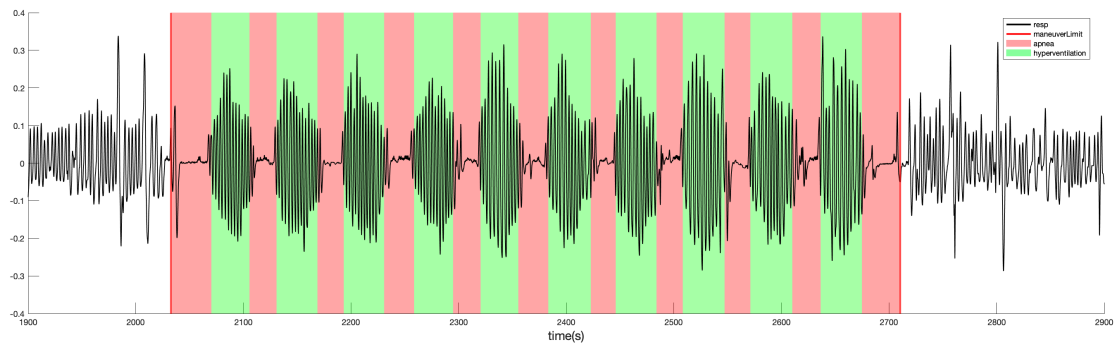


Figure 2.15: Apnea and hyperventilation phases detection in a maneuver

Baseline / Maneuvers phases detection

The baseline period refers to the time when the patient is at rest during the data collection process. The detection of this phase is crucial because if there is a clear distinction between baseline and maneuver a functional relationship between the variables is deduced. We used a combined study of the cardiovascular and respiratory systems to automatically detect the baseline phase. The feature describing the state of rest / excitation was therefore defined by interpolating of :

A) BPM (beats per minute), derived from the ECG signal processing, where a smoothing algorithm was used to remove any steps in the trace

```
1 ecgFeature = smoothdata( bpm, 'lowess', 30);
```

B) the air flow signals, which was resampled at the ECG sampling frequency after being processed with a smoothing method to remove any steps.

```
1 respFeature = diff( resp );
2 respFeature = movsum( respFeature , 5 );
3 respFeature = smoothdata( respFeature , 2000 );
4 respFeature =
5     resample( respFeature , length( ecgFeature ) , length( respFeature ) );
6 respFeature = detrend( respFeature );
```

C) The two multiplied variables generates a feature that increases proportionally to the patient's level of activity.

```
1 baselineFeature = ecgFeature .* respFeature ;
2 baselineFeature = baselineFeature.^2;
```

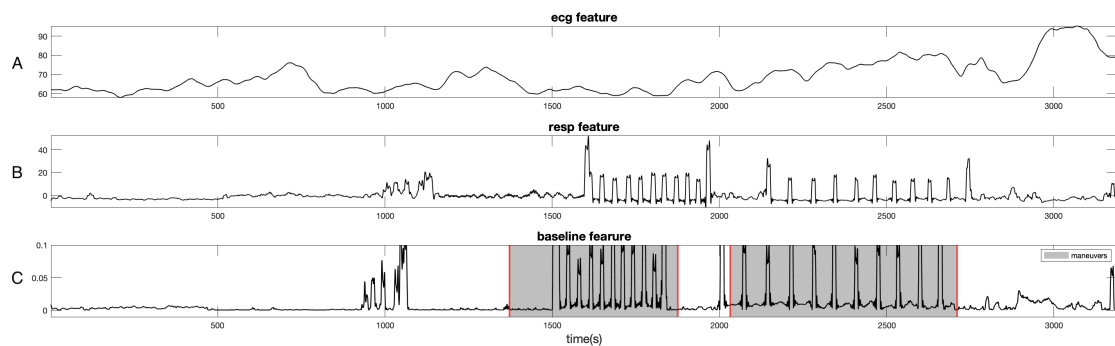


Figure 2.16: Maneuver automatic detection

Our research focuses on finding time frames that reflect the following characteristics: are included in the maneuvers and have a very low arousal state.

In the first instance, this is accomplished by looking at the derivative in the domain of the time of the newly defined adhoc variable and looking for points with zero derivative. These points correspond to moments of instantaneous phase change and they are taken as the start and end times of the baseline period.

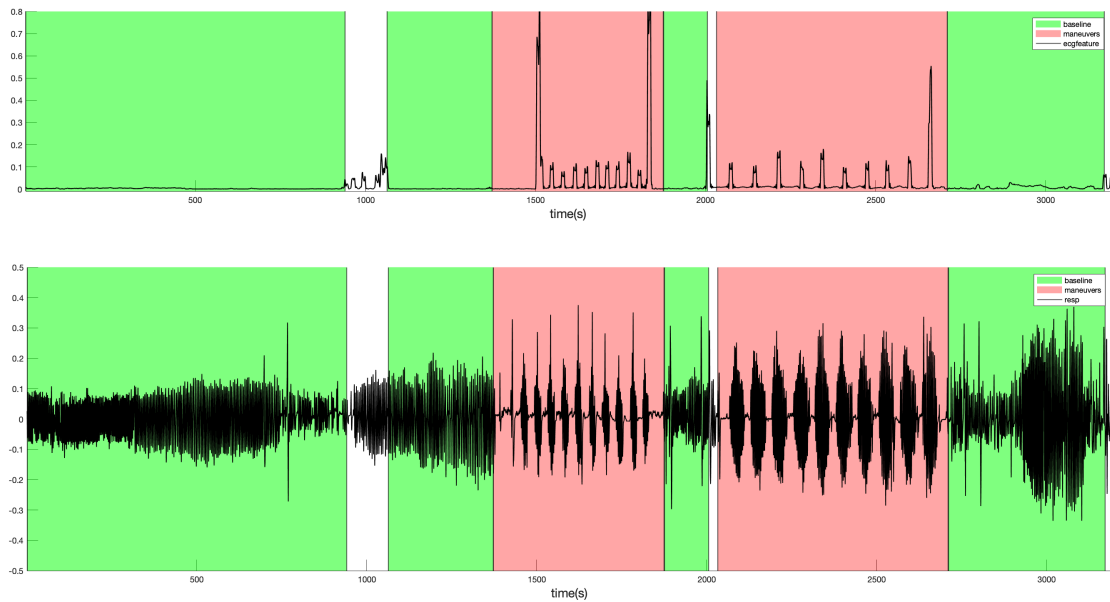


Figure 2.17: Baseline phases automatic detection

2.3.4 Cross-correlation between MSNA and ECG

The precise timing between the R peak and the burst in the MSNA signal was evaluated mostly visually, therefore the creation of a technique that could systematically characterize this synchronization and quantify the delay would be valuable.

This would be useful for analyzing bigger datasets and determining how consistent and variable this temporal connection is across different experimental circumstances.

We define two vectors, '*heart*' and '*nerve*', of dimension [1 x N]. N is the length of the recordings in analysis, re-sampled at a rate of 20 frames per second, which was chosen for the analysis.

```
1 fs = 20;
2 heart = zeros(1, fix(recLim(end, 2)*fs));
3 nerve = zeros(1, fix(recLim(end, 2)*fs));
```

The R wave and burst measurements are represented by the '*heart*' and '*nerve*' vectors, respectively.

Those are expressed by logical variables that are 1 at the time instant corresponding to the event and 0 elsewhere in the vector.

As a result, vector '*heart*' will have a value of 1 at time instants corresponding to the ECG's R points, and vector '*nerve*' will have a value of 1 at time instants corresponding to the MSNA bursts.

```
1 % fsNerve : 10k Hz
2 % fsHeart : 2k Hz
3 % x_pk : MSNA peaks time (sampled at fsNerve)
4 % x_R : ECG R peaks time (sampled at fsHeart)
5
6 x_pk_resampled = fix((x_pk / fsNerve) * fs);
7 x_R_resampled = fix((x_R / fsHeart) * fs);
8
9 heart(x_R_resampled) = 1;
10 nerve(x_pk_resampled) = 1;
```

By temporally translating the '*heart*' vector with respect to the '*nerve*' vector by one position at a time, we calculate the pairwise distance between the two vectors with a Jaccard metric method.

The minimum distance between those found, corresponds to the delay between the R wave and the bursts.

A permutation analysis was performed to determine the significance of the test, considering only the results lower than the 0.5 percentile of the null distribution.

```

1 n_lag = 50;
2 distance= nan(1 ,n_lag );
3 nullDistro=nan(1000 ,n_lag );
4
5 for jj = 1:n_lag
6     nerveTmp = nerve(jj :end);
7     heartTmp = heart(1:end-jj+1);
8
9     distance(jj) = pdist2(heartTmp ,nerveTmp , 'jaccard ')
10
11    for hh = 1 :1000
12        nullDistro(hh ,jj)=
13            pdist2(heartTmp ,nerveTmp(randperm(numel(nerveTmp))) , 'jaccard ')
14    end
15
16 end
17
18 nullDistro = min(nullDistro ,[] ,2);
19 [minDistance , lag] = min(distance);
20
21 if minDistance < prctile(nullDistro , 0.5)
22     delay(s) = lag/fs ;
23 end

```

2.3.5 PPG Signal

The algorithm's primary input is the PPG signal acquired from traditional pulse oximeters, which measures pulsatile blood volume in the fingertip.

According to the literature [74, 75], the PPG signal is reported to show a spontaneous low-frequency (LF) oscillations with a frequency (0.040.15 Hz) similar to autonomic variations in other cardiovascular signals including heart rate variability and blood pressure variability.

The difference between the maximum (peak) and minimum (nadir) values of the correspondent blood volume pulse-wave is then defined as the Pulse Wave Amplitude $PWA(i)$ time-series at each cardiac cycle (i).

A pulsatile physiological waveform ('pulse wave') attributable to heart synchronous variations is overlaid on a more slowly fluctuating baseline with different lower frequency components related to breathing, sympathetic nervous system activity, and thermoregulation in the PPG-signal [76, 77].

Drops in pulse wave amplitude (PWA) [78], as measured by PPG at each cardiac cycle, are known to directly reflect changes in peripheral blood flow related to vasoconstriction [79], and hence may provide a very simple indicator of autonomic activity.

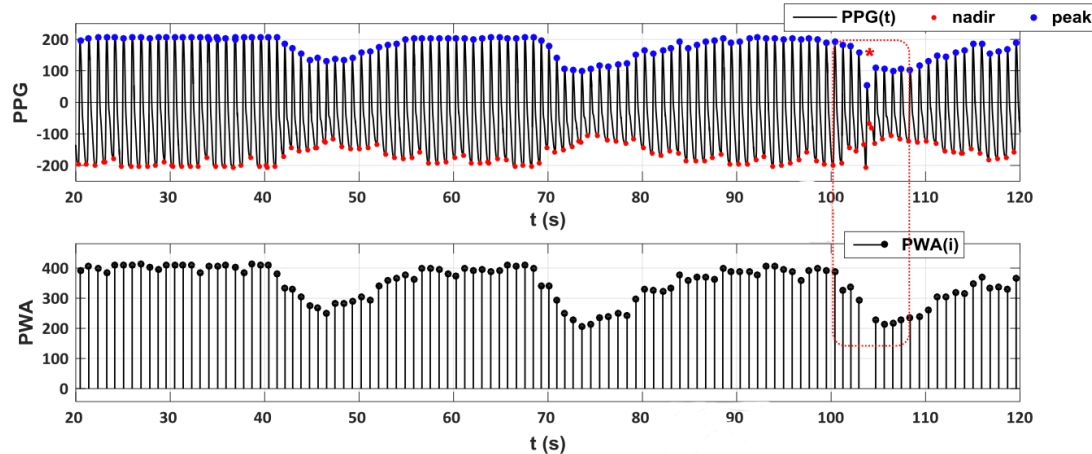


Figure 2.18: PWA signal extraction and preliminary artifact detection (*red)

The detection of these PWA-drops was implemented through the use of the algorithm described in the paper "Quantifying peripheral sympathetic activations during sleep by means of an automatic method for pulse wave amplitude drop detection" [80].

The algorithm's primary input is the PPG signal acquired from traditional pulse oximeters, which measures pulsatile blood volume in the fingertip. To reduce the amount of noise in the signal, high-pass ($\text{highpass}(pletFilt, 0.3, fs)$) and low-pass ($\text{lowpass}(pletRaw, 10, fs)$) filters are implemented.

The primary feature, the amplitude fluctuation of the pulsatile waveform associated with the cardiac cycle, was then derived.

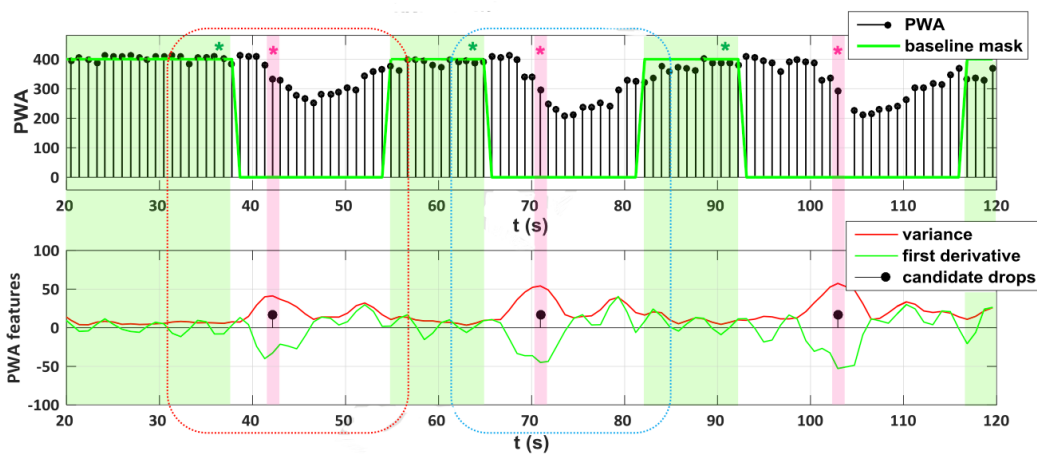


Figure 2.19: Time-varying PWA feature evaluation: baseline mask definition (*green) and candidate drop detection (*red)

For each confirmed PWA-drop a set of properties are estimated: the total duration d , the amplitude A (defined as the maximum absolute signal percent decrease within the drop), and the descending and ascending slopes (defined respectively as the decrement and increment in P% values divided by the time expressed in seconds), the area under the curve (AUC) of the PWA-drop.

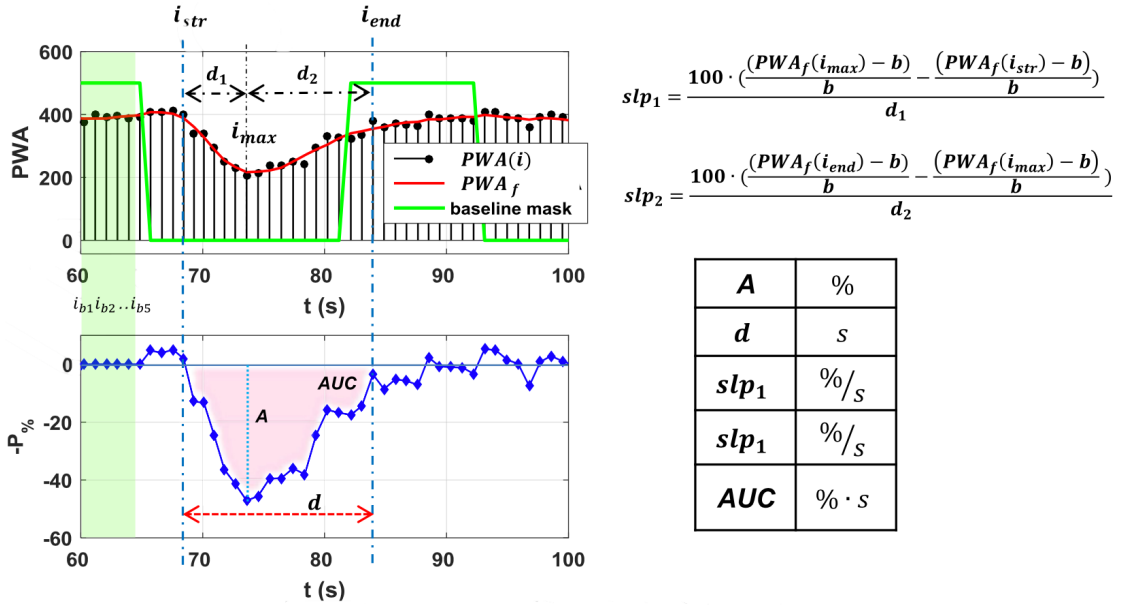


Figure 2.20: Description of the parameters extracted for each PWA-drop detected by the algorithm. The amplitude A , the duration d and the area under the curve AUC are graphically represented on the left, while the descending slp_1 and ascending slp_2 slopes are mathematically defined on the right. Finally, the table on the right summarizes the unit of measurement for each parameter.

The algorithm was tested against expert human scorers who visually inspected corresponding PPG-recordings as described in the paper [80]. The performance of the PWA-drop detection algorithm, expressed in terms of both sensitivity and precision, are reported in Table 2.1.

	ALL SLEEP	REM	NREM
Accuracy vs Score1 (F-score)	90.3%	90.1%	90.5%
Accuracy vs Score2 (F-score)	91.3%	91.0%	91.9%
Mean Sensitivity	90.8%	90.6%	91.2%
Mean Specificity	99.6%	99.7%	99.3%
Mean Precision	95.2%	95.1%	95.2%

Table 2.1: Table reports performance statistics for the algorithm.

2.3.6 Data Structure

The data has been reorganised in such a way that it would be simple to use. For each subject, all of the defined signals and features have been collected in '*struct*' containers. The graph in Figure 2.21 shows the structure with which the data were arranged.

The data were first sorted by the subject from which they were gathered: *sub1*, *sub2*, ..., *subN*. Multiple subdivision arise for each subject:

- *recs*: holds the multiple data records, each of which is filled with raw signals from the various sensors;
- *meta*: stores the registration metadata, which includes multiple information notes contained in the recordings;
- *nerve*: contains the entire subject's nerve raw trace recorded and the signals derived from its analysis (filtered signal, RMS signal, MSNA burst);
- *ecg*: contains the entire subject's ecg raw trace recorded and the signals derived from its analysis (filtered signal, PQR-wave, BurstPerMinute);
- *resp*: accomodate the complete subject's respiration raw trace recorded and the signals derived from its analysis (filtered signal, RespirationPerMinute(RPM), apnea phases information);
- *features*: is populated by the multiple features derived from various analysis during the algorithm (MSNA burst proximal to R-peaks, burst frequency, burst incidence, burst area, maneuvers information, baseline information)

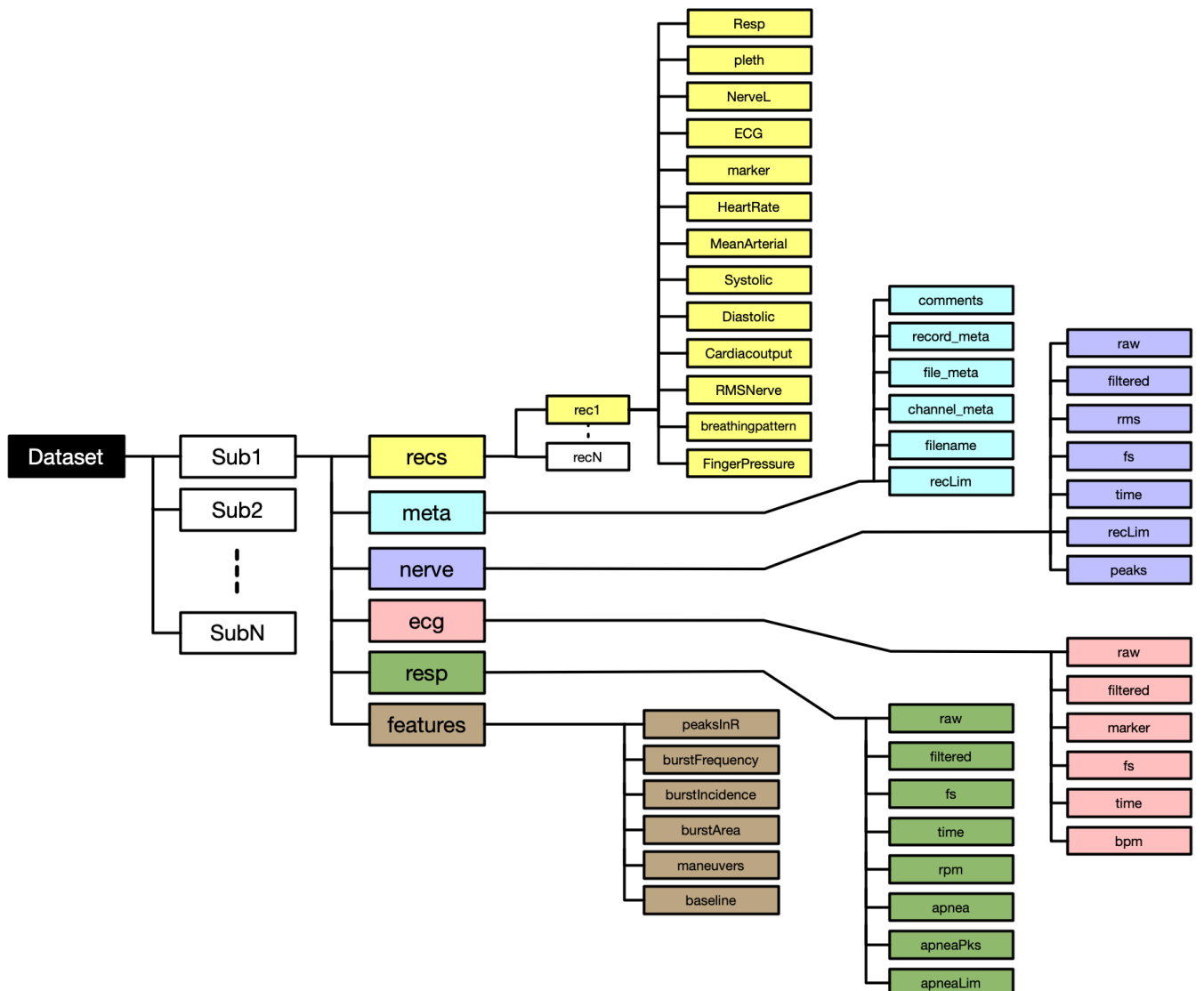


Figure 2.21: In the figure is shown the graph of the data structure.

2.3.7 Graphical User Interface (GUI)

A graphical user interface (GUI) has been designed to make the developed algorithm simple and easy to use. The GUI was developed with the *App Design* tool, which allows you to integrate Matlab software-based algorithms into a graphic environment. This tool is open-source and can be downloaded at the following link <https://github.com/valeriofantozzi/MSNA-GUI>.

The aim of this tool is to provide a guided and graphic approach for the clinical environment in order to speed up the process of cleaning the signal from the noise and the extraction of the features.

The GUI is divided into three sections:

- *LoadData* tab: allows the user to choose which files of a subject to analyze and displays a preview of a raw signal of their choice;

- *PreProcess* tab: the primary goal of this section is to prepare each signal for a further analysis by reducing the noise present in the raw trace and extrapolate the appropriate features. Once the signal has been preprocessed, the results can be saved on the hard disk;

The user can load raw data from '*.mat*' format files, using the '*select file*' button on the *LoadData* tab. After that, the selected data is imported and plotted. The user can select whatever channel and recording they want to review.

Lastly, the most significant information about the patient from whom the data was collected as well as specifics about the selected channel's signal are displayed.

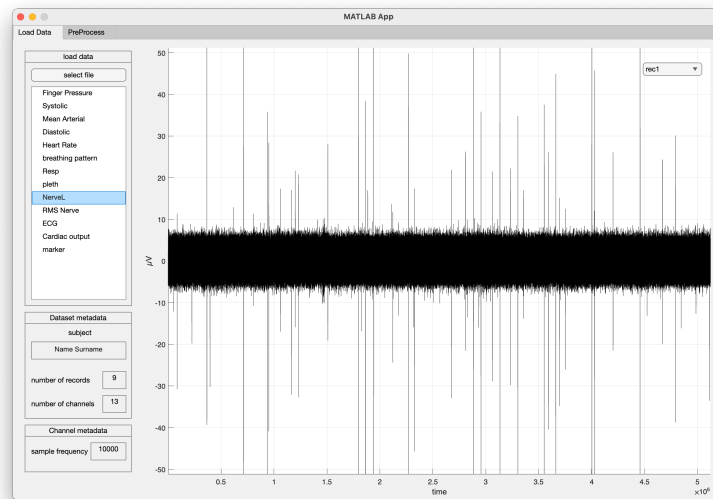


Figure 2.22: GUI \mapsto *LoadData Tab*

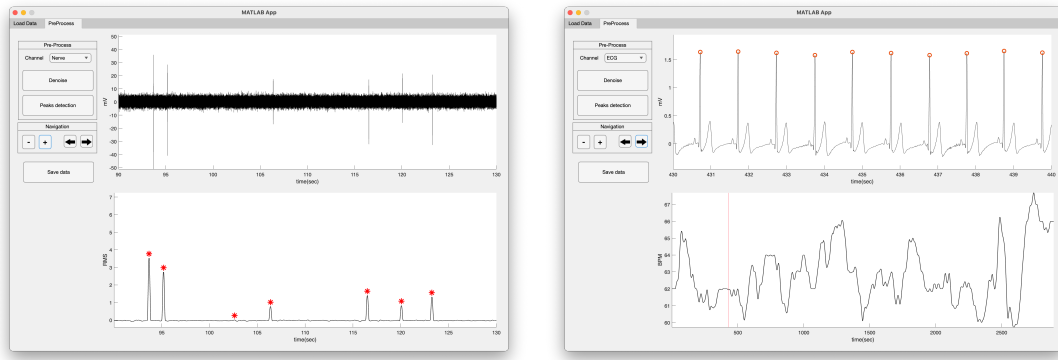
In the *PreProcess* tab the user can choose from the following signals for the analysis procedure: *Nerve*, *Ecg*, *Resp*, and *Ppg*.

The displayed signal is then presented by concatenating all of the recordings into a single track, allowing the user to navigate within it and adjust the temporal dimension of the shown segment using particular buttons.

Using the *Denoise* button, the user can initiate the process of noise estimation and reduction. The algorithms used in this approach are specific to the signal in question and are identical to those developed and presented earlier in this thesis.

Then, the second button launches the feature derivation procedure for the chosen signal, applying previously developed and discussed algorithms. The extracted features are then displayed.

The processed signals and obtained features can then be saved and used for an inter-subject analysis in the future.



(a) *Preprocess Tab* \mapsto Nerve

(b) *Preprocess Tab* \mapsto Nerve

Figure 2.23: GUI \mapsto Preprocess Tab

Chapter 3

Results

3.1 Algorithm validation

3.1.1 R-peak Detection

Manual scoring validation

The performance of the developed ECG algorithm was examined against the manual scoring of a blind operator, who visually reviewed each respiratory trace in the dataset and meticulously recorded each R-peaks. It was possible to objectively define if each R-peak was correctly identified or missed by the algorithm (true positive/false negative) and if each detected peak (false positive) lay in the proximity ($\pm 0.1\text{sec}$) of a true R-peak by comparing the algorithm output and the manual scoring. In the table 3.5, the total number of True Positive, False Positive, and False Negative events for each subject have been determined.

Therefore, we are able to get a total sensitivity value for our technique using the formula below.

$$\text{True positive} = (\text{R waves detected} - \text{False Positives}) = (34983 - 25) = 34985$$

$$\text{Sensitivity} = \frac{\text{True Positive}}{\text{True Positive} + \text{False Negative}} = \frac{34985}{34985 + 14} = 99.9\%$$

$$\text{Precision} = \frac{\text{True Positive}}{\text{True Positive} + \text{False Positive}} = \frac{34985}{34985 + 25} = 99.9\%$$

Our recordings contained very heterogeneous ECG traces since the experimental protocols involved not only baseline traces but also different respiratory manoeuvres.

Our technique had a high overall sensitivity (99.9%) and accuracy (99.9%), and we visually validated that neither false positive nor false negative cases were higher during manoeuvres than baseline phases.

Subject	False Positive	False Negative	R waves detected
1	1	0	2979
2	8	12	2855
3	0	1	3357
4	12	0	2058
5	0	0	3774
6	1	0	4308
7	0	0	6548
8	0	0	5057
9	3	1	4047
TOT	25	14	34983

Table 3.1: The Table shows the results for each subject of the manual scoring performed on the ECG signal.

Comparison validation

A second validation process was performed thanks to an open-source Matlab based graphical user interface for the detection and correction of R-peaks ('*R-DECO*') , available at <https://gitlab.esat.kuleuven.be/biomed-public/r-deco> [81].

The chosen algorithm shows a sensitivity of 99.60% and a positive predictive value of 99.69% when evaluated against the public MIT/BIH arrhythmia database, available at <https://physionet.org/content/mitdb/1.0.0/> [82].



Figure 3.1: A working example of the R-DECO’s GUI analysing the ECG signal of the dataset processed in this thesis. On the top is shown the ECG signal with the R-peaks detected and marked. On the bottom is shown the Beats Per Minute

We analysed the dataset loading the ECG signal in the R-DECO algorithm that is able to detect the R-peaks. The results of the two algorithms was compared as shown in the Table 3.2. The error in the difference of the number of R-peaks detected is maximum in subject 4 of 0.01% and in the remaining subjects of <0.01%.

Subject	Alg.1	Alg.2	error
1	2979	2979	0
2	2855	2857	2
3	3357	3358	1
4	2058	2041	17
5	3774	3773	1
6	820	820	0
7	3606	3609	3
8	5057	5058	1
9	4074	4066	8

Table 3.2: The table shows the comparison between the two R-peaks detection algorithms. Col Alg.1: R-peaks detected with our algorithm; Col Alg.2: R-peaks detected with R-DECO algorithm

If we evaluate the temporal shifting of the R-peaks found with the R-DECO algorithm with respect to those identified by the algorithm developed in this thesis, we can notice a maximum average error of 2.5 ms and a maximum standard error of 0.2 ms as shown in the Table 3.3. This analysis is based on the assumption that only the R peaks of the algorithm we proposed were associated with those of the R-DECO algorithm, and that those that were identified as errors by the previous analysis were discarded.

Subject	MeanError (ms)	StandardError (ms)
1	-0.15	0.04
2	0.78	0.24
3	1.48	0.04
4	1.34	0.24
5	0.40	0.01
6	1.42	0.09
7	-2.51	0.13
8	0.76	0.07
9	2.51	0.15

Table 3.3: The table shows for each subject the temporal error between the R-peaks derived by the R-DECO and the proposed algorithm. The Mean Error between the bursts and the relative Standard Deviation was reported for each subject. The results obtained were reported in milliseconds.

3.1.2 Inspiration Peak Detection

The performance of the respiration algorithm here developed were validated against the independent manual scoring of a blind operator, who visually inspected each single respiratory trace in the dataset and carefully marked each inspiration peak.

Directly comparing the algorithm output and the manual scoring it was possible to objectively define if each inspiration peak was correctly identified or missed by the algorithm (true positive/false negative) and if each detected peak (false positive) lay in the proximity ($\pm 0.5\text{sec}$) of a true inspiration peak. The total number of True Positive, False Positive and False Negative cases have been reported separately for each subject in table 3.4. Finally, applying the formula reported below, we could evaluate a total sensitivity value for our procedure.

Subject	False Positive	False Negative	Inspiration peaks
1	8	0	737
2	7	2	610
3	4	11	775
4	13	3	585
5	10	3	741
6	4	17	1032
7	4	3	1344
8	4	3	995
9	6	1	953
TOT	60	43	7772

Table 3.4: The Table shows the results for each subject of the manual scoring performed on the respiration signal.

From this analysis we can therefore derive:

$$\text{True positive} = (\text{Detected peaks} - \text{Falsi Positivi}) = (7772 - 60) = 7712$$

$$\text{Sensitivity} = \frac{\text{True Positive}}{\text{True Positive} + \text{False Negative}} = \frac{7712}{7712 + 43} = 99.4\%$$

$$\text{Precision} = \frac{\text{True Positive}}{\text{True Positive} + \text{False Positive}} = \frac{7712}{7712 + 60} = 99.2\%$$

Our recordings contained very heterogeneous respiratory traces since the experimental protocols involved not only normal breathing but also different respiratory manoeuvres.

Very interestingly, our procedure reached overall high sensitivity (99.4%) and precision (99.2%) levels and we visually verified that nor false positive nor false negative cases were higher during manoeuvres in respect to baseline values.

3.2 MSNA burst analysis

3.2.1 Burst incidence in cardiac interval

Given the established interrelationship between the cardiovascular system and the SNS [83, 25, 32], the first analysis conducted has the purpose of evaluate the average of bursts present in each cardiac cycle. By cardiac interval is meant the time interval between one R point and the next on the ECG trace.

Being aware of the event time of each R point and burst, the number of burst inside all the R-R interval has been counted for every subject.

By averaging over the entire population of subjects studied, we found that 79% of cardiac cycles hold no bursts per interval and 18% hold one burst per interval.

Our result results comparable with the one founded in previous studies [83, 25, 32] that show approximately an average of 75% cycles without burst and 15% cycles with one burst.

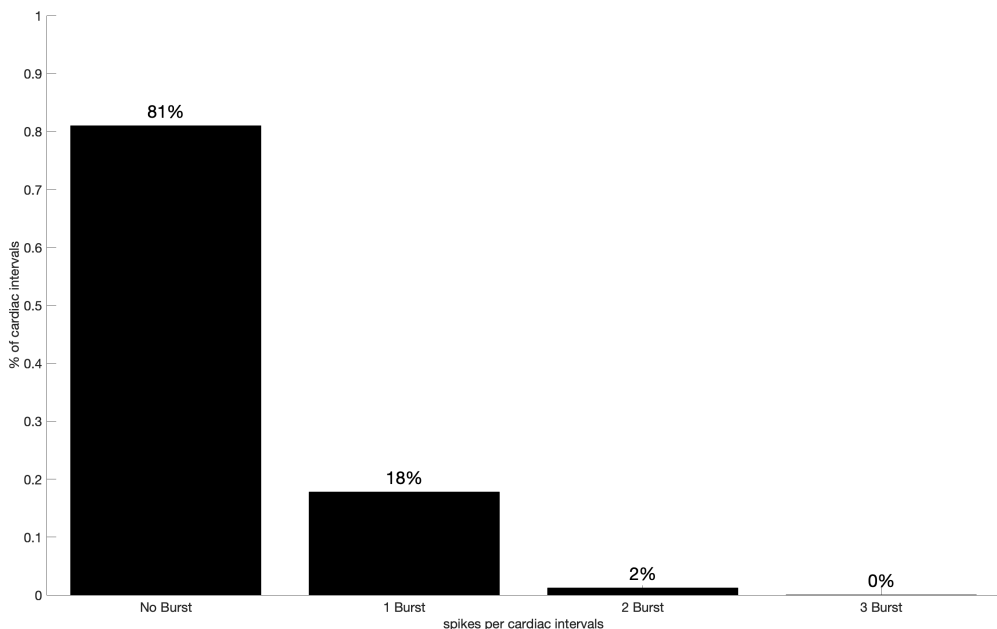


Figure 3.2: The figure shows the histogram of the number of spikes averaged over the entire population of the dataset that fall in the cardiac interval.

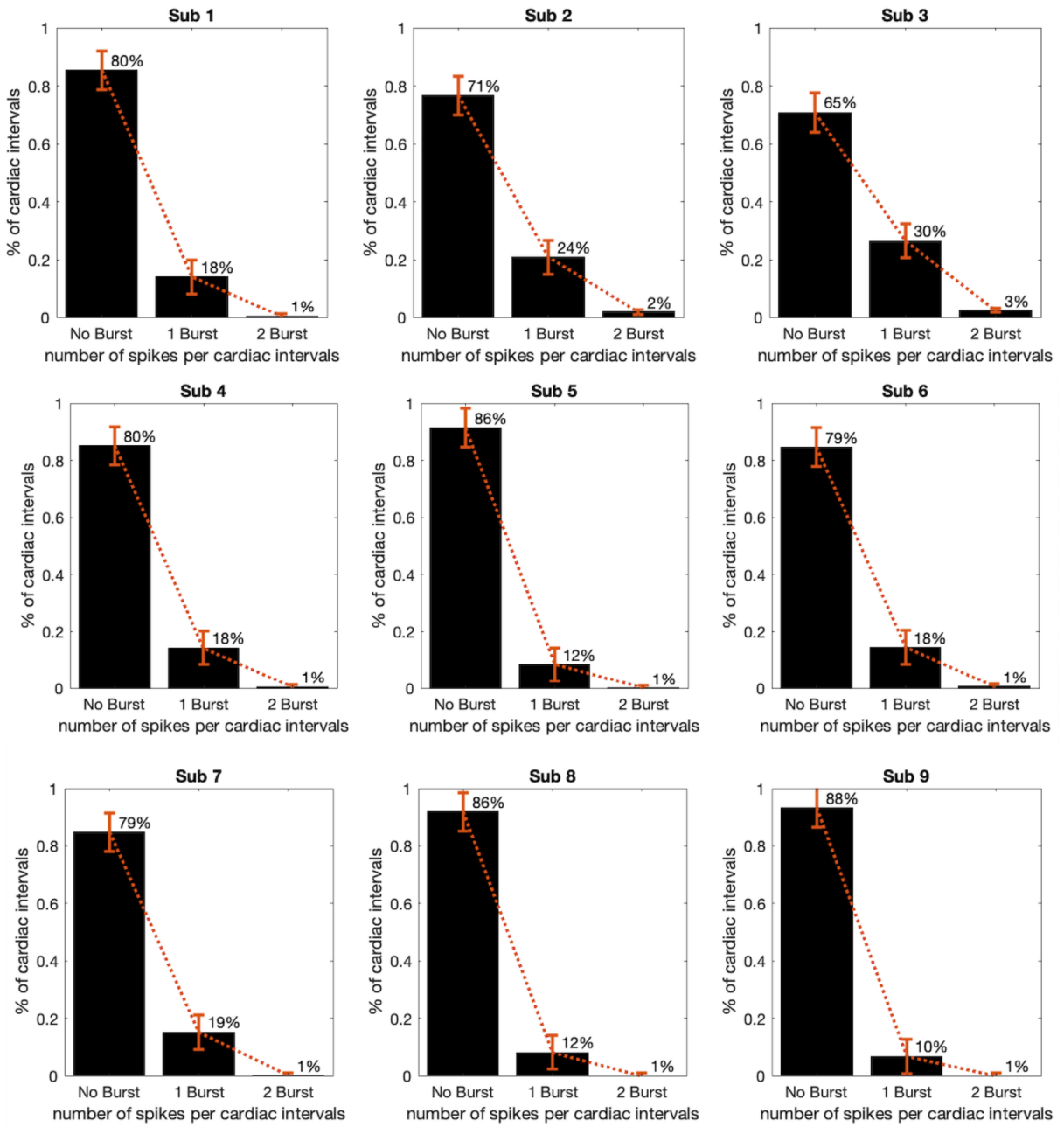


Figure 3.3: The figure shows the histogram of the number of spikes for each subject that fall in the cardiac cycle. the horizontal red lines indicate di variance of the measure.

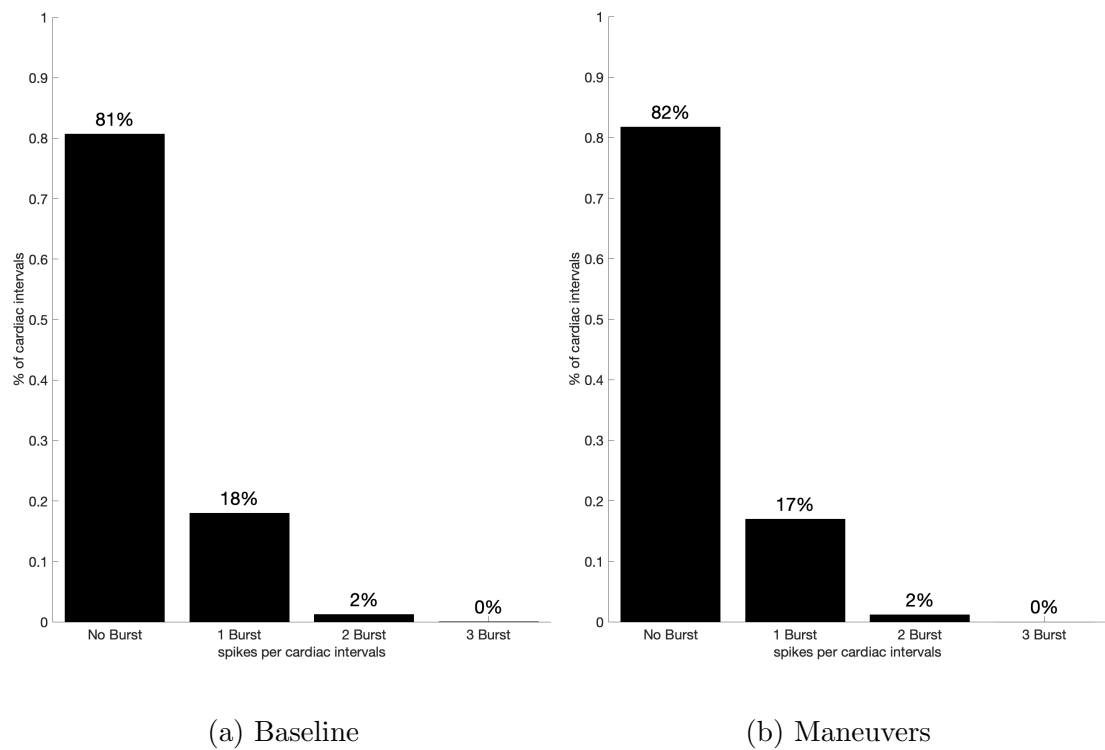


Figure 3.4: The figure shows the histogram of the number of spikes averaged over the entire population of the dataset that fall in the cardiac cycle during a) the baseline phase and b) the maneuvers phase.

3.2.2 Features analysis

The MSNA features were then divided into two categories based on their time occurrence: baseline and maneuvers events. The BPM signal was used as a reference data in the study to ensure that the approach was viable. A t-test was performed for each feature tested, and the p-value associated is reported in the Table 3.5. Burst Area and Burst Amplitude shows a p-value <0.05 , making them significant for the investigation.

It is therefore possible to notice how the average value of both Burst Area and Burst Amplitude show a decrease between the baseline and the maneuver period.

	BPM	Burst Area	Burst Amplitude	Burst Duration	Burst frequency	Burst Incidence
p-value	0.02	0.03	0.04	0.21	0.11	0.14

Table 3.5: The Table shows the p-values of a paired-sample t-test

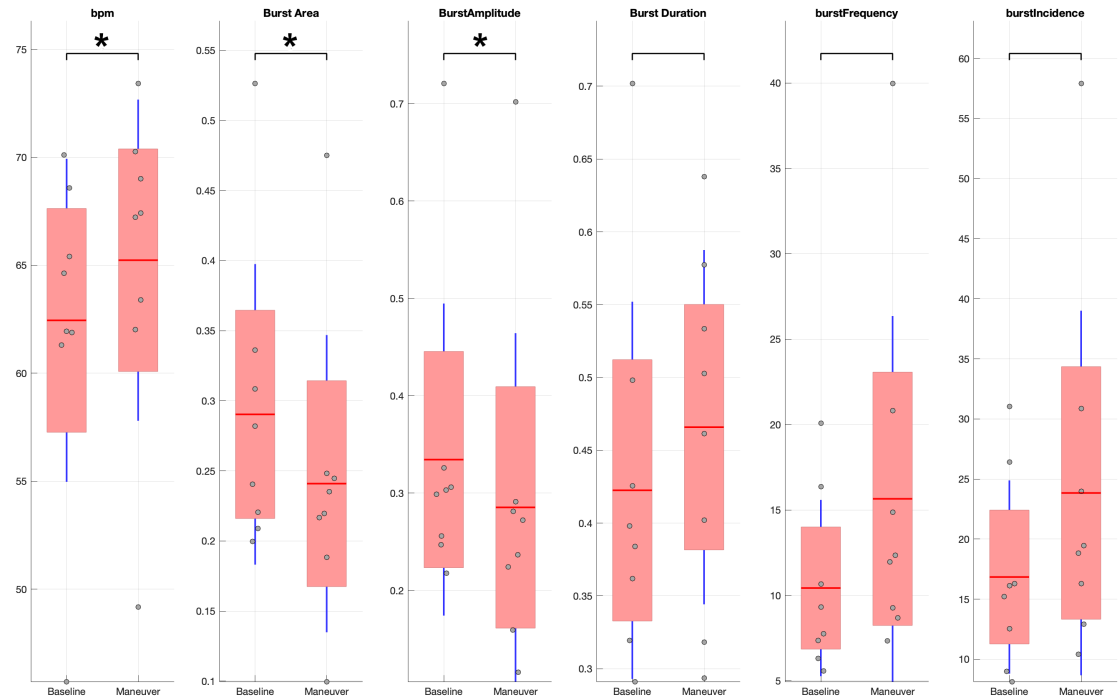


Figure 3.5: The figure shows the box plot of the features calculated during Baseline and Maneuvers. The marker (*) indicate a $p\text{-value} < 0.05$. The red lines indicate the mean value of the features and the blue lines indicate the variance of the feature. The grey markers indicate for each subject the mean value of the feature.

3.2.3 Baroreflex delay

The figure 3.6 shows the curves obtained from the cross-correlation analysis.

It shows the results of implementing the *Jaccard* approach to calculate the distance between the occurrence vector of the R peaks and the MSNA bursts as the temporal lag between the two varies. The temporal lag associated with the shortest distance relates to the delay between the two vectors which maximize the synchronization between the two events. The statistical analysis with the permutation test allowed us to evaluate whether the level of synchronization between the two time-series is significantly greater than that which could be randomly generated between the two time-series.

The Table 3.6 shows for each subject the valid delay in seconds resulted by the cross-correlation analysis between MSNA and ECG. To determine the test's significance, a permutation analysis was performed , with only the results below the null distribution's 0.5 percentile being considered.

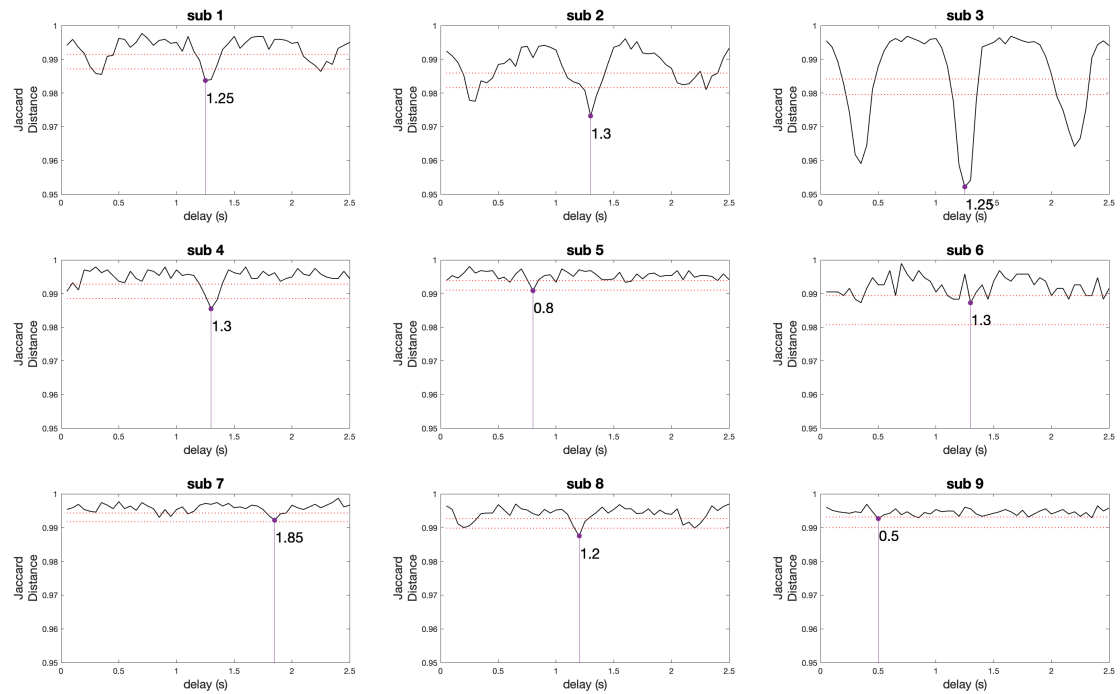


Figure 3.6: The figure shows for each subject the distances calculated between the occurrence vector of the R peaks and the MSNA bursts as the temporal lag between the two varies. The reported value indicated the minimum distance calculated. The red dotted lines indicates the null-distribution's 0.5 percentile (upper line) and 9.5 percentile (lower line)

subject	1	2	3	4	5	6	7	8	9
delay (sec)	1.25	1.3	1.25	1.3	0.8	X	X	1.2	X

Table 3.6: The table shows the results of the cross-correlation analysis reporting only the delays below the null distribution's 0.5 percentile. The delays marked by an X were greater than the null distribution's 0.5 percentile and then discarded.

The median value of the delays calculated is 1.25 seconds. The identified delay should be applied to the ECG signal, which is delayed relative to the MSNA signal.

3.2.4 Baroreflex delay distribution

The highlighted delays resulted by the cross-correlation analysis between MSNA and ECG were then analyzed with the aim of going to see how the individual delays differ for each subject (for each R peak and burst) with respect to the average delay value.

Figure 3.7 and Figure 3.8 show both the distribution of the single delay error with regard to the average given in the preceding study with the difference that the first one is a comparison between baseline and maneuvers phases and the second one compare apnea and hyperventilation periods.

First of all, the pairs of bursts and R points located in the baseline and maneuver time frames were divided. The maneuvers were also subdivided into apnea and hyperventilation stages.

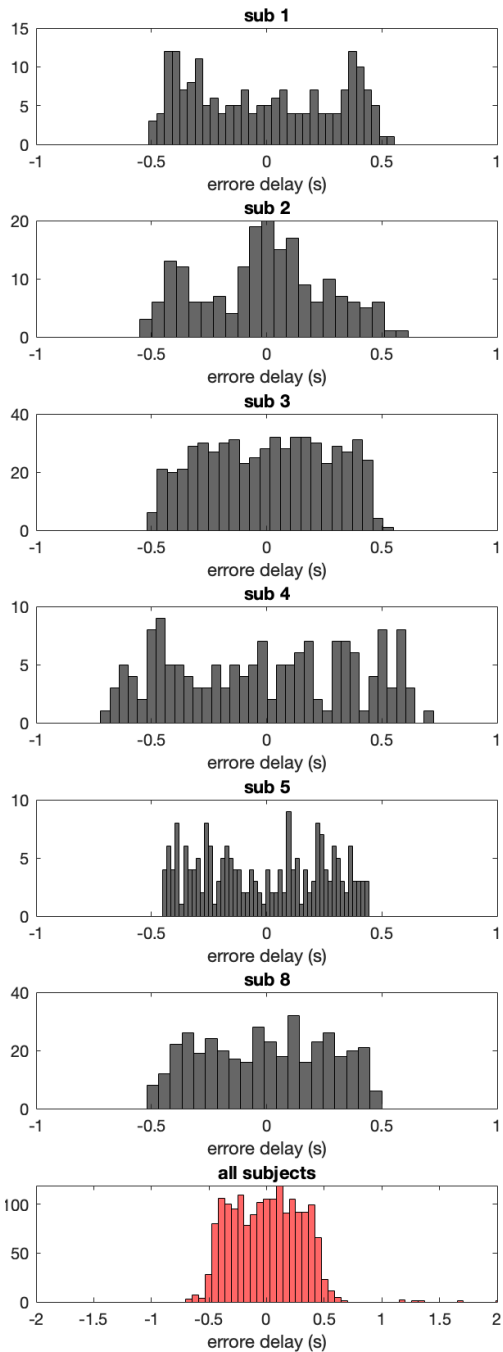
The delay distributions of the burst around the point R were then evaluated.

As shown, the estimated delays remain around the R point with a maximum detachment of 0.5 seconds.

This result confirms what previous studies have found [12, 13, 20, 27, 30, 32], that the burst is delayed $1.25\text{sec} \pm 0.5\text{sec}$ after the R wave occurs.

It should be noted that the distribution contains components that are higher than 0.5 seconds during the maneuver phases (apnea and hyperventilation).

Baseline



Maneuvers

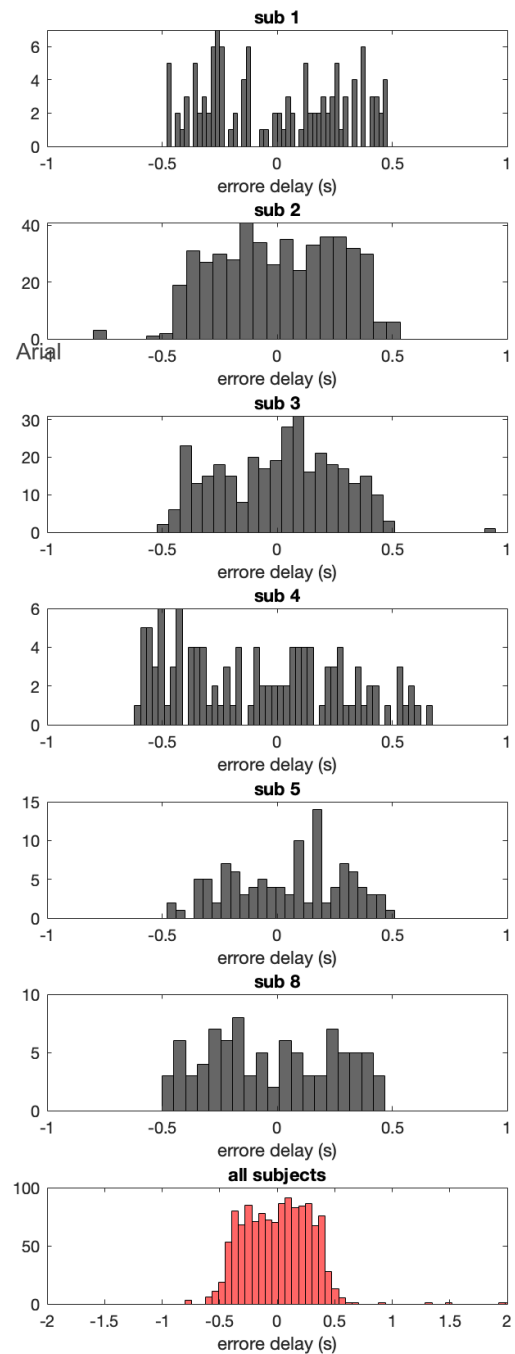
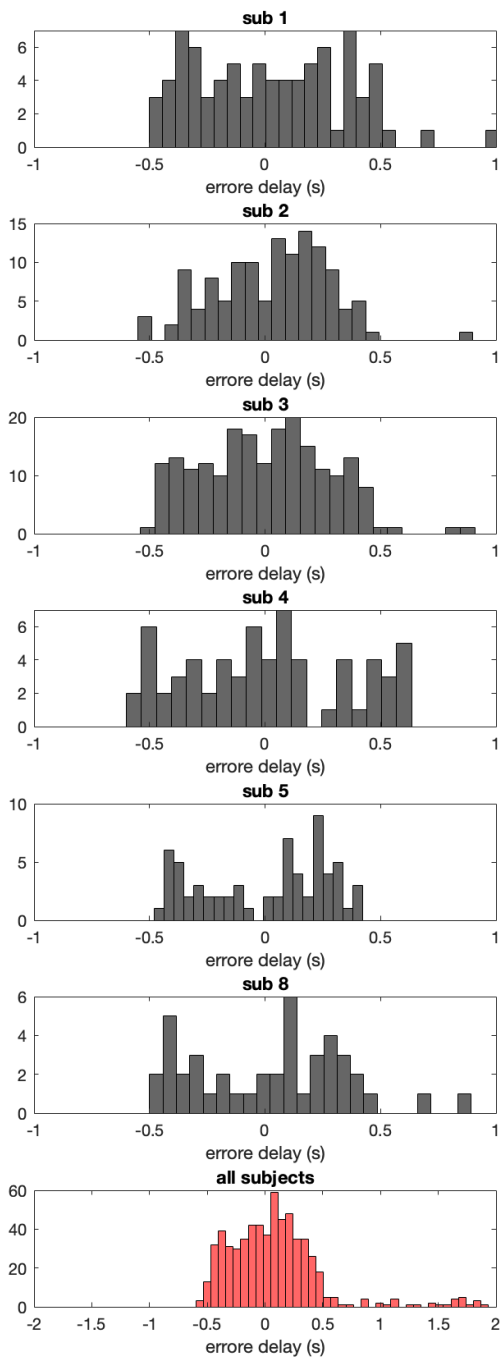


Figure 3.7: Comparison between Baseline (on the left) and Maneuvers (on the right) phases of distribution of the error of the single delay with respect to the average

Apnea



Hyperventilation

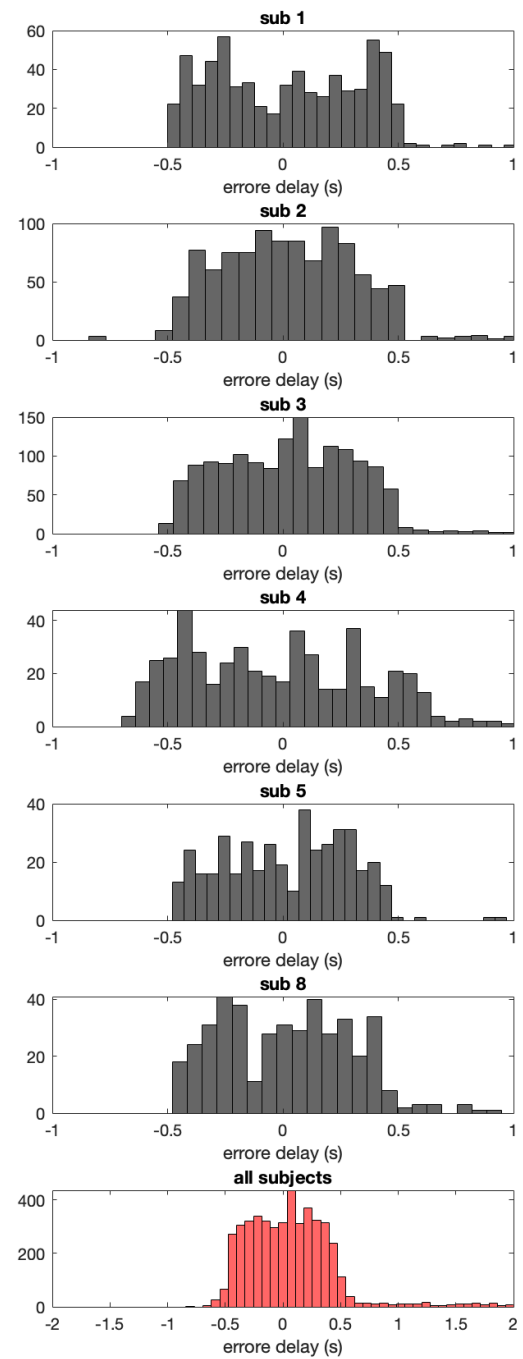


Figure 3.8: Comparison between Apnea (on the left) and Hyperventilation (on the right) phases of distribution of the error of the single delay with respect to the average

3.2.5 Respiration delay

The cross-correlation analysis was performed also to better investigate the relationship between the respiration signal and the occurrence of burst of SNA in the MSNA signal.

The results shows not to be valid by the permutation test, thus assuming from this analysis there is no temporal interrelationship between the two systems.

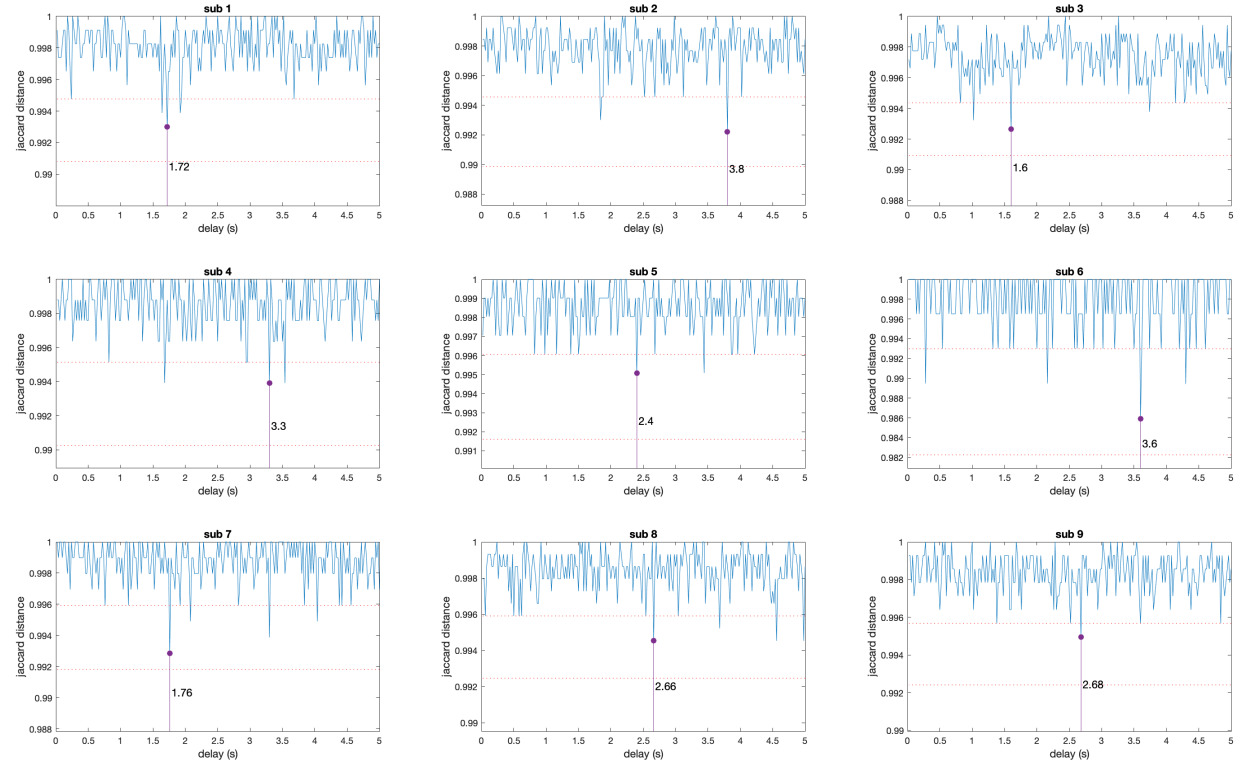


Figure 3.9: The figure shows for each subject the distances calculated between the occurrence vector of the inspiration peaks and the MSNA bursts as the temporal lag between the two varies. The reported value indicated the minimum distance calculated. The red dotted lines indicates the null-distribution's 0.5 percentile (upper line) and 9.5 percentile (lower line)

3.2.6 MSNA-PWA relationship

The variability of the features that fall in the temporal period fixed on the PWA-drops event, as obtained from the PPG signal analysis, was investigated.

As shown in the Figure 3.10, the average values and relative variances for each time instant of the selected features were evaluated in the PWA-drop event range of ± 45 sec.

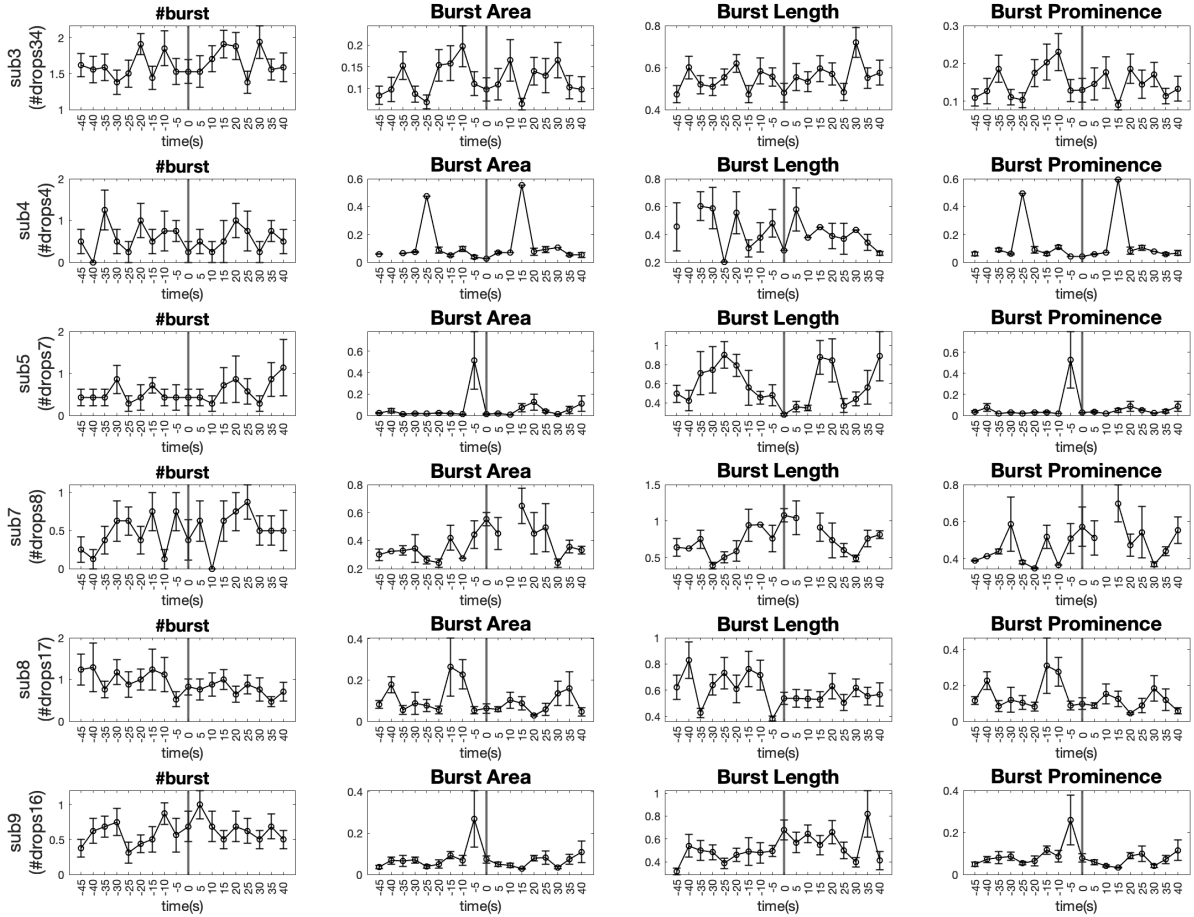


Figure 3.10: The figure shows for each subject the features mean amplitude variation around the PWA drop event. The time lapse taken into consideration is in the PWA-drop event range of ± 45 sec.

Finally, as shown in Figure 3.11, the variability of each feature was estimated for each instant of time by averaging the values obtained earlier for each subjects.

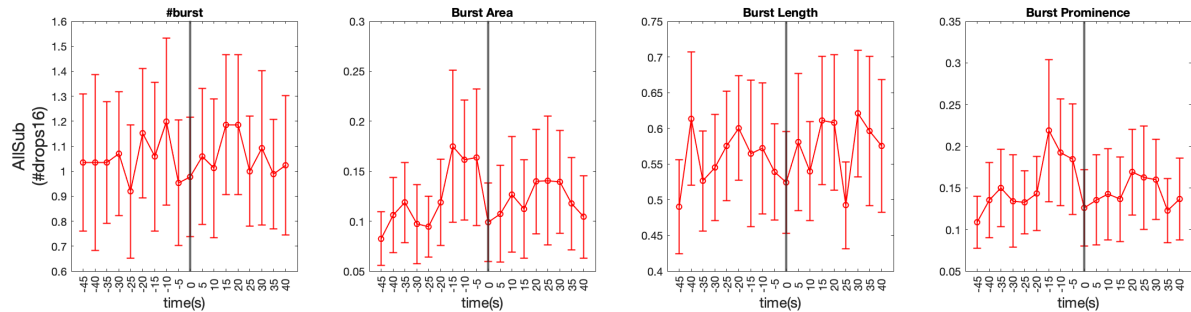


Figure 3.11: The figure shows the mean of the subjects features amplitude variation around the PWA-drop event.

Chapter 4

Discussion

The project's ultimate aim was to develop tools that could systematically characterize potential relationships between MSNA and peripheral non-invasive signals, and then identify surrogate non-invasive features that correlate with MSNA derived features and could be used as potential predictors of sympathetic activity levels. The MSNA signal of 9 healthy volunteers was recorded simultaneously with non-invasive bio-signals such as blood pressure, electrocardiographic (ECG) signal, photoplethysmographic (PPG) signal, and air flow. Following a baseline assessment, each subject was given a series of guided voluntary breathing maneuvers to assess non-steady-state relationships. Considering the relatively high complexity of the experimental setup (e.g., breathing maneuvers interleaved with resting state), we developed an ad-hoc set of algorithms able to process bio-signals in these non-stationary conditions.

Therefore, a Matlab toolbox has been built that can perform an automatic analysis of all of the signals discussed above. Each signal had first been cleaned of artifacts before being processed to extrapolate a wide range of features that were determined following a comprehensive review of the literature.

The ECG and Respiration signal processing algorithms were both validated by analyzing the peaks derived from the pre-processing algorithms in order to ensure that the analysis process was reliable.

The R peaks derived from the ECG signal are then used via two processes to authenticate their validity.

By comparing the algorithm output with the manual scoring, it was possible to objectively determine if each R-peak was accurately recognized or missed by the algorithm (true positive/false negative) and whether each detected peak (false positive) was within 0.1 sec of a real R-peak. Because the experimental protocols included not just baseline traces but also varied breathing exercises, our recordings comprised a wide range of ECG traces. We visually checked that neither the

number of false positives nor false negatives increased during maneuvers compared to baseline, and our method had a high overall sensitivity (99.9%) and accuracy (99.9%).

R-DECO, an open-source Matlab algorithm for identifying and correcting R-peaks, was also used to compare the R peaks found by us. The chosen algorithm has a sensitivity of 99.60% and a positive predictive value of 99.69% when tested against the public MIT / BIH arrhythmia database. The difference in number of peaks recognized by the two algorithms was thus determined to be less than 0.1% inaccurate. Even when the number of R peaks identified is approximately the same, the two methods produce slightly discordant results with a 1% difference in accuracy due to the different noise reduction strategies and artifacts used. When comparing the temporal shifting of the R-peaks detected using the R-DECO method to those identified by the technique proposed in this thesis, we see a maximum average inaccuracy of 2.5 ms and a maximum standard error of 0.2 ms.

The respiration signal was exposed to a procedure similar to the previous one. The signal is characterized by peaks that occur at the outmost of an inspiration. These markers were compared to those found through manual scoring to derive whether each peak was recognized or not by the automatic detection algorithm (true positive / false negative) and whether each detected peak (false positive) was within 0.5 sec of a real peak. The method also ensured that neither the number of false positives nor false negatives increased during maneuvers when compared to baseline. Our method showed had a high overall sensitivity (99.4%) and accuracy (99.2%).

Consequently, a set of algorithms have been developed to perform an automatic processing of the MSNA signal. The methods were formulated based on strategies shared by the scientific community [11, 25, 12]. The literature, however, does not exhibit a gold standard for the detection and validation of the MSNA signal apart from the visual analysis of the clinician. The proposed algorithms are instead capable of automatically detecting MSNA bursts.

The temporal relationships discovered between MSNA peaks and cardiac cycle R peaks are consistent with previous studies. However, according to past research, the delay results are never calculated using scientific approach [12, 13, 20, 27, 30, 32]. We present a methodology for calculating the baroreflex delay utilizing systematic techniques, as well as a measure of the missing error delay in the literature, presented for the first time in this work. Both steady-state (baseline) and non-steady-state (maneuver) conditions were used to calculate the error delay. The relationship between MSNA bursts and R-peaks appears to change during the

subject's voluntary breathing maneuvers.

It was also observed that the features derived from the MSNA signal vary in the time span close to the drop in the PWA signal, which is associated with a 40% decrease of the signal. In fact, between 10 and 20 seconds before the drop, there is a qualitative increase in the amplitude and area of the MSNA bursts. This behavior is supposed to reflect increases in sympathetic output that drive a peripheral vasoconstriction. This discovery might be significant since it suggests that PWA-drop could be used as a non-invasive marker of increased sympathetic activity. This pattern is consistent with recent research linking a rise in the prevalence of PWA-drop to a variety of diseases [84] .

Because statistical analysis on a large sample of participants is not available, the aforementioned observations are currently only in qualitative nature.

Through the construction of an open-source toolkit with a GUI, very easy to use even in a clinical setting, this thesis work delivers a useful tool to the scientific community. It will enable comparable analyses to be performed on large samples, allowing the first evidences to be verified and expanded.

This study paves the way for comparative analyses to be performed on large samples, allowing the data analyses developed to be verified and expanded.

Bibliography

- [1] *Trattato di anatomia umana*, vol. 3. edi-ermes.
- [2] A. Santuz, “Extracting muscle synergies from human steady and unsteady locomotion: methods and experiments,” 08 2018.
- [3] D. Robertson, *Primer on the Autonomic Nervous System (Third Edition)*. Elsevier, 2012.
- [4] L. PA, “Clinical autonomic disorders,” *The role of the sympathetic skin response in the assessment of autonomic function*, pp. 231–241, 1993.
- [5] Conti, *Fisiologia Medica*, vol. 1. edi-ermes, 2010.
- [6] J. M. Karemaker, “An introduction into autonomic nervous function,” *Physiol Meas*, vol. 38, pp. R89–R118, May 2017.
- [7] A. Woodruff, “action potentials and synapses(<https://qbi.uq.edu.au/brain-basics/brain/physiology/action-potentials-and-synapses>).”
- [8] A. B. Vallbo and K. E. Hagbarth, “Impulses recorded with micro-electrodes in human muscle nerves during stimulation of mechanoreceptors and voluntary contractions,” *Electroencephalogr Clin Neurophysiol*, vol. 23, p. 392, Oct 1967.
- [9] A. B. Vallbo, K.-E. Hagbarth, and B. G. Wallin, “Microneurography: how the technique developed and its role in the investigation of the sympathetic nervous system,” *J Appl Physiol (1985)*, vol. 96, pp. 1262–9, Apr 2004.
- [10] N. D. J. Strzalkowski, R. M. Peters, J. T. Inglis, and L. R. Bent, “Cutaneous afferent innervation of the human foot sole: what can we learn from single-unit recordings?,” *J Neurophysiol*, vol. 120, pp. 1233–1246, 09 2018.
- [11] J. L. Greaney and W. L. Kenney, “Measuring and quantifying skin sympathetic nervous system activity in humans,” *J Neurophysiol*, vol. 118, pp. 2181–2193, 10 2017.

- [12] V. G. Macefield, “Recording and quantifying sympathetic outflow to muscle and skin in humans: methods, caveats and challenges,” *Clin Auton Res*, vol. 31, pp. 59–75, 02 2021.
- [13] E. C. Hart, G. A. Head, J. R. Carter, B. G. Wallin, C. N. May, S. M. Hamza, J. E. Hall, N. Charkoudian, and J. W. Osborn, “Recording sympathetic nerve activity in conscious humans and other mammals: guidelines and the road to standardization,” *Am J Physiol Heart Circ Physiol*, vol. 312, pp. H1031–H1051, May 2017.
- [14] T. Mano, “Microneurographic research on sympathetic nerve responses to environmental stimuli in humans.,” *Jpn J Physiol*, vol. 48, pp. 99–114, Apr 1998.
- [15] V. G. Macefield, A. R. Burton, and R. Brown, “Somatosympathetic vasoconstrictor reflexes in human spinal cord injury: Responses to innocuous and noxious sensory stimulation below lesion,” *Front Physiol*, vol. 3, p. 215, 2012.
- [16] K. E. Hagbarth and A. B. Vallbo, “Pulse and respiratory grouping of sympathetic impulses in human muscle-nerves,” *Acta Physiol Scand*, vol. 74, no. 1, pp. 96–108, 1968.
- [17] V. G. Macefield and B. G. Wallin, “Modulation of muscle sympathetic activity during spontaneous and artificial ventilation and apnoea in humans,” *J Auton Nerv Syst*, vol. 53, pp. 137–47, Jun 1995.
- [18] J. Fagius and B. G. Wallin, “Long-term variability and reproducibility of resting human muscle nerve sympathetic activity at rest, as reassessed after a decade,” *Clin Auton Res*, vol. 3, pp. 201–5, Jun 1993.
- [19] K. E. Hagbarth, R. G. Hallin, A. Hongell, H. E. Torebjörk, and B. G. Wallin, “General characteristics of sympathetic activity in human skin nerves,” *Acta Physiol Scand*, vol. 84, pp. 164–76, Feb 1972.
- [20] W. Delius, K. E. Hagbarth, A. Hongell, and B. G. Wallin, “General characteristics of sympathetic activity in human muscle nerves,” *Acta Physiol Scand*, vol. 84, pp. 65–81, Jan 1972.
- [21] C. N. Young, D. M. Keller, C. G. Crandall, and P. J. Fadel, “Comparing resting skin sympathetic nerve activity between groups: caution needed,” *J Appl Physiol (1985)*, vol. 106, pp. 1751–2; author reply 1753, May 2009.
- [22] N. Charkoudian, M. J. Joyner, C. P. Johnson, J. H. Eisenach, N. M. Dietz, and B. G. Wallin, “Balance between cardiac output and sympathetic nerve

- activity in resting humans: role in arterial pressure regulation,” *J Physiol*, vol. 568, pp. 315–21, Oct 2005.
- [23] I. T. Fonkoue and J. R. Carter, “Sympathetic neural reactivity to mental stress in humans: test-retest reproducibility,” *Am J Physiol Regul Integr Comp Physiol*, vol. 309, pp. R1380–6, Dec 2015.
 - [24] G. Sundlöf and B. G. Wallin, “The variability of muscle nerve sympathetic activity in resting recumbent man,” *J Physiol*, vol. 272, pp. 383–97, Nov 1977.
 - [25] V. G. Macefield, “Sympathetic microneurography,” *Handb Clin Neurol*, vol. 117, pp. 353–64, 2013.
 - [26] “ecg-reading-the-waves(<https://www.msdmanuals.com/en-sg/home/multimedia/figure/ecg-reading-the-waves>).”
 - [27] N. Charkoudian and B. G. Wallin, “Sympathetic neural activity to the cardiovascular system: integrator of systemic physiology and interindividual characteristics,” *Compr Physiol*, vol. 4, pp. 825–50, Apr 2014.
 - [28] J. C. Longhurst and L.-W. Fu, “Chapter 35 - cardiac and other visceral afferents,” in *Primer on the Autonomic Nervous System (Third Edition)* (D. Robertson, I. Biaggioni, G. Burnstock, P. A. Low, and J. F. Paton, eds.), pp. 171–176, San Diego: Academic Press, third edition ed., 2012.
 - [29] E. G. Vaschillo, B. Vaschillo, J. F. Buckman, R. J. Pandina, and M. E. Bates, “Measurement of vascular tone and stroke volume baroreflex gain,” *Psychophysiology*, vol. 49, pp. 193–7, Feb 2012.
 - [30] B. G. Wallin, D. Burke, and S. Gandevia, “Coupling between variations in strength and baroreflex latency of sympathetic discharges in human muscle nerves,” *J Physiol*, vol. 474, pp. 331–8, Jan 1994.
 - [31] P. Kienbaum, T. Karlsson, Y. B. Sverrisdottir, M. Elam, and B. G. Wallin, “Two sites for modulation of human sympathetic activity by arterial baroreceptors?,” *J Physiol*, vol. 531, pp. 861–9, Mar 2001.
 - [32] V. G. Macefield and B. G. Wallin, “The discharge behaviour of single sympathetic neurones supplying human sweat glands,” *J Auton Nerv Syst*, vol. 61, pp. 277–86, Dec 1996.
 - [33] J. Fagius and B. G. Wallin, “Sympathetic reflex latencies and conduction velocities in normal man,” *J Neurol Sci*, vol. 47, pp. 433–48, Sep 1980.

- [34] V. G. Macefield, “On the number of preganglionic neurons driving human postganglionic sympathetic neurons: a comparison of modeling and empirical data,” *Front Neurosci*, vol. 5, p. 132, 2011.
- [35] M. Elam, D. McKenzie, and V. Macefield, “Mechanisms of sympathoexcitation: single-unit analysis of muscle vasoconstrictor neurons in awake osas subjects,” *J Appl Physiol (1985)*, vol. 93, pp. 297–303, Jul 2002.
- [36] V. G. Macefield, B. Rundqvist, Y. B. Sverrisdottir, B. G. Wallin, and M. Elam, “Firing properties of single muscle vasoconstrictor neurons in the sympathoexcitation associated with congestive heart failure,” *Circulation*, vol. 100, pp. 1708–13, Oct 1999.
- [37] V. G. Macefield and B. G. Wallin, “Firing properties of single vasoconstrictor neurones in human subjects with high levels of muscle sympathetic activity,” *J Physiol*, vol. 516 (Pt 1), pp. 293–301, Apr 1999.
- [38] V. G. Macefield, M. Elam, and B. G. Wallin, “Firing properties of single post-ganglionic sympathetic neurones recorded in awake human subjects,” *Auton Neurosci*, vol. 95, pp. 146–59, Jan 2002.
- [39] H. Murai, M. Takamura, and S. Kaneko, “Advantage of recording single-unit muscle sympathetic nerve activity in heart failure,” *Front Physiol*, vol. 3, p. 109, 2012.
- [40] P. H. M. Kullmann and J. P. Horn, “Homeostatic regulation of m-current modulates synaptic integration in secretomotor, but not vasomotor, sympathetic neurons in the bullfrog,” *J Physiol*, vol. 588, pp. 923–38, Mar 2010.
- [41] J. A. Dempsey, A. W. Sheel, C. M. St Croix, and B. J. Morgan, “Respiratory influences on sympathetic vasomotor outflow in humans,” *Respir Physiol Neurobiol*, vol. 130, pp. 3–20, Mar 2002.
- [42] D. L. Eckberg, C. Nerhed, and B. G. Wallin, “Respiratory modulation of muscle sympathetic and vagal cardiac outflow in man,” *J Physiol*, vol. 365, pp. 181–96, Aug 1985.
- [43] D. R. Seals, N. O. Suwarno, M. J. Joyner, C. Iber, J. G. Copeland, and J. A. Dempsey, “Respiratory modulation of muscle sympathetic nerve activity in intact and lung denervated humans,” *Circ Res*, vol. 72, pp. 440–54, Feb 1993.
- [44] C. Ashley, D. Burton, Y. B. Sverrisdottir, M. Sander, D. K. McKenzie, and V. G. Macefield, “Firing probability and mean firing rates of human muscle vasoconstrictor neurones are elevated during chronic asphyxia,” *J Physiol*, vol. 588, pp. 701–12, Feb 2010.

- [45] C. M. St Croix, M. Satoh, B. J. Morgan, J. B. Skatrud, and J. A. Dempsey, “Role of respiratory motor output in within-breath modulation of muscle sympathetic nerve activity in humans,” *Circ Res*, vol. 85, pp. 457–69, Sep 1999.
- [46] D. W. Richter, “Generation and maintenance of the respiratory rhythm,” *J Exp Biol*, vol. 100, pp. 93–107, Oct 1982.
- [47] I. Leusen and J. Weyne, “Central neurone environment,” in *Central Neurone Environment and the Control Systems of Breathing and Circulation* (M. E. Schlafke, W. R. See, and H.-P. Koepchen, eds.), (Berlin, Heidelberg), pp. 1–12, Springer Berlin Heidelberg, 1983.
- [48] D. L. Eckberg, Y. T. Kifle, and V. L. Roberts, “Phase relationship between normal human respiration and baroreflex responsiveness,” *J Physiol*, vol. 304, pp. 489–502, Jul 1980.
- [49] J. Hayano, F. Yasuma, A. Okada, S. Mukai, and T. Fujinami, “Respiratory sinus arrhythmia. a phenomenon improving pulmonary gas exchange and circulatory efficiency,” *Circulation*, vol. 94, pp. 842–7, Aug 1996.
- [50] G. E. Billman, “Heart rate variability ? a historical perspective,” *Frontiers in Physiology*, vol. 2, 2011.
- [51] M. Elstad, E. L. O’Callaghan, A. J. Smith, A. Ben-Tal, and R. Ramchandra, “Cardiorespiratory interactions in humans and animals: rhythms for life,” *Am J Physiol Heart Circ Physiol*, vol. 315, pp. H6–H17, 07 2018.
- [52] A. E. Simms, J. F. R. Paton, A. E. Pickering, and A. M. Allen, “Amplified respiratory-sympathetic coupling in the spontaneously hypertensive rat: does it contribute to hypertension?,” *J Physiol*, vol. 587, pp. 597–610, Feb 2009.
- [53] H. J. Häbler, W. Jänig, and M. Michaelis, “Respiratory modulation in the activity of sympathetic neurones,” *Prog Neurobiol*, vol. 43, pp. 567–606, Aug 1994.
- [54] D. B. Zoccal, J. F. R. Paton, and B. H. Machado, “Do changes in the coupling between respiratory and sympathetic activities contribute to neurogenic hypertension?,” *Clin Exp Pharmacol Physiol*, vol. 36, pp. 1188–96, Dec 2009.
- [55] A. Von Chong, M. Terosiet, A. Histace, and O. Romain, “Towards a novel single-led pulse oximeter based on a multispectral sensor for iot applications,” *Microelectronics Journal*, vol. 88, pp. 128–136, 2019.

- [56] W. N. Leimbach, Jr, B. G. Wallin, R. G. Victor, P. E. Aylward, G. Sundlöf, and A. L. Mark, “Direct evidence from intraneuronal recordings for increased central sympathetic outflow in patients with heart failure,” *Circulation*, vol. 73, pp. 913–9, May 1986.
- [57] B. Rundqvist, R. Casale, Y. Bergmann-Sverrisdottir, P. Friberg, A. Mortara, and M. Elam, “Rapid fall in sympathetic nerve hyperactivity in patients with heart failure after cardiac transplantation,” *J Card Fail*, vol. 3, pp. 21–6, Mar 1997.
- [58] J. T. Carlson, J. Hedner, M. Elam, H. Ejnell, J. Sellgren, and B. G. Wallin, “Augmented resting sympathetic activity in awake patients with obstructive sleep apnea.,” *Chest*, vol. 103, pp. 1763–1768, Jun 1993.
- [59] K. Narkiewicz, M. Kato, B. G. Phillips, C. A. Pesek, D. E. Davison, and V. K. Somers, “Nocturnal continuous positive airway pressure decreases daytime sympathetic traffic in obstructive sleep apnea,” *Circulation*, vol. 100, pp. 2332–5, Dec 1999.
- [60] V. G. Macefield, M. Elam, and B. G. Wallin, “Firing properties of single postganglionic sympathetic neurones recorded in awake human subjects.,” *Auton Neurosci*, vol. 95, pp. 146–159, Jan 2002.
- [61] S. Heindl, M. Lehnert, C. P. Criée, G. Hasenfuss, and S. Andreas, “Marked sympathetic activation in patients with chronic respiratory failure,” *Am J Respir Crit Care Med*, vol. 164, pp. 597–601, Aug 2001.
- [62] M. Böhm, M. Flesch, and P. Schnabel, “Beta-adrenergic signal transduction in the failing and hypertrophied myocardium,” *J Mol Med (Berl)*, vol. 75, no. 11-12, pp. 842–8, 1997.
- [63] C. Communal, K. Singh, D. R. Pimentel, and W. S. Colucci, “Norepinephrine stimulates apoptosis in adult rat ventricular myocytes by activation of the beta-adrenergic pathway,” *Circulation*, vol. 98, pp. 1329–34, Sep 1998.
- [64] B. Chaudhri, F. Del Monte, R. J. Hajjar, and S. E. Harding, “Interaction between increased serca2a activity and beta -adrenoceptor stimulation in adult rabbit myocytes,” *Am J Physiol Heart Circ Physiol*, vol. 283, pp. H2450–7, Dec 2002.
- [65] V. G. Macefield and B. G. Wallin, “Respiratory and cardiac modulation of single sympathetic vasoconstrictor and sudomotor neurones to human skin,” *J Physiol*, vol. 516 (Pt 1), pp. 303–14, Apr 1999.

- [66] D. M. Baekey, Y. I. Molkov, J. F. R. Paton, I. A. Rybak, and T. E. Dick, “Effect of baroreceptor stimulation on the respiratory pattern: insights into respiratory-sympathetic interactions,” *Respir Physiol Neurobiol*, vol. 174, pp. 135–45, Nov 2010.
- [67] D. Yumino and T. D. Bradley, “Central sleep apnea and cheyne-strokes respiration,” *Proc Am Thorac Soc*, vol. 5, pp. 226–36, Feb 2008.
- [68] T. E. Dick, Y.-H. Hsieh, R. R. Dhingra, D. M. Baekey, R. F. Galán, E. Wehrwein, and K. F. Morris, “Cardiorespiratory coupling: common rhythms in cardiac, sympathetic, and respiratory activities,” *Prog Brain Res*, vol. 209, pp. 191–205, 2014.
- [69] R. P. R. Tompkins, C. W. J. Melling, T. D. Wilson, B. D. Bates, and J. K. Shoemaker, “Arrangement of sympathetic fibers within the human common peroneal nerve: implications for microneurography,” *J Appl Physiol (1985)*, vol. 115, pp. 1553–61, Nov 2013.
- [70] B. G. Wallin and N. Charkoudian, “Sympathetic neural control of integrated cardiovascular function: insights from measurement of human sympathetic nerve activity,” *Muscle Nerve*, vol. 36, pp. 595–614, Nov 2007.
- [71] V. G. Macefield, Y. B. Sverrisdottir, M. Elam, and J. Harris, “Firing properties of sudomotor neurones in hyperhidrosis and thermal sweating,” *Clin Auton Res*, vol. 18, pp. 325–30, Dec 2008.
- [72] Y. B. Sverrisdóttir, B. Rundqvist, G. Johannsson, and M. Elam, “Sympathetic neural burst amplitude distribution: A more specific indicator of sympathoexcitation in human heart failure,” *Circulation*, vol. 102, pp. 2076–81, Oct 2000.
- [73] Y. B. Sverrisdóttir, B. Rundqvist, and M. Elam, “Relative burst amplitude in human muscle sympathetic nerve activity: a sensitive indicator of altered sympathetic traffic,” *Clin Auton Res*, vol. 8, pp. 95–100, Apr 1998.
- [74] A. Malliani, M. Pagani, F. Lombardi, and S. Cerutti, “Cardiovascular neural regulation explored in the frequency domain,” *Circulation*, vol. 84, pp. 482–92, Aug 1991.
- [75] G. Parati, J. P. Saul, M. Di Rienzo, and G. Mancia, “Spectral analysis of blood pressure and heart rate variability in evaluating cardiovascular regulation. a critical appraisal,” *Hypertension*, vol. 25, pp. 1276–86, Jun 1995.

- [76] M. Nitzan, A. Babchenko, B. Khanokh, and D. Landau, “The variability of the photoplethysmographic signal—a potential method for the evaluation of the autonomic nervous system,” *Physiol Meas*, vol. 19, pp. 93–102, Feb 1998.
- [77] M. Nitzan, S. Turivnenko, A. Milston, A. Babchenko, and Y. Mahler, “Low-frequency variability in the blood volume and in the blood volume pulse measured by photoplethysmography,” *J Biomed Opt*, vol. 1, pp. 223–9, Apr 1996.
- [78] D. Korpas, J. Hálek, and L. Dolezal, “Parameters describing the pulse wave,” *Physiol Res*, vol. 58, no. 4, pp. 473–479, 2009.
- [79] F. A. R. Stammers, “Digital plethysmography. by george e. burch, m.d., f.a.c.p., henderson professor of medicine, tulane university school of medicine. 8â x 5â in. pp. viii+134, with 83 figures. index. 1954. new york: Grune & stratton. price \$5.00,” *The Journal of Bone and Joint Surgery. British volume*, vol. 36-B, no. 4, pp. 706–707, 1954.
- [80] M. Betta, G. Handjaras, E. Ricciardi, P. Pietrini, J. Haba-Rubio, F. Siclari, R. Heinzer, and G. Bernardi, “Quantifying peripheral sympathetic activations during sleep by means of an automatic method for pulse wave amplitude drop detection,” *Sleep Med*, vol. 69, pp. 220–232, 05 2020.
- [81] J. Moeyersons, M. Amoni, S. Van Huffel, R. Willems, and C. Varon, “R-deco: an open-source matlab based graphical user interface for the detection and correction of r-peaks.,” *PeerJ Comput Sci*, vol. 5, p. e226, 2019.
- [82] G. B. Moody and R. G. Mark, “The impact of the mit-bih arrhythmia database,” *IEEE Eng Med Biol Mag*, vol. 20, no. 3, pp. 45–50, 2001.
- [83] V. G. Macefield, B. G. Wallin, and A. B. Vallbo, “The discharge behaviour of single vasoconstrictor motoneurones in human muscle nerves,” *J Physiol*, vol. 481 (Pt 3), pp. 799–809, Dec 1994.
- [84] C. Hirotsu, M. Betta, G. Bernardi, P. Marques-Vidal, P. Vollenweider, G. Waeber, V. Pichot, F. Roche, F. Siclari, J. Haba-Rubio, and R. Heinzer, “Pulse wave amplitude drops during sleep: clinical significance and characteristics in a general population sample.,” *Sleep*, vol. 43, Jul 2020.